CHAPTER
11

Volume-Scattering Models and Land Observations

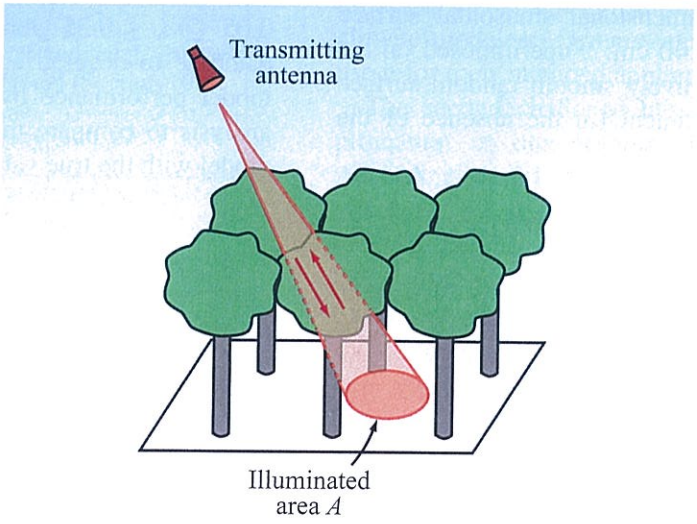

Volume scattering

CONTENTS

The Nature of Volume Scattering

In contrast with surface scattering, which occurs at a continuous surface interface between two media with different dielectric properties, volume scattering is caused by discrete particles present in an otherwise homogeneous background dielectric medium. The sketch shown in Fig. 11-1 depicts a layer of dry snow above a soil medium. The snow consists of ice crystals suspended in an air background. The total signal scattered by the snow-soil composite includes scattering components due to surface scattering by the air-snow interface and by the snow-soil interface, volume scattering by the ice crystals, and multiple scattering involving both surface and volume scattering. A similar scenario applies to the vegetation canopy shown in Fig. 11-2, except that the top of the canopy does not have a distinct boundary. To compute the scattering at the diffuse air-canopy boundary, we represent the canopy in terms of an equivalent, homogeneous dielectric medium. However, because the vegetation material contained in the canopy constitutes less than 1% of the canopy by volume, the real part of the effective dielectric constant of the canopy is only slightly larger than that of air. Consequently, we treat the air-canopy boundary as a nonscattering diffuse boundary.

► When modeling or analyzing radar scattering or radiometric emission by a volume-scattering medium, it is prudent to consider the following factors:

(a) The size distribution of the scatterers, relative to the wavelength λ.

(b) The 3-D orientation distribution of the scatterers.

(c) The shape distributions of the scatterers.

(d) The dielectric constant of the scatterers (for each type of scatterer, if more than one type exists in the scattering volume). ◄

These factors determine:

(a) Whether or not the shape of a scatterer is important so far as its scattering pattern is concerned. Large scatterers (relative to λ) have distinct scattering patterns, whereas the scattering patterns of very small scatterers can be approximated by the Rayleigh phase function (Section 11-6.5) regardless of their shapes.

(b) Whether or not volume scattering by the layer can be limited to single scattering, thereby simplifying the computation.

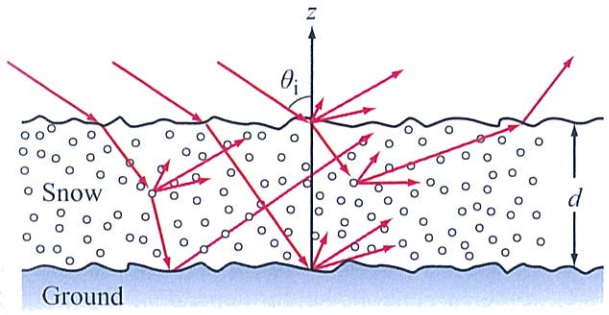

Figure 11-1: Scattering by a snow layer.

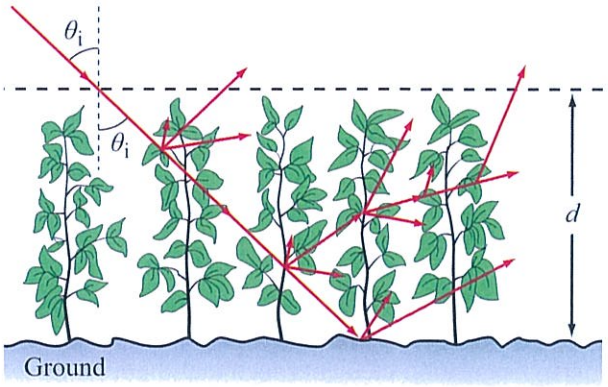

Figure 11-2: Volume scattering by a vegetation canopy.

(c) Whether or not the extinction coefficient of the medium is dominated by absorption (relative to scattering).

(d) Whether or not the volume exhibits azimuthal symmetry.

To help the reader develop an understanding of the interrelationships between these various factors and their consequences, we begin with heuristic descriptions of the scattering process for simple cases, followed by an overview presentation of the wave propagation properties of various media of interest. The combination of the two topics provides a useful background for our discussion of radiative transfer theory in Sections 11-6 and 11-7.

11-1 Heuristic Single-Scattering Model for Vegetation

Consider the vegetation canopy depicted in Fig. 11-3.

► A ***single-scattering*** backscatter model accounts for scattering contributions that involve single scattering by the canopy volume, but may include double, single, or no scattering by the underlying ground surface. ◄

These contributions include:

(a) single backscattering by the ground surface, taking into account the two-way transmission through the canopy (denoted "ray 1" in Fig. 11-3).

(b) single direct backscattering by the canopy constituents (denoted "ray 2" in Fig. 11-3).

(c) combination of single bistatic scattering (reflection) by the ground followed by single bistatic scattering by vegetation elements such that the final direction is towards the radar, or the reverse of the scattering sequence (denoted "ray 3a" and "ray 3b", respectively, in Fig. 11-3).

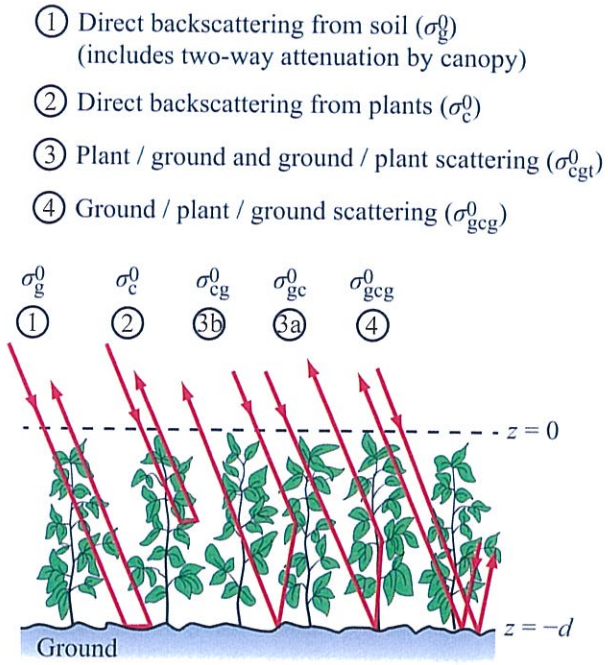

Figure 11-3: Single-scattering contributions in a vegetation canopy.

(d) transmission through the canopy, followed by specular reflection by the ground surface, followed by backscatter by the vegetation volume, followed by another specular reflection by the ground surface ("ray 4" in Fig. 11-3).

For a differential canopy volume, the ***p-polarized extinction coefficient*** κ_e^p accounts for absorption and scattering losses experienced by a wave propagating through it. That is,

$$\kappa_e^p = \kappa_a^p + \kappa_s^p. \tag{11.1}$$

Because the canopy may be nonuniform in height and nonisotropic azimuthally, and because its constituents (leaves, stalks, etc.) have specific shapes and orientations, κ_e^p is, in general, height-dependent (between the top of the canopy at $z = 0$ and the bottom of the canopy at depth $z = -d$), direction-dependent, and polarization-dependent. *For the sake of this simple heuristic model,*

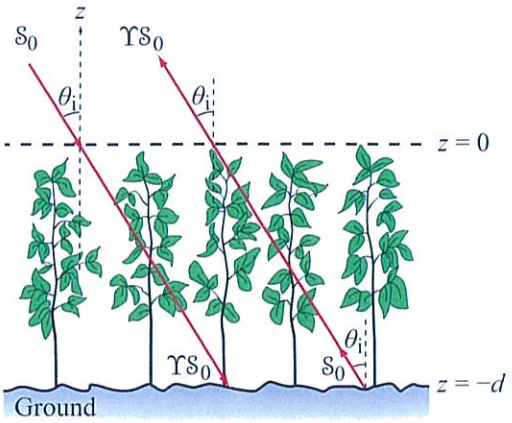

Figure 11-4: Transmissivity Υ accounts for transmission loss through the canopy along angle θ_i.

we assume that κ_s^p, κ_a^p, and κ_e^p are uniform as a function of z within the canopy.

For propagation downward along incidence angle θ_i relative to nadir, or upward along angle θ_i relative to $-z$ (Fig. 11-4), the p-polarized one-way oblique ***transmittivity*** of the canopy, Υ_p, is given by

$$\Upsilon_p = e^{-\tau_p}, \tag{11.2}$$

where τ_p is the p-polarized ***attenuation (optical depth)*** of the canopy,

$$\tau_p = \kappa_e^p d \sec\theta_i \qquad \text{(Np)}. \tag{11.3}$$

Scattering Terminology

In the forthcoming derivation, we use multiple scattering-related quantities. For the sake of clarity, we offer the following definitions:

$\sigma^0_{\text{name}_{pq}}$: The superscript 0 identifies this quantity as a ***scattering coefficient*** (scattering cross section per unit area), measured in m^2/m^2; its "name" subscript refers to the abbreviated name of the associated scattering mechanism (see Fig. 11-3); and pq refers to the receive/transmit polarizations (with $p, q =$ v or h).

$\sigma^{\text{back}}_{v_{pq}}$: The subscript v denotes this quantity as the ***volume backscattering coefficient*** (scattering cross section per unit volume), measured in $m^2/m^3 = m^{-1}$; and the superscript "back" denotes that the incident and scattering directions are exact opposites.

$\sigma^{\text{bist}}_{v_{pq}}$: This quantity also is a ***volume scattering coefficient***, but it is for bistatic scattering.

$\sigma^{\text{back}}_{pq}$: ***Backscattering cross section*** of a single particle (m^2).

$\sigma^{\text{bist}}_{pq}$: ***Bistatic scattering cross section*** of a single particle (m^2).

11-1.1 Direct Ground Contribution

If in the absence of the vegetation layer the backscattering coefficient of the ground surface is $\sigma^0_{s_{pq}}$, the presence of the vegetation simply modifies the direct ground contribution by a factor of $\Upsilon_p\Upsilon_q$,

$$\sigma^0_{g_{pq}}(\theta_i) = \Upsilon_p\Upsilon_q\,\sigma^0_{s_{pq}}(\theta_i) \qquad (m^2/m^2), \tag{11.4}$$

$$(p, q = \text{v or h polarization}).$$

Since $\sigma^0_{s_{pq}}$ is, in general, polarization and angle dependent, so is $\sigma^0_{g_{pq}}$.

11-1.2 Direct Volume Contribution—The Cloud Model

To model the scattering contribution of the canopy volume $\sigma^0_{c_{pq}}(\theta_i)$, Attema and Ulaby (1978) treated the canopy as an equivalent "water cloud" consisting of identical scatterers that are uniformly distributed throughout the volume, as illustrated in Fig. 11-5. Ignoring multiple scattering, the pq-polarized ***volume backscattering coefficient*** $\sigma^{\text{back}}_{v_{pq}}$ of the vegetation medium is

$$\sigma^{\text{back}}_{v_{pq}} = N_v\sigma^{\text{back}}_{pq} \qquad (m^{-1}), \tag{11.5}$$

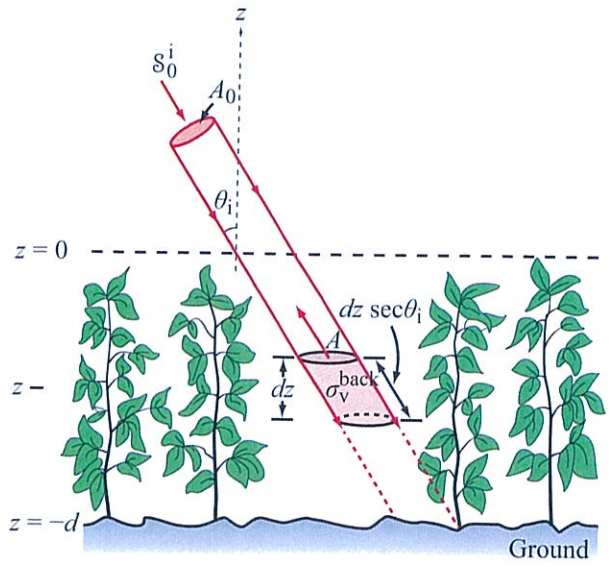

Figure 11-5: Direct backscatter contribution by the canopy volume.

where N_v is the ***number density*** (number of scattering particles per unit volume [in m^{-3})] and σ_{pq}^{back} is the pq-polarized backscattering cross section of a single particle.

With reference to Fig. 11-5, for a q-polarized incident plane wave with power density $\mathcal{S}_0^i$ before intercepting the canopy, the q-polarized power density across an area A of a differential volume within the canopy at a lateral distance $z\sec\theta_i$ from the surface is

$$\mathcal{S}_q^i(z) = \mathcal{S}_0^i \cos\theta_i \, e^{\kappa_e^q z \sec\theta_i} \qquad (W/m^2), \tag{11.6}$$

where κ_e^q is the extinction coefficient for q polarization. Note that the top of the canopy is denoted $z = 0$ and the ground is denoted $z = -d$, so within the canopy layer, $z \le 0$. The $\cos\theta$ factor accounts for the reduction in power density between that incident upon A_0 and that incident upon the larger area $A = A_0/\cos\theta_i$, and the exponential function represents the one-way transmissivity between the canopy surface and the differential volume at depth z.

Given that $\sigma_{v_{pq}}^{back}$ is the backscattering cross section per unit volume and the volume of the differential volume is $A\sec\theta_i \, dz$, the total backscattering cross section of the differential volume is

$$d\sigma_{pq}^{back} = \sigma_{v_{pq}}^{back} A \sec\theta_i \, dz \qquad (m^2). \tag{11.7}$$

The differential p-polarized power reradiated by the differential volume in the backscatter direction, after propagation from z to the top of the canopy, is

$$\begin{aligned} dP_p^{rer} &= \mathcal{S}_q^i(z) \, d\sigma_{pq}^{back} \, e^{\kappa_e^p z \sec\theta_i} \\ &= \mathcal{S}_0^i A \cos\theta_i \, \sigma_{v_{pq}}^{back} \, e^{2(\kappa_e^q + \kappa_e^p) z \sec\theta_i} \sec\theta_i \, dz. \end{aligned} \tag{11.8}$$

Integrating dP_p^{rer} over the full depth of the canopy yields

$$\begin{aligned} P_p^{rer} &= \int_{-d}^{0} \mathcal{S}_0^i A \cos\theta_i \, \sigma_{v_{pq}}^{back} e^{(\kappa_e^p + \kappa_e^q) z \sec\theta_i} \sec\theta_i \, dz \\ &= \frac{\mathcal{S}_0^i A \, \sigma_{v_{pq}}^{back}}{(\kappa_e^p + \kappa_e^q)\sec\theta_i} \left[1 - e^{-(\kappa_e^p + \kappa_e^q) d \sec\theta_i}\right] \\ &= \frac{\mathcal{S}_0^i A \cos\theta_i \, \sigma_{v_{pq}}^{back}}{\kappa_e^p + \kappa_e^q} \left[1 - \Upsilon_p \Upsilon_q\right], \end{aligned} \tag{11.9}$$

where Υ is the one-way transmissivity defined by Eq. (11.2).

At a range R_r to the receive antenna, the p-polarized power density of the scattered wave is

$$\mathcal{S}_p^s = \frac{P_p^{rer}}{4\pi R_r^2}.$$

Application of the standard definition for the radar cross section given by Eq. (5.30) and then dividing by A to obtain the pq-polarized ***canopy backscattering coefficient*** $\sigma_{c_{pq}}^0$, leads to

$$\begin{aligned} \sigma_{c_{pq}}^0(\theta_i) &= \frac{4\pi R_r^2}{A} \frac{\mathcal{S}_p^s}{\mathcal{S}_0^i} \\ &= \frac{\sigma_{v_{pq}}^{back} \cos\theta_i}{\kappa_e^p + \kappa_e^q} \left(1 - \Upsilon_p \Upsilon_q\right) \qquad (m^2/m^2). \end{aligned} \tag{11.10}$$

If σ_v^{back} and κ_e are polarization-independent and do not generate cross polarization, then $\sigma_c^0(\theta_i)$ is the same for hh and vv polarization and zero for hv polarization. For real canopies, σ_c^0 is not zero for hv polarization, and if the canopy contains vertical stalks, σ_c^0 may not have the same magnitude for hh and vv polarizations.

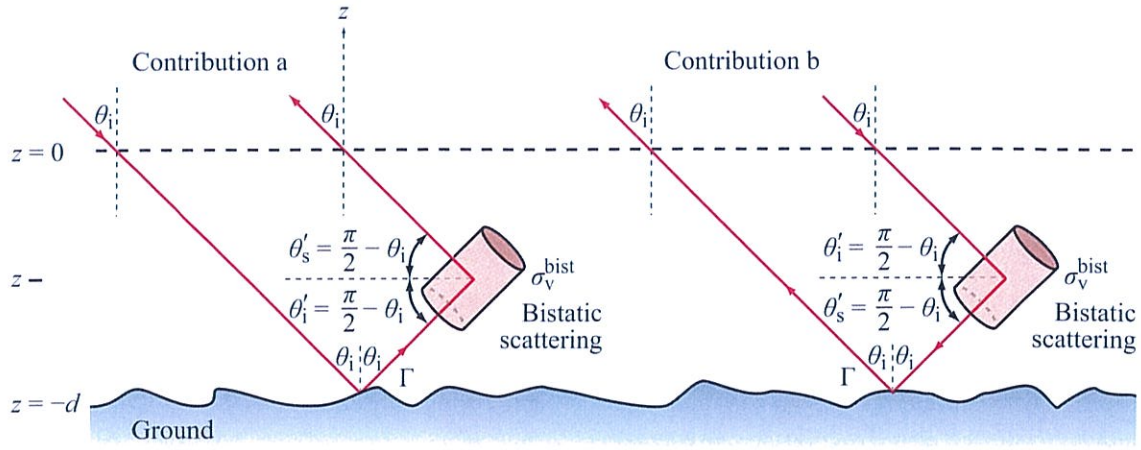

Figure 11-6: The two volume-ground single-scattering contributions.

11-1.3 Canopy-Ground Contributions

To compute the two components of the canopy ground contribution, namely the one involving ground reflection followed by canopy bistatic scattering in the direction of the radar, and the other involving the sequence in reverse order (Fig. 11-6), we treat the ground boundary as a ***quasi-specular*** surface. By quasi-specular, we mean that we limit reflection to the specular direction, but we account for the reduction in the magnitude of the Fresnel reflectivity caused by surface roughness. That is, we use Eq. (5.110) to describe the p-polarized coherent reflectivity $\Gamma^p_{\rm coh}(\theta_i)$ in terms of the p-polarized Fresnel reflectivity for a specular surface $\Gamma^p(\theta_i)$,

$$\Gamma^p_{\rm coh}(\theta_i) = \Gamma^p(\theta_i)\, e^{-4k^2 s^2 \cos^2\theta_i}, \qquad (p = \text{v or h}), \tag{11.11}$$

where $k = 2\pi/\lambda$ is the wavenumber and s is the rms height of the ground surface.

> ► In the material that follows, we use the symbol Γ to represent the surface reflectivity, with the implicit understanding that Γ should be replaced with $\Gamma_{\rm coh}$ if the electromagnetic roughness $ks > 0.2$. ◄

Under the specular-reflection condition, all propagation occurs along downward and upward directions that make an angle θ_i relative to $\hat{\mathbf{z}}$ or $-\hat{\mathbf{z}}$. Consider scattering contribution "a" in Fig. 11-6. After propagation through the canopy down to the ground surface and reflection along the specular direction, the wave propagates all the way to the top of the canopy and beyond. Along the way, part of the upward propagating energy gets bistatically scattered in the direction of the radar. The fraction of energy so scattered is proportional to the ***volume bistatic scattering coefficient*** $\sigma^{\rm bist}_{{\rm v}pq}(\theta_s', \phi_s'; \theta_i', \phi_i')$, where (θ_i', ϕ_i') and (θ_s', ϕ_s') define the incident and scattered directions relative to the differential volume under consideration. Under the specular-direction condition, $\phi_s' = \phi_i' = 0$ and $\theta_i' = \theta_s' = \pi/2 - \theta_i$. Repeat of the steps we used earlier to derive the expression for σ^0_c given by Eq. (11.10) leads to the following expression for the ***ground-canopy backscattering coefficient***:

$$\sigma^0_{{\rm gc}_{pq}}(\theta_i) = \sigma^{\rm bist}_{{\rm v}_{pq}} \cdot d\Gamma^q \Upsilon_q \Upsilon_p, \tag{11.12}$$

where d is the height of the canopy and the volume bistatic scattering coefficient $\sigma^{\rm bist}_{{\rm v}_{pq}}$ is defined for $\theta_i' = \theta_s' = \pi/2 - \theta_i$.

Similarly, for contribution "b" in Fig. 11-6,

$$\sigma^0_{{\rm cg}_{pq}}(\theta_i) = \sigma^{\rm bist}_{{\rm v}_{pq}} \cdot d\Gamma^p \Upsilon_p \Upsilon_q. \tag{11.13}$$

The sum of the two components is denoted the ***total canopy ground contribution***:

$$\sigma^0_{\mathrm{cgt}_{pq}}(\theta_\mathrm{i}) = \sigma^0_{\mathrm{gc}_{pq}}(\theta_\mathrm{i}) + \sigma^0_{\mathrm{cg}_{pq}}(\theta_\mathrm{i}) = \sigma^{\mathrm{bist}}_{\mathrm{v}_{pq}} \cdot d[\Gamma^p + \Gamma^q]\Upsilon_p\Upsilon_q. \tag{11.14}$$

For $p = q$ (i.e., for hh or vv polarization), Eq. (11.14) simplifies to

$$\sigma^0_{\mathrm{cgt}_{pp}}(\theta_\mathrm{i}) = 2\sigma^{\mathrm{bist}}_{\mathrm{v}_{pp}} \cdot d\Gamma^p\Upsilon_p^2 \qquad (p = \mathrm{h\ or\ v}). \tag{11.15a}$$

(incoherent addition)

Our treatment is based on radiative transfer theory, which deals with power quantities instead of electric fields. Hence, different contributions are added incoherently (with regard to phase). Since the two contributions undergo the same propagation and reflection sequence, but in reverse order, they should have the same amplitude and phase, in which case their electric fields should be added coherently.

Coherent addition increases the magnitude of σ^0_{cgt} for hh and vv polarizations by a factor of 2. Thus,

$$\sigma^0_{\mathrm{cgt}_{pp}}(\theta_\mathrm{i}) = 4\sigma^{\mathrm{bist}}_{\mathrm{v}_{pp}} \cdot d\Gamma^p\Upsilon_p^2 \qquad (p = \mathrm{h\ or\ v}). \tag{11.15b}$$

(coherent addition)

This increase in the level of the co-polarized total canopy-ground contribution is known as ***bistatic scattering enhancement***.

11-1.4 Ground-Canopy-Ground Contribution

Term 2 in Fig. 11-3 represents upward backscatter by the canopy volume. Term 4 represents backscatter by the canopy volume along the downward direction, in addition to double reflections by the ground surface and an extra two-way propagation through the canopy. Hence, the ground-canopy-ground contribution is

$$\sigma_{\mathrm{gcg}_{pq}}(\theta_\mathrm{i}) = \Upsilon_p\Upsilon_q\Gamma^p\Gamma^q\,\sigma^0_{\mathrm{c}_{pq}}(\theta_\mathrm{i}) = \frac{\sigma^{\mathrm{back}}_{\mathrm{v}_{pq}}\cos\theta_\mathrm{i}}{\kappa_\mathrm{e}^p + \kappa_\mathrm{e}^q}\,\Gamma^p\Gamma^q(\Upsilon_p\Upsilon_q - \Upsilon_p^2\Upsilon_q^2). \tag{11.16}$$

11-1.5 Single-Scattering Radiative Transfer Model

The total single-scattering backscattering coefficient is the sum of the four contributions derived in the preceding subsections:

$$\begin{aligned}\sigma^0_{pq} &= \sigma^0_{\mathrm{g}_{pq}} + \sigma^0_{\mathrm{c}_{pq}} + \sigma^0_{\mathrm{cgt}_{pq}} + \sigma^0_{\mathrm{gcg}_{pq}} \\ &= \Upsilon_p\Upsilon_q\,\sigma^0_{\mathrm{s}_{pq}}(\theta_\mathrm{i}) \\ &\quad + \frac{\sigma^{\mathrm{back}}_{\mathrm{v}_{pq}}\cos\theta_\mathrm{i}}{\kappa_\mathrm{e}^p + \kappa_\mathrm{e}^q}\,(1 - \Upsilon_p\Upsilon_q)(1 + \Gamma^p\Gamma^q\Upsilon_p\Upsilon_q) \\ &\quad + n\,\sigma^{\mathrm{bist}}_{\mathrm{v}_{pq}}\,d(\Gamma^p + \Gamma^q)\Upsilon_p\Upsilon_q,\end{aligned} \tag{11.17}$$

with

$$n = \begin{cases} 1 & \text{for hv polarization and also for hh and vv under the incoherent addition assumption,} \\ 2 & \text{for hh and vv polarizations with coherent addition.} \end{cases}$$

We refer to Eq. (11.17) as the ***single-scattering radiative-transfer*** ($\mathrm{S^2RT}$) model because it is identical with the formal solution of the radiative transfer equation obtained later in Section 11-5.

The absence of a vegetation layer implies that $d = 0$ and $\Upsilon = 1$, in which case Eq. (11.17) reduces to $\sigma^0 = \sigma^0_{\mathrm{s}_{pq}}$. At the other extreme, for a very dense canopy with high attenuation, $\Upsilon \approx 0$, in which case the canopy appears like a semi-infinite layer with

$$\sigma^0_{pq}(\theta_\mathrm{i}) = \frac{\sigma^{\mathrm{back}}_{\mathrm{v}_{pq}}\cos\theta_\mathrm{i}}{\kappa_\mathrm{e}^p + \kappa_\mathrm{e}^q}, \qquad (\Upsilon \to 0). \tag{11.18}$$

(semi-infinite canopy)

11-2 Isotropic and Rayleigh Scatterers

11-2.1 Canopy Elements as Isotropic Scatterers

For isotropic scatterers, the scattering pattern is uniform along all directions for both hh and vv polarizations. Hence,

$$\sigma_{\mathrm{v}}^{\mathrm{back}} = \sigma_{\mathrm{v}}^{\mathrm{bist}} = \kappa_{\mathrm{s}}, \tag{11.19}$$

where κ_{s} is the scattering component of the extinction coefficient κ_{e}. Also, $\Upsilon_p = \Upsilon_q$. Using Eq. (11.19) in Eq. (11.17) leads to

$$\sigma_{pp}^0(\theta_{\mathrm{i}}) = \Upsilon^2\, \sigma_{\mathrm{s}_{pp}}^0(\theta_{\mathrm{i}}) + \frac{a\cos\theta_{\mathrm{i}}}{2}(1-\Upsilon^2)(1+\Gamma^2\Upsilon^2) + 4\kappa_{\mathrm{s}} d\Gamma\Upsilon^2, \quad (p = \mathrm{h\ or\ v}), \tag{11.20}$$

where $\Gamma = \Gamma^p$ and we introduced the ***single-scattering albedo*** a, defined as

$$a = \frac{\kappa_{\mathrm{s}}}{\kappa_{\mathrm{e}}}. \tag{11.21}$$

11-2.2 Canopy Elements as Rayleigh Scatterers

In Section 8-5.3, we discussed the scattering and absorption properties of small spheres under the Rayleigh approximation (which we discuss further in Section 11-5.5). The scattering pattern of a Rayleigh particle depends on the incident and scattered directions, but for hh and vv polarizations and for the incident and scattered directions shown in Fig. 11-6,

$$\sigma_{\mathrm{v}}^{\mathrm{back}} = \sigma_{\mathrm{v}}^{\mathrm{bist}} = \frac{3}{2}\kappa_{\mathrm{s}} \qquad \textbf{(hh and vv polarizations)}, \tag{11.22}$$

which leads to

$$\sigma_{pp}^0(\theta_{\mathrm{i}}) = \Upsilon^2\, \sigma_{\mathrm{s}_{pp}}^0(\theta_{\mathrm{i}}) + \frac{3a}{4}\cos\theta_{\mathrm{i}}(1-\Upsilon^2)(1+\Gamma^2\Upsilon^2) + 3n\kappa_{\mathrm{s}} d\Gamma\Upsilon^2, \quad (p = \mathrm{h\ or\ v}). \tag{11.23}$$

We call this the ***S^2RT model with Rayleigh particles***, or ***S^2RT/R*** for short.†

The relative contributions of the four components of σ^0 are illustrated in Fig. 11-7 for three Rayleigh canopies: a lowloss canopy with $\Upsilon_0 = 0.8$, a medium-loss canopy with $\Upsilon_0 = 0.3$, and a high-loss canopy with $\Upsilon_0 = 0.1$. All three canopies have a single-scattering albedo $a = 0.1$ and an extinction coefficient $\kappa_{\mathrm{e}} = 1$ Np/m, but their heights vary from 0.22 m for the low-loss canopy to 2.3 m for the most lossy. The underlying soil surface is slightly rough ($ks = 0.63$) and its volumetric soil moisture is 0.2 g/cm^3. As expected, the ground component $\sigma_{\mathrm{g}_{pq}}^0$ is the dominant contributor, particularly near normal incidence, for the low-loss canopy, whereas the volume component σ_{c}^0 is the dominant contributor for the high-loss canopy.

11-3 Heuristic Single-Scattering Model for Snow-Covered Ground

The snow layer depicted in Fig. 11-8 is of depth d and contains uniformly distributed scatterers (ice crystals) in a background of air. The process of computing the backscatter from the snow-ground combination is identical with what we had done in the preceding section, except for modifications that incorporate the presence of the air-snow boundary. These modifications include:

(a) Backscatter by the air-snow boundary, represented by a backscattering coefficient σ_{as}^0. This term is proportional to the air-snow reflectivity, which (except for very wet snow conditions) is very small in magnitude because the dielectric constant of the snow layer is only slightly larger than that of air. Hence, this term usually is negligibly small in comparison with the other backscatter contributions.

(b) Transmission from air to snow across the air-snow boundary. This happens twice, on the way down into the snow layer and later on the way out, and can be accounted for by $\mathbb{T}^p\mathbb{T}^q$, where $\mathbb{T}^p$ is the p-polarized air-snow boundary transmissivity defined in Table 2-5.

† **Computer Code 11.1.**

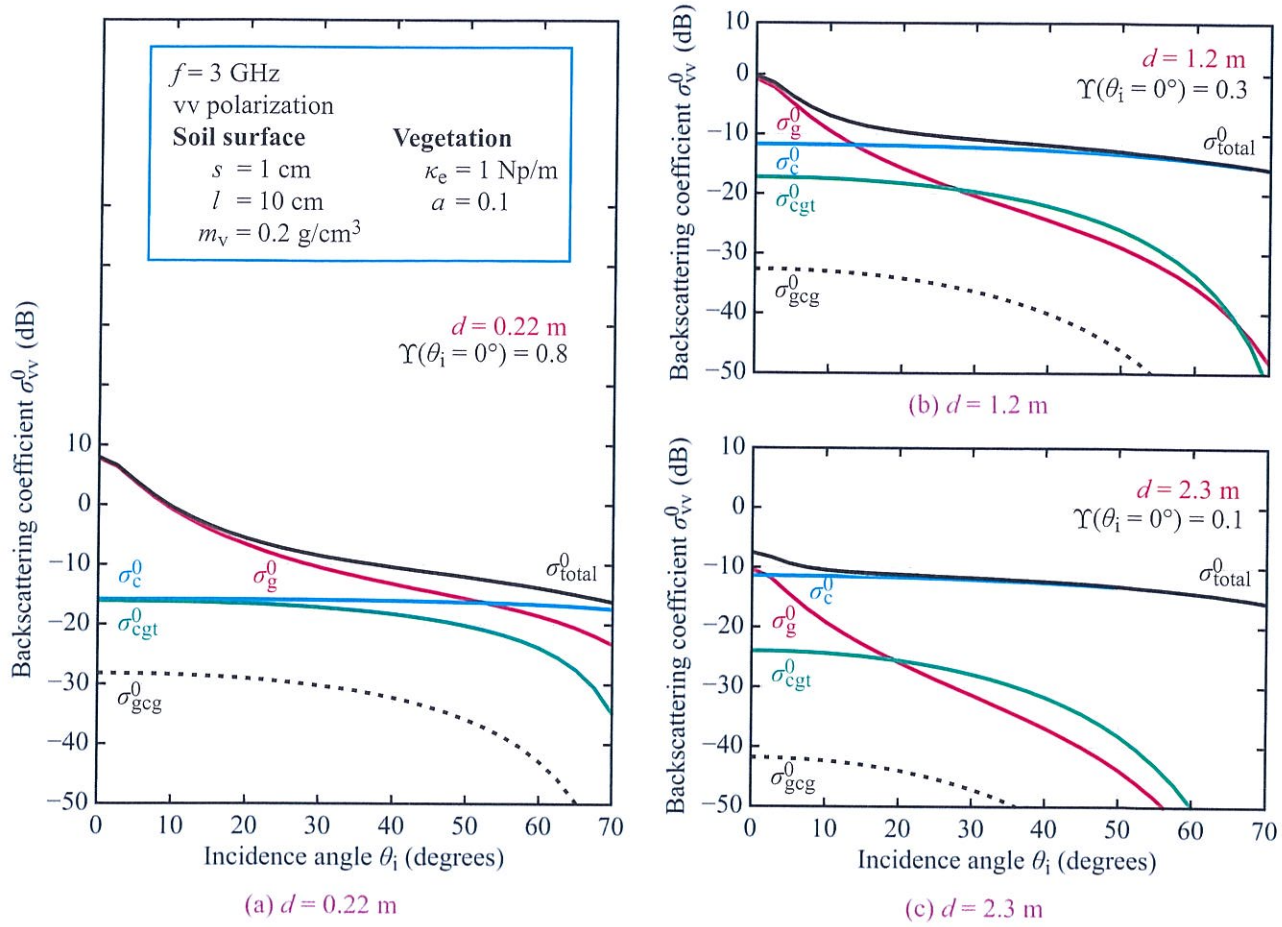

Figure 11-7: Computed backscattering by a canopy containing Rayleigh particles. The canopy heights are: (a) 0.22 m, (b) 1.2 m, and (c) 2.3 m.

Also, because of refraction from incidence angle θ_i to angle θ_i', θ_i in the expression for Υ given by Eqs. (11.2) and (11.3) should be replaced with θ_i'. Hence,

$$\sigma_{pq}^0(\theta_i) = \mathbb{T}^p(\theta_i)\,\mathbb{T}^q(\theta_i)\left[\Upsilon_p\Upsilon_q\,\sigma_{sg_{pq}}^0(\theta_i') + \frac{\sigma_{v_{pq}}^{back}(\theta_i')\cos\theta_i'}{\kappa_e^p + \kappa_e^q}(1-\Upsilon_p\Upsilon_q)(1+\Gamma^p\Gamma^q\Upsilon_p\Upsilon_q) + n\sigma_{v_{pq}}^{bist}\,d(\Gamma^p+\Gamma^q)\Upsilon_p\Upsilon_q\right] + \sigma_{as_{pq}}^0(\theta_i), \quad (11.24)$$

with

$$n = \begin{cases} 1 & \text{for hv polarization and also for hh and vv under the incoherent addition assumption,} \\ 2 & \text{for hh and vv polarizations with coherent addition,} \end{cases}$$

where σ_{sg}^0 is the snow-ground backscattering coefficient and σ_{as}^0 is the air-snow backscattering coefficient. The

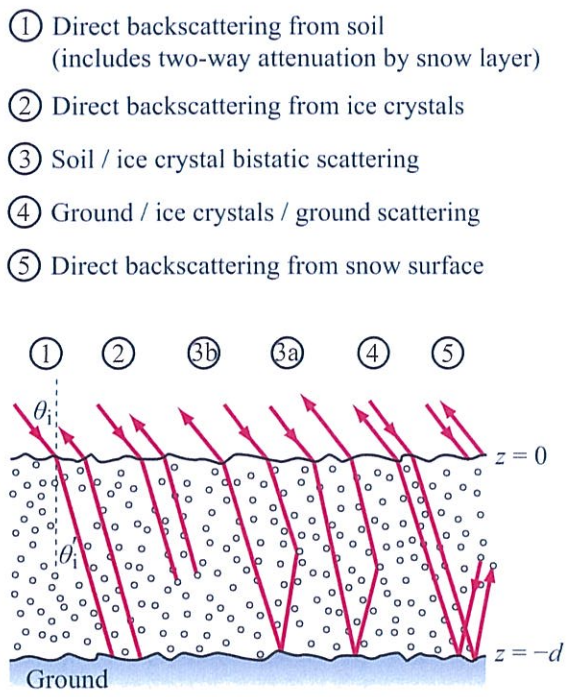

Figure 11-8: Single-scattering contributions for snow-over-ground.

formulation given by Eq. (11.24) is an ***S^2RT/R model for a layer with a distinct upper boundary.***[†]

11-4 Penetration Depth

The power density $\mathcal{S}(z)$ of an EM wave propagating in the z direction in a medium characterized by an ***extinction coefficient*** κ_e is given by

$$\mathcal{S}(z) = \mathcal{S}(0)\, e^{-\kappa_e z},$$

where $\mathcal{S}(0)$ is the power density at a reference location denoted by $z = 0$, and

$$\kappa_e = \kappa_a + \kappa_s.$$

The ***volume absorption coefficient*** κ_a is related to the effective dielectric constant ε of the medium as

$$\kappa_a = 2k_0 n'' = -2k_0\, \Im\mathrm{m}\left\{\sqrt{\varepsilon}\right\}, \qquad (11.25)$$

where $k_0 = 2\pi/\lambda_0$ with λ_0 being the free-space wavelength, and n is the complex index of refraction. If the medium is composed of multiple constituents—such as wet snow, which is a mixture of air, ice, and liquid water—then ε is the equivalent dielectric constant of the mixture. Strictly speaking, the concept of "effective" or "equivalent" dielectric constant for an inhomogeneous medium is applicable only if the constituents (ice crystals and small water pockets, for example) are much smaller in size compared with λ_0. When this condition is satisfied, it also follows that the ***volume scattering coefficient*** κ_s is much smaller than κ_a, in which case $\kappa_e \approx \kappa_a$.

Often, the equivalent-dielectric models of Chapter 4 are used to obtain a first-order, approximate estimate of ε even when the particle's dimensions are not much smaller than λ. A useful parameter in this connection is the ***single-scattering albedo*** of the medium, defined by Eq. (11.21). The contribution of scattering loss to the total extinction may be ignored if $a < 0.01$.

The ***penetration depth*** of a medium with extinction coefficient κ_e is defined as the depth $\delta_p = z$ at which $\mathcal{S}(z) = \mathcal{S}(0)\, e^{-1} = 0.37\mathcal{S}(0)$. Hence,

$$\delta_p = \frac{1}{\kappa_e} \qquad \text{(m)}.$$

For a scatter-free medium, $\delta_p = \delta_s/2$, where δ_s is the skin depth. The factor of 2 arises from the fact that δ_s is defined for the electric field amplitude $E(z)$, whereas δ_p is defined for the power density $\mathcal{S}(z)$, which is proportional to $|E(z)|^2$.

11-5 Radiative Transfer Theory

Two distinct theoretical approaches are available for computing multiple scattering by an inhomogeneous medium: ***analytical theory*** and ***radiative transfer theory*** (also called ***transport theory***). The analytical theory approach, which starts with Maxwell's equations and wave equations, can (in principle) account for all multiple scattering, diffraction, and interference effects, but it is mathematically complicated and computationally demanding.

[†] **Computer Code 11.2.**

► In contrast, the radiative-transfer approach deals with the transport of energy through a medium containing particles and assumes that there is no correlation between the fields scattered by different particles. This assumption allows the incoherent addition of the powers associated with multiple scattering contributions, rather than the addition of their electric fields. ◄

To justify this assumption, the scattering particles should be randomly distributed in location, and the average spacing between them should be sufficiently large (measured in wavelengths) as to ignore mutual coupling between them. Fortunately, most natural media that generate multiple scattering when EM waves pass through them do obey the random distribution requirement. The second requirement, which pertains to the spacing between adjacent scattering particles (such as between two ice crystals in a layer of snow or between two adjacent leaves in a vegetation canopy), is not always satisfied. Nevertheless, with few exceptions, the radiative transfer model has provided results in good agreement with experimental observations.

For an unbounded medium containing spherical particles (such as the atmosphere when viewed by an upward-looking sensor), the polarization state of the wave propagating through the medium becomes irrelevant. Consequently, radiative transfer can be formulated in terms of the scalar specific intensity I, as was done in Section 6-6. For radar, such a formulation leads to a scalar radiative transfer equation of the form

$$\frac{dI(\mathbf{R},\hat{\mathbf{s}})}{ds} = -\kappa_e\, I(\mathbf{R},\hat{\mathbf{s}}) - \kappa_{a,b}\, I(\mathbf{R},\hat{\mathbf{s}}) + \iint_{4\pi} \psi(\hat{\mathbf{s}},\hat{\mathbf{s}}')\, I(\mathbf{R},\hat{\mathbf{s}}')\, d\Omega', \quad (11.26)$$

which is analogous to the combination of Eqs. (6.48), (6.52), and (6.53), without the self-emission contribution $\kappa_a J_a$. This ***scalar radiative transfer equation*** states that propagation through a differential volume of length ds in direction $\hat{\mathbf{s}}$ entails losses (negative signs) and gains (positive signs). The loss due to extinction (absorption and scattering) by the particles is accounted for by κ_e, and the loss due to absorption by the background material (if not lossless) is accounted for by the background absorption coefficient $\kappa_{a,b}$. The last term on the right-hand side of Eq. (11.26) accounts for energy incident from all directions $\hat{\mathbf{s}}'$ (due to bistatic scattering by other volumes) that gets redirected along the original direction $\hat{\mathbf{s}}$ of intensity I (Fig. 11-9). For passive remote sensing, the formulation includes an additional source term that accounts for self emission by the differential volume (Chapter 12).

Most terrestrial media are not composed of spherical particles, which means that scattering by the particles is, in general, wave-polarization dependent. Also, the scattering medium is bounded by a lower surface (ground) and sometimes by an upper surface. Reflection by and transmission across surface boundaries also are polarization dependent. Hence, we should generalize Eq. (11.26) to the ***vector radiative transfer equation***

$$\frac{d\mathbf{I}(\mathbf{R},\hat{\mathbf{s}})}{ds} = -\boldsymbol{\kappa}_e\, \mathbf{I}(\mathbf{R},\hat{\mathbf{s}}) - \kappa_{a,b}\, \mathbf{I}(\mathbf{R},\hat{\mathbf{s}}) + \iint_{4\pi} \boldsymbol{\psi}(\hat{\mathbf{s}},\hat{\mathbf{s}}')\, \mathbf{I}(\mathbf{R},\hat{\mathbf{s}}')\, d\Omega', \quad (11.27)$$

where $\mathbf{I}$ is now a 4×1 vector representing the vector specific intensity of a plane wave with electric field

$$\mathbf{E} = (\hat{\mathbf{v}} E_v + \hat{\mathbf{h}} E_h) e^{-jk\hat{\mathbf{s}}\cdot\mathbf{R}}, \quad (11.28)$$

where $\hat{\mathbf{s}}$ is the propagation direction and $\mathbf{R}$ is a vector from the center of the coordinate system to the location of the differential volume under consideration. From Eq. (5.23a),

$$\mathbf{I} = \begin{bmatrix} I_v \\ I_h \\ U \\ V \end{bmatrix} = \begin{bmatrix} \langle |E_v|^2 \rangle \\ \langle |E_h|^2 \rangle \\ \langle 2\Re\mathrm{e}(E_v E_h^*) \rangle \\ \langle 2\Im\mathrm{m}(E_v E_h^*) \rangle \end{bmatrix} \Big/ \eta, \quad (11.29)$$

where $\langle\ \rangle$ denotes an ensemble average over many independent observations of the distributed target.

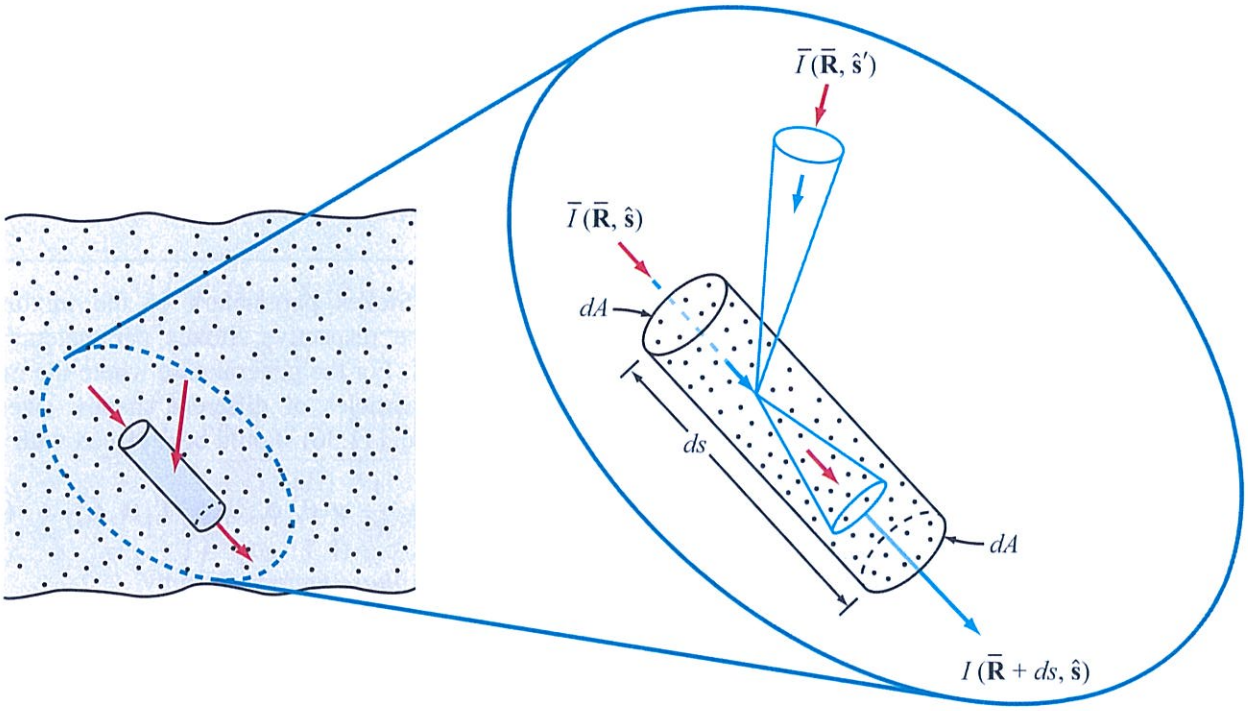

Figure 11-9: Propagation and scattering in a differential volume containing randomly positioned scatterers.

The other quantities printed in bold in Eq. (11.27) are the ***extinction matrix*** $\boldsymbol{\kappa}_e$ and the ***phase matrix*** $\boldsymbol{\psi}$, both of which are 4×4 matrices. Their definitions follow.

11-5.1 Extinction Matrix

For a single particle, the ***optical theorem*** provides a useful relationship for computing the extinction cross section Q_e in terms of elements of the scattering matrix of the particle for scattering in the forward direction, defined by $\theta_s = \theta_i$ and $\phi_s = \phi_i$. If the incident wave is p polarized, where $p = \text{v}$ or h, the extinction cross section of a particle with orientation direction (θ_j, ϕ_j) is

$$Q_e^p = \frac{4\pi}{k} \Im\text{m}[\widetilde{S}_{pp}(\theta_i, \phi_i; \theta_i, \phi_i; \theta_j, \phi_j)], \qquad (11.30)$$

where $k = 2\pi/\lambda$ and $\widetilde{S}_{pp}$ is the pp-scattering amplitude of the particle, defined in the forward scattering alignment (FSA) convention (Section 5-3.1).

The p-polarized extinction coefficient of a medium containing a random distribution of particles may be obtained by performing an ensemble average over the orientations of the particles. Thus,

$$\kappa_e = N_v \langle Q_e^p \rangle, \qquad (11.31)$$

where N_v is the number of particles per unit volume. For spherical particles, κ_e is the same for both polarizations and the extinction matrix is given by the diagonal form

$$\boldsymbol{\kappa}_e = \begin{bmatrix} \kappa_e & 0 & 0 & 0 \\ 0 & \kappa_e & 0 & 0 \\ 0 & 0 & \kappa_e & 0 \\ 0 & 0 & 0 & \kappa_e \end{bmatrix} \quad \textbf{(spheres)}. \qquad (11.32)$$

In the general case when the particles are nonspherical, the extinction matrix assumes the form (Ishimaru and

Cheung, 1980)

$$\boldsymbol{\kappa}_e = \begin{bmatrix} 2\Re e(m_{vv}) & 0 & \Re e(m_{vh}) & \Im m(m_{vh}) \\ 0 & 2\Re e(m_{hh}) & \Re e(m_{hv}) & -\Im m(m_{hv}) \\ 2\Re e(m_{hv}) & \Re e(m_{vh}) & \Re e(m_{vh}+m_{hh}) & \Im m(m_{hh}-m_{vv}) \\ -2\Im m(m_{hv}) & \Im m(m_{vh}) & \Im m(m_{vh}-m_{hh}) & \Re e(m_{vv}+m_{hh}) \end{bmatrix}, \tag{11.33}$$

where

$$m_{pq} = j\left[\frac{2\pi}{k}\right] N_v \left\langle \widetilde{S}_{pq} \right\rangle, \qquad (p,q = \text{v or h}). \tag{11.34}$$

11-5.2 Phase Matrix

From Eq. (5.12) in Section 5-3, the electric field $\mathbf{E}^s$ of the spherical wave scattered by a particle with scattering matrix $\widetilde{\mathbf{S}}$ (defined in the FSA convention) is related to $\mathbf{E}^i$ of the incident plane wave by

$$\begin{bmatrix} E_v^s \\ E_h^s \end{bmatrix} = \left(\frac{e^{-jkR_r}}{R_r}\right) \begin{bmatrix} \widetilde{S}_{vv} & \widetilde{S}_{vh} \\ \widetilde{S}_{hv} & \widetilde{S}_{hh} \end{bmatrix} \begin{bmatrix} E_v^i \\ E_h^i \end{bmatrix}. \tag{11.35}$$

In the same section, we showed that the corresponding vector specific intensities, $\mathbf{I}^s$ and $\mathbf{I}^i$, are related by Eq. (5.24a), namely

$$\mathbf{I}^s = \frac{1}{R_r^2} \widetilde{\mathbf{M}}\, \mathbf{I}^i, \tag{11.36}$$

where $\widetilde{\mathbf{M}}$ is the ***modified Mueller matrix***, repeated here for convenience:

$$\widetilde{\mathbf{M}} = \begin{bmatrix} |\widetilde{S}_{vv}|^2 & |\widetilde{S}_{vh}|^2 & \cdots \\ |\widetilde{S}_{hv}|^2 & |\widetilde{S}_{hh}|^2 & \\ 2\Re e(\widetilde{S}_{vv}\widetilde{S}_{hv}^*) & 2\Re e(\widetilde{S}_{vh}\widetilde{S}_{hh}^*) & \\ 2\Im m(\widetilde{S}_{vv}\widetilde{S}_{hv}^*) & 2\Im m(\widetilde{S}_{vh}\widetilde{S}_{hh}^*) & \end{bmatrix}$$

$$\begin{bmatrix} \Re e(\widetilde{S}_{vv}\widetilde{S}_{vh}^*) & -\Im m(\widetilde{S}_{vv}\widetilde{S}_{vh}^*) \\ \Re e(\widetilde{S}_{hv}\widetilde{S}_{hh}^*) & -\Im m(\widetilde{S}_{hv}\widetilde{S}_{hh}^*) \\ \Re e(\widetilde{S}_{vv}\widetilde{S}_{hh}^* + \widetilde{S}_{vh}\widetilde{S}_{hv}^*) & -\Im m(\widetilde{S}_{vv}\widetilde{S}_{hh}^* - \widetilde{S}_{vh}\widetilde{S}_{hv}^*) \\ \Im m(\widetilde{S}_{vv}\widetilde{S}_{hh}^* + \widetilde{S}_{vh}\widetilde{S}_{hv}^*) & \Re e(\widetilde{S}_{vv}\widetilde{S}_{hh}^* - \widetilde{S}_{vh}\widetilde{S}_{hv}^*) \end{bmatrix}. \tag{11.37}$$

> ▶ One of the fundamental assumptions of radiative transfer theory is that in a medium containing a random distribution of particles, the waves scattered by the particles are random in phase, thereby allowing the addition of the multiple waves incoherently (without regard to their individual phases). ◀

That is, the Stokes parameters of the mixture are the sum of the respective Stokes parameters of the separate waves. For the general case where the medium may contain particles of different shapes, sizes, and orientations, Eq. (11.36) should be replaced with

$$\mathbf{I}^s(\theta_s,\phi_s) = \frac{1}{R_r^2}\, \boldsymbol{\psi}(\theta_s,\phi_s;\theta_i,\phi_i)\, \mathbf{I}^i(\theta_i,\phi_i), \tag{11.38}$$

where $\boldsymbol{\psi}$ is the ***phase matrix*** given by

$$\begin{aligned} \boldsymbol{\psi}(\theta_s,\phi_s;\theta_i,\phi_i) &= N_v \left\langle \widetilde{\mathbf{M}}(\theta_s,\phi_s;\theta_i,\phi_i;x_1,x_2,\ldots,x_n) \right\rangle \\ &= N_v \int \widetilde{\mathbf{M}}(\theta_s,\phi_s;\theta_i,\phi_i;x_1,x_2,\ldots,x_n) \\ &\quad \times p(x_1,x_2,\ldots,x_n)\, dx_1\, dx_2 \ldots dx_n, \end{aligned} \tag{11.39}$$

and $p(x_1,x_2,\ldots,x_n)$ is the joint probability density function over the shape, size, and orientation parameters $(x_1,x_2,\ldots,x_n)$.

11-5.3 Scattering and Absorption Cross Sections

The backscattering cross section of a particle is defined by Eq. (5.30), but the form also applies to the general case of bistatic scattering. Thus, for plane-wave incidence along direction $\hat{\mathbf{i}}$, corresponding to angles (θ_i,ϕ_i), and spherical-wave scattering along direction $\hat{\mathbf{s}}$, corresponding to angles (θ_s,ϕ_s), the pq-polarized bistatic scattering cross section is given by

$$\sigma_{pq}(\hat{\mathbf{s}},\hat{\mathbf{i}}) = 4\pi R_r^2 \frac{\mathcal{S}_p^s(\hat{\mathbf{s}})}{\mathcal{S}_q^i(\hat{\mathbf{i}})}, \qquad (p,q = \text{h or v}), \tag{11.40}$$

where R_r is the distance to the receiver (assumed to be sufficiently large as to satisfy the far-field criterion),

$\mathcal{S}_p^s(\hat{\mathbf{s}})$ is the p-polarized power density of the scattered wave and $\mathcal{S}_q^i(\hat{\mathbf{i}})$ is the q-polarized power density of the incident wave. The p-polarized (total) ***scattering cross section*** of the particle, Q_s^p, is defined as the ratio of the total power scattered by the particle along all directions (which includes both h- and v-polarized waves), divided by the p-polarized incident power density:

$$Q_s^p = \frac{P^s}{\mathcal{S}_p^i(\hat{\mathbf{i}})} = \frac{\iint \left[\mathcal{S}_h^s(\hat{\mathbf{s}}') + \mathcal{S}_v^s(\hat{\mathbf{s}}')\right] dA'}{\mathcal{S}_p^i(\hat{\mathbf{i}})}$$
$$= \frac{\iint_{4\pi} \left[\mathcal{S}_h^s(\hat{\mathbf{s}}') + \mathcal{S}_v^s(\hat{\mathbf{s}}')\right] R_r^2 \, d\Omega_s'}{\mathcal{S}_p^i(\hat{\mathbf{i}})}$$
$$= \frac{1}{4\pi} \iint_{4\pi} \left[\sigma_{hp}(\hat{\mathbf{s}}', \hat{\mathbf{i}}) + \sigma_{vp}(\hat{\mathbf{s}}', \hat{\mathbf{i}})\right] d\Omega_s'. \tag{11.41}$$

In view of the relationship given by Eq. (5.31), namely

$$\sigma_{pq}(\hat{\mathbf{s}}', \hat{\mathbf{i}}) = 4\pi \left|\widetilde{S}_{pq}(\hat{\mathbf{s}}', \hat{\mathbf{i}})\right|^2 \qquad (p = \text{h or v}), \tag{11.42}$$

the expression for Q_s^p becomes

$$Q_s^p = \iint_{4\pi} \left[\left|\widetilde{S}_{hp}(\hat{\mathbf{s}}', \hat{\mathbf{i}})\right|^2 + \left|\widetilde{S}_{vp}(\hat{\mathbf{s}}', \hat{\mathbf{i}})\right|^2\right] d\Omega_s'. \tag{11.43}$$

If the volume has N_v randomly distributed particles per unit volume, then the scattering coefficient of the medium is

$$\kappa_s^p = N_v \langle Q_s^p \rangle. \tag{11.44}$$

The absorption coefficient of the medium is

$$\kappa_a^p = \kappa_e^p - \kappa_s^p = N_v \langle Q_e^p - Q_s^p \rangle, \qquad (p = \text{h or v}), \tag{11.45}$$

where Q_e^p is the extinction cross section given by Eq. (11.30). The p-polarized ***single scattering albedo*** is

$$a^p = \frac{\kappa_s^p}{\kappa_e^p}. \tag{11.46}$$

If the background medium in which the particles are embedded is not air or a lossless dielectric, we can account for the ***background absorption coefficient*** $\kappa_{a,b}$ as follows:

$$\kappa_{a,b} = 2k_0 n_b'' = -2k_0 \, \mathfrak{Im}\left\{\sqrt{\varepsilon_b}\right\}, \tag{11.47}$$

where n_b'' is the imaginary part of the complex index of refraction of the background medium and $k_0 = 2\pi/\lambda_0$. The ***total extinction matrix*** of the medium becomes

$$\boldsymbol{\kappa}_{e,t} = \boldsymbol{\kappa}_e + \boldsymbol{\kappa}_{a,b}, \tag{11.48}$$

where $\boldsymbol{\kappa}_e$ is the extinction matrix of the particles given by Eq. (11.33), and $\boldsymbol{\kappa}_{a,b} = \kappa_{a,b}\mathbf{U}$ and $\mathbf{U}$ is a 4×4 unit matrix.

11-5.4 Applicability Conditions

The radiative transfer equation is formulated on the basis of energy balance. Thus, the phase changes of the scattered wave and its cross-correlation terms are ignored in the solution of the transfer equation. Furthermore, the phase function used in practice comes from the averaging of the magnitude squared of the far-zone scattering amplitudes caused by an individual scatterer or its equivalent. Hence, for the transfer method to apply, the spacing between scatterers in a discrete medium or adjacent inhomogeneities in a continuous medium must be large. An experimental study by Vasalos (1969) shows that for the transfer equation to be applicable, the spacing between scatterers must be larger than $\lambda/3$ and $0.4d$, where λ is the wavelength in the host medium and d is the diameter of the scatterer. Vasalos considered volume fractions as high as 0.295, d/λ ratios from 0.186 to 1.2, and optical thicknesses in the 0.01–3211 range. Additional studies by Hottel et al. (1971) show that a smaller spacing-to-wavelength ratio ($l/\lambda = 0.117$) can be acceptable if the d/λ ratio is larger than 0.23 at a volume fraction of 0.2195 or less. Theoretical studies on the relationship between the radiative transfer approach and the wave approach using Maxwell's equations have been carried out by Fante (1981). Related studies have also been reported by Ishimaru and Kuga (1982).

11-5.5 Phase Matrix of Simple Objects

With the definitions given in the preceding subsections for the phase and extinction matrices, we can, in principle, apply a suitable numerical technique to solve the vector radiative transfer equation given by Eq. (11.27) for a medium with any specified particle distribution and boundary conditions. Because of multiple scattering, each elemental volume within the inhomogeneous medium is coupled to every other elemental volume, and wave propagation in a given direction is coupled to wave propagation along all other directions. Obtaining a numerical solution is doable, but computationally intensive. To avoid the computational challenge, we have two basic options, namely:

(a) to limit the solution to first-order or second-order scattering, as illustrated later in Section 11-6, or

(b) to treat the particles as isotropic point scatterers or as equivalent spherical Rayleigh scatterers, thereby simplifying the forms of the extinction and phase matrices. To justify doing so requires that the wavelength λ be much larger than the particle size. Under such simplifying conditions, it is possible to obtain exact numerical solutions for the vector radiative transfer equation.

Isotropic scatterers

Isotropic point scatterers are characterized by a simple scalar phase function given by

$$\psi = \frac{\kappa_s}{4\pi} = a\,\frac{\kappa_e}{4\pi}, \tag{11.49}$$

where $a = \kappa_s/\kappa_e$ is the single scattering albedo. Note that ψ is independent of both polarization and incidence angle.

Spherical Rayleigh scatterers

If an ice crystal is not spherical in shape but small in size relative to λ, it may be modeled as an equivalent sphere with the same size and mass as the actual crystal. In principle, this equivalency can also be applied to other types of scattering particle, such as small leaves and needles in vegetation canopies. Scattering by a sphere of radius r and relative index of refraction n can be computed using the Rayleigh approximation, which yields acceptable accuracies so long as the product of n and the parameter $\chi = kr = 2\pi r/\lambda_b$ satisfies the condition

$$|n\chi| = \left|\frac{2\pi n}{\lambda_b}\,r\right| < 0.5, \tag{11.50}$$

where λ_b is the wavelength in the background medium and $n = n_p/n_b$ (with n_p and n_b being the indices of refraction of the particle and background, respectively). The phase matrix of a random medium containing spherical Rayleigh scatterers with incidence along (θ_i, ϕ_i) and scattering along (θ_s, ϕ_s), as shown in Fig. 11-10, is given by (Tsang et al., 1985, pp. 157–158):

$$\boldsymbol{\psi}(\phi_s, \theta_s; \phi_i, \theta_i) = \begin{bmatrix} \psi_{11} & \psi_{12} & \psi_{13} & 0 \\ \psi_{21} & \psi_{22} & \psi_{23} & 0 \\ \psi_{31} & \psi_{32} & \psi_{33} & 0 \\ 0 & 0 & 0 & \psi_{44} \end{bmatrix}, \tag{11.51}$$

where

$$\begin{aligned}
\psi_{11} &= b[\sin^2\theta_s \sin^2\theta_i + \cos^2\theta_s \cos^2\theta_i \cos^2(\phi_s - \phi_i) \\
&\quad + 2\sin\theta_s \sin\theta_i \cos\theta_s \cos\theta_i \cos(\phi_s - \phi_i)], \\
\psi_{12} &= b\cos^2\theta_s \sin^2(\phi_s - \phi_i), \\
\psi_{13} &= b[\cos\theta_s \sin\theta_s \sin\theta_i \sin(\phi_s - \phi_i) \\
&\quad + \cos^2\theta_s \cos\theta_i \sin(\phi_s - \phi_i)\cos(\phi_s - \phi_i)], \\
\psi_{21} &= b\cos^2\theta_i \sin^2(\phi_s - \phi_i), \\
\psi_{22} &= b\cos^2(\phi_s - \phi_i), \\
\psi_{23} &= -b\cos\theta_s \sin(\phi_s - \phi_i)\cos(\phi_s - \phi_i), \\
\psi_{31} &= b[-2\sin\theta_s \sin\theta_i \cos\theta_i \sin(\phi_s - \phi_i) \\
&\quad - 2\cos\theta_s \cos^2\theta_i \cos(\phi_s - \phi_i)\sin(\phi_s - \phi_i)], \\
\psi_{32} &= 2b\cos\theta_s \sin(\phi_s - \phi_i)\cos(\phi_s - \phi_i)], \\
\psi_{33} &= b\{\sin\theta_s \sin\theta_i \cos(\phi_s - \phi_i) \\
&\quad + \cos\theta_s \cos\theta_i[\cos^2(\phi_s - \phi_i) - \sin^2(\phi_s - \phi_i)]\}, \\
\psi_{44} &= b[\sin\theta_s \sin\theta_i \cos(\phi_s - \phi_i) + \cos\theta_s \cos\theta_i], \\
b &= \frac{3}{8\pi}\,\kappa_s,
\end{aligned}$$

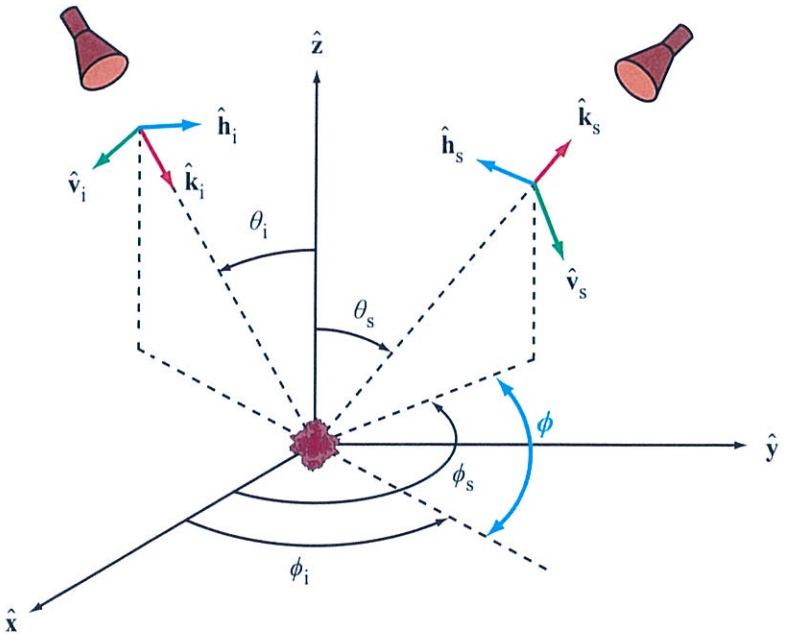

Figure 11-10: Incident and scattering directions for a point scatterer.

and κ_s is the scattering coefficient.

From Eq. (8.45a),

$$\begin{aligned}\kappa_s = N_v Q_s &= \frac{2\lambda^2}{3\pi} N_v \chi^6 |K|^2 \\ &= \frac{8\pi}{3} N_v k^4 r^6 |K|^2 \\ &= 2\upsilon k^4 r^3 |K|^2, \end{aligned} \tag{11.52}$$

where $k = 2\pi/\lambda_b$, N_v is the number density of particles (in #/m^3), υ is the ***volume fraction*** of scatterers,

$$\upsilon = \left(\frac{4}{3}\pi r^3\right) N_v, \tag{11.53}$$

and K is defined by Eq. (8.43) as

$$K = \frac{n^2 - 1}{n^2 + 2} = \frac{\varepsilon - 1}{\varepsilon + 2}, \tag{11.54}$$

where $\varepsilon = n^2 = \varepsilon_p/\varepsilon_b$.

The phase matrix describes the bistatic scattering pattern of Rayleigh particles, while accounting for the polarization directions of the incident and scattered waves. In the ***plane of incidence*** ($\phi_s = \phi_i$), all nondiagonal terms are zero, and the diagonal terms simplify to

$$\psi_{11} = \frac{3\kappa_s}{8\pi} (\sin\theta_s \sin\theta_i + \cos\theta_s \cos\theta_i)^2, \tag{11.55a}$$

$$\psi_{22} = \frac{3\kappa_s}{8\pi}, \tag{11.55b}$$

$$\psi_{33} = \psi_{44} = \frac{3\kappa_s}{8\pi} (\sin\theta_s \sin\theta_i + \cos\theta_s \cos\theta_i). \tag{11.55c}$$

Moreover, if $\theta_s = \theta_i$ (in addition to $\phi_s = \phi_i$),

$$\psi_{11} = \psi_{22} = \psi_{33} = \psi_{44} = \frac{3\kappa_s}{8\pi}. \tag{11.56}$$

From Eq. (8.45a), the absorption coefficient is given by

$$\begin{aligned}\kappa_a = N_v Q_a &= \frac{\lambda^2}{\pi} N_v \chi^3 \, \Im\mathrm{m}[-K] \\ &= 3\upsilon k \, \Im\mathrm{m}[-K] = 3\upsilon k \frac{\varepsilon''}{|\varepsilon + 2|^2}. \end{aligned} \tag{11.57}$$

The extinction coefficient due to the particles is $\kappa_e = \kappa_s + \kappa_a$, and the extinction matrix is diagonal with each element equal to κ_e, as in Eq. (11.32).

11-5.6 Boundary Conditions for a Planar Interface

When the specific intensity impinges upon the boundary separating two media with different dielectric constants, part of the incident energy is reflected and the remaining part is transmitted across the boundary. In this section, we consider the boundary conditions relating the Stokes parameters of the specific intensities in the two media.

If the boundary is a planar dielectric interface, scattering at the boundary occurs in only the specular direction and does not include a diffuse component. If the boundary is rough, however, the incident wave is scattered in all directions at the boundary and the incident intensity is coupled into all of the reflected and transmitted directions. However, if the scattering albedo of the particles contained in the scattering layer is larger than about 0.3, the numerical approach to solving the radiative transfer equation is the only viable technique for obtaining reasonably accurate results; the iterative-solution approach is inadequate for $a \gtrsim 0.3$. Nevertheless, in this book, we limit our discussion to the smooth-boundary case. For examination of the boundary conditions associated with a rough surface, we refer the interested reader to the article by Fung and Eom (1981), who investigated radar scattering from a layer of Rayleigh particles over a rough surface by using the Kirchhoff approximation, and to the books by Tsang et al. (1985) and Fung and Chen (2010).

For a plane wave incident upon a planar boundary from medium 1 to medium 2, as shown in Fig. 11-11, the expressions for the Fresnel reflection and transmission coefficients and associated reflectivities and transmissivities given in Table 2-5 can be written in the form:

$$\rho_h = \frac{n_1 \cos\theta_1 - n_2 \cos\theta_2}{n_1 \cos\theta_1 + n_2 \cos\theta_2}, \tag{11.58a}$$

$$\rho_v = \frac{n_1 \cos\theta_2 - n_2 \cos\theta_1}{n_1 \cos\theta_2 + n_2 \cos\theta_1}, \tag{11.58b}$$

$$\tau_h = 1 + \rho_h, \qquad \tau_v = (1 + \rho_v)\frac{\cos\theta_1}{\cos\theta_2} \tag{11.58c}$$

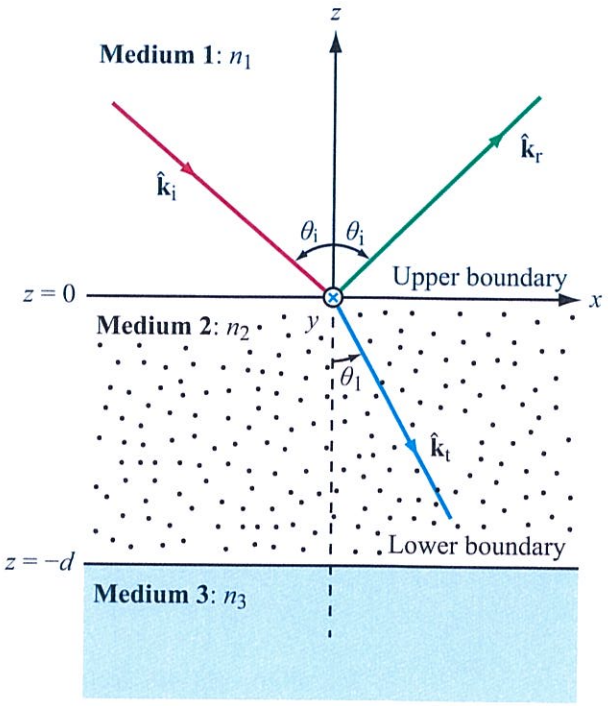

Figure 11-11: Incidence in medium 1 with index of refraction n_1 upon medium 2 with index of refraction n_2.

$$\Gamma^h = |\rho_h|^2, \qquad \Gamma^v = |\rho_v|^2, \tag{11.58d}$$

$$\mathbb{T}^h = 1 - \Gamma^h, \qquad \mathbb{T}^v = 1 - \Gamma^v, \tag{11.58e}$$

where n_1 and n_2 are the indices of refraction of media 1 and 2, respectively, and angles θ_1 and θ_2 are related by Snell's law:

$$n_2 \sin\theta_2 = n_1 \sin\theta_1. \tag{11.59}$$

The vector specific intensity $\mathbf{I}$ of a propagating wave is defined in Eq. (11.29) in terms of the h- and v-polarized components of the wave's electric field. Using superscripts $\mathbf{I}^i$, $\mathbf{I}^r$, and $\mathbf{I}^t$ to denote the incident, reflected, and transmitted specific intensities, the relationships between them are given by Ishimaru (1978) as

$$\mathbf{I}^r = \mathbb{R}\mathbf{I}^i, \tag{11.60a}$$

and

$$\mathbf{I}^t = \mathbb{T}\mathbf{I}^i, \tag{11.60b}$$

where $\mathbb{R}$ and $\mathbb{T}$ are ***reflectivity*** and ***transmissivity matrices*** given by

$$\mathbb{R} = \begin{bmatrix} \Gamma^{v} & 0 & 0 & 0 \\ 0 & \Gamma^{h} & 0 & 0 \\ 0 & 0 & \Re e(\rho_v \rho_h^*) & -\Im m(\rho_v \rho_h^*) \\ 0 & 0 & \Im m(\rho_v \rho_h^*) & \Re e(\rho_v \rho_h^*) \end{bmatrix} \tag{11.61a}$$

and

$$\mathbb{T} = \frac{n_2^3 \cos\theta_2}{n_1^3 \cos\theta_1} \begin{bmatrix} |\tau_v|^2 & 0 & 0 & 0 \\ 0 & |\tau_v|^2 & 0 & 0 \\ 0 & 0 & \Re e(\tau_v \tau_h^*) & -\Im m(\tau_v \tau_h^*) \\ 0 & 0 & \Im m(\tau_v \tau_h^*) & \Re e(\tau_v \tau_h^*) \end{bmatrix}. \tag{11.61b}$$

11-6 Iterative Solution of the Radiative Transfer Equation

Except for some special cases, the vector radiative transfer equation does not have an analytical solution. The approximations and numerical techniques used for solving the radiative transfer equation include the ***iterative-solution technique*** and the ***discrete-ordinate technique*** (Chandrasekhar, 1960; Ishimaru, 1978; Tsang et al., 1985; Ulaby et al., 1986a; Fung, 1994). In the iterative approach, the radiative transfer equation is cast into an integral form, and then solved iteratively to obtain the zero-, first-, and second-order solutions. In principle, we can obtain an accurate solution by iterating many times. In practice, however, iteration beyond the second-order solution is not necessary.

The discrete-ordinate eigenanalysis technique provides good numerical solutions for the radiative transfer equation (Ishimaru et al., 1982; Ulaby et al., 1986a) and has been used extensively in the literature. In this technique, the specific intensity and phase matrix are first discretized into a finite number of directions by means of quadrature, and the resulting matrix equation is solved by eigenanalysis.

In addition to these, several other techniques have been applied to solve the radiative transfer equation, including the invariant-embedding method and the finite-difference method (Tsang et al., 1985). The major limitation of these numerical techniques is the fact that they are computationally very demanding, particularly if the angular variation of the phase matrix is very complex. However, if the scattering albedo a of the particles contained in the scattering layer is larger than about 0.3, the numerical approach to solving the radiative transfer equation is the only viable technique for obtaining reasonably accurate results; the iterative-solution approach is inadequate for $a \gtrsim 0.3$. Nevertheless, in this book, we limit our presentation to the iterative method.

11-6.1 Iterative-Solution Method

The iterative method is applicable when the random medium is ***weakly scattering***; that is, when the albedo a is small. The procedure starts by computing the ***zero-order solution***, which ignores scattering, except for its contribution to extinction. The zero-order solution then serves as a ***source function*** for computing the first-order solution, and then the first-order solution becomes the source function for the second-order solution.

To illustrate the mechanics of the iterative solution method, we consider the simple three-layer case shown in Fig. 11-12, in which:

(a) the middle layer contains uniformly distributed spherical particles, which reduces the extinction matrix $\boldsymbol{\kappa}_e$ into the product of a unitary diagonal matrix and the scalar extinction coefficient κ_e,

(b) the upper boundary is diffuse, which means that no reflection occurs at the top interface at $z = 0$, and

(c) the bottom boundary is flat, which means that only specular reflection occurs at the lower interface at $z = -d$.

The incident specific intensity is $\mathbf{I}_0^i(-\mu_i, \phi_i)$, where $\mu_i = \cos\theta_i$ and $-\mu_i = \cos(\pi - \theta_i)$. Thus, μ_i denotes an upward propagating wave and $-\mu_i$ denotes a downward propagating wave. The total backscattered intensity is denoted $\mathbf{I}^s(\mu_i, \phi_i + \pi)$, which is related to the incident intensity $\mathbf{I}_0^i$ by

$$\mathbf{I}^s(\mu_i, \phi_i + \pi) = \boldsymbol{\mathcal{T}}_t(\mu_i, \phi_i + \pi; -\mu_i, \phi_i)\, \mathbf{I}_0^i(-\mu_i, \phi_i), \tag{11.62}$$

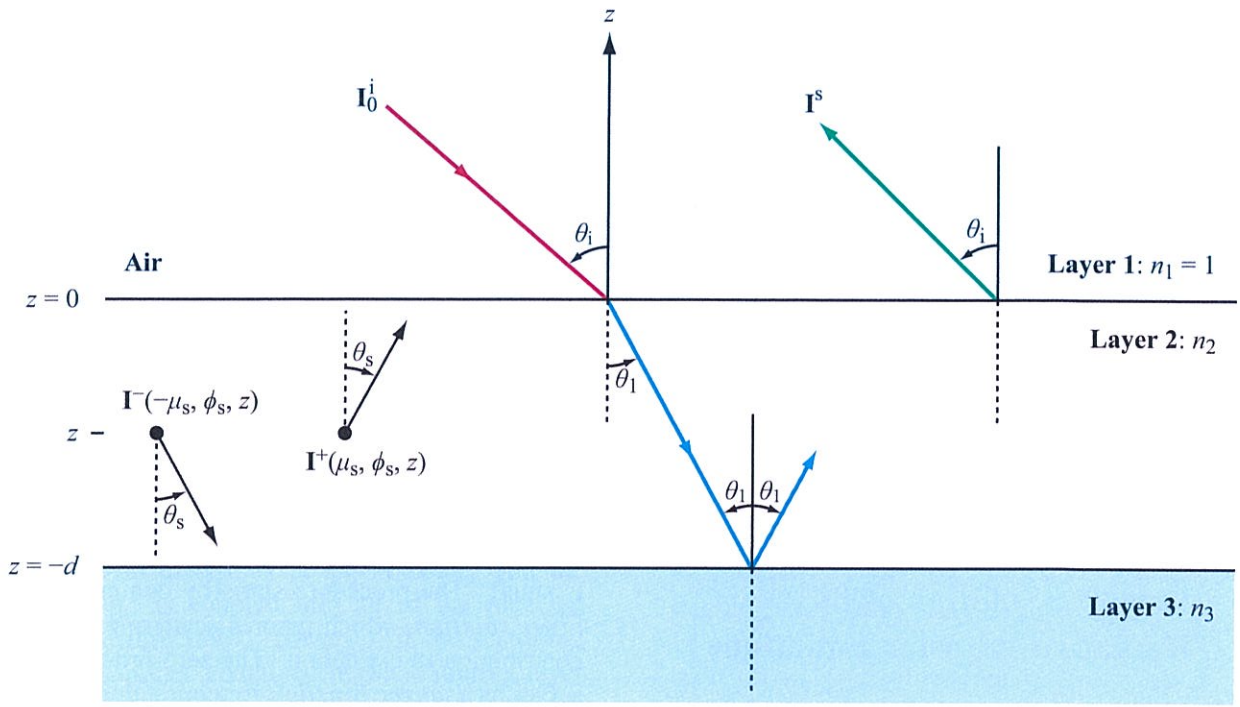

Figure 11-12: Incident vector intensity $\mathbf{I}_0^i$, downward and upward propagating intensities $\mathbf{I}^-$ and $\mathbf{I}^+$, and backscattered intensity $\mathbf{I}^s$.

where $\mathcal{T}_t(\mu_i, \phi_i + \pi; -\mu_i, \phi_i)$ is a ***total backscattering transformation matrix***. The goal of the radiative-transfer solution is to obtain an expression for $\mathcal{T}_t$ for downward incidence along $(-\mu_i, \phi_i)$ and upward backscattering along $(\mu_i, \phi_i + \pi)$. However, because the bottom boundary is assumed to be flat, the radiative transfer model does not account for the attenuated direct backscatter from the bottom surface.

Given $\mathcal{T}_t$, the backscattering coefficients for vv, hh, and hv polarizations are given by

$$\sigma^0_{vv}(\theta_i) = \Upsilon^2\, \sigma^0_{s_{vv}}(\theta_i) + 4\pi \cos\theta_i [\mathcal{T}_t]_{11}, \quad (11.63a)$$

$$\sigma^0_{hh}(\theta_i) = \Upsilon^2\, \sigma^0_{s_{hh}}(\theta_i) + 4\pi \cos\theta_i [\mathcal{T}_t]_{22}, \quad (11.63b)$$

$$\sigma^0_{hv}(\theta_i) = \Upsilon^2\, \sigma^0_{s_{hv}}(\theta_i) + 4\pi \cos\theta_i [\mathcal{T}_t]_{21}, \quad (11.63c)$$

where Υ^2 is the two-way transmissivity of the middle layer and $\sigma^0_{s_{pq}}$ is the backscattering coefficient of the bottom surface in the absence of the middle layer.

To compute the backscattering coefficient for other receive/transmit polarization combinations of interest, we can use the polarization synthesis technique of Section 5-11.3. The parallel to the formulation given by Eq. (5.150) is

$$\sigma^0_{rt}(\psi_r, \chi_r; \psi_t, \chi_t) = \Upsilon^2\, \sigma^0_{s_{rt}}(\theta_i) + 4\pi \cos\theta_i\, \mathbf{I}^r_n \cdot \mathbf{Q}\, \mathcal{T}_t \mathbf{I}^t_n, \quad (11.64)$$

where $\mathbf{I}^r_n$ and $\mathbf{I}^t_n$ describe the polarizations of the received and transmitted waves and are defined by Eq. (5.145), and $\mathbf{Q}$ is a 4×4 matrix given by Eq. (5.149).

11-6.2 Upward- and Downward-Propagating Intensities

We start by designating $\mathbf{I}^+(\mu_s, \phi_s, z)$ as the ***upward-propagating intensity*** at depth z, along direction (μ_s, ϕ_s). Similarly, $\mathbf{I}^-(-\mu_s, \phi_s, z)$ is the ***downward-propagating intensity*** along $(-\mu_s, \phi_s)$. Inside the middle layer, the

intensities $\mathbf{I}^+$ and $\mathbf{I}^-$ must satisfy the coupled radiative transfer equations:

$$\frac{d}{dz}\mathbf{I}^+(\mu_s,\phi_s,z) = -\frac{\kappa_e}{\mu_s}\mathbf{I}^+(\mu_s,\phi_s,z) + \mathcal{F}^+(\mu_s,\phi_s,z), \tag{11.65a}$$

$$-\frac{d}{dz}\mathbf{I}^-(-\mu_s,\phi_s,z) = -\frac{\kappa_e}{\mu_s}\mathbf{I}^-(-\mu_s,\phi_s,z) + \mathcal{F}^-(-\mu_s,\phi_s,z). \tag{11.65b}$$

Note that $d\mathbf{I}^-/dz$ is preceded by a minus sign in Eq. (11.65b). This is because the direction of propagation is along $-\mu_s$. This pair of equations is obtained from Eq. (11.27) by (a) replacing the lateral distance ds with $dz\sec\theta_s$, (b) using Eq. (11.32) for $\boldsymbol{\kappa}_e$, thereby, in essence, replacing $\boldsymbol{\kappa}_e$ with the scalar extinction coefficient κ_e, (c) either deleting the background absorption term in Eq. (11.27) because the background dielectric in the middle layer is lossless, in which case $\kappa_{a,b} = 0$, or including $\kappa_{a,b}$ in κ_e if the background dielectric is not lossless, and (d) denoting the term that includes the phase matrix as $\mathcal{F}^+$ for upward propagation and denoting it as $\mathcal{F}^-$ for downward propagation. Thus, $\mathcal{F}^+$ and $\mathcal{F}^-$ are ***source functions*** that account for directing the energy incident upon an elemental volume from all directions into directions (θ_s,ϕ_s) and $(\pi-\theta_s,\phi_s)$, respectively. They are given by

$$\mathcal{F}^+(\mu_s,\phi_s,z) = \frac{1}{\mu_s}\left[\int_0^{2\pi}\int_0^1 \boldsymbol{\psi}(\mu_s,\phi_s;\mu',\phi')\,\mathbf{I}^+(\mu',\phi',z)\,d\Omega' + \int_0^{2\pi}\int_0^1 \boldsymbol{\psi}(\mu_s,\phi_s;-\mu',\phi')\,\mathbf{I}^-(-\mu',\phi',z)\,d\Omega'\right], \tag{11.66a}$$

$$\mathcal{F}^-(-\mu_s,\phi_s,z) = \frac{1}{\mu_s}\left[\int_0^{2\pi}\int_0^1 \boldsymbol{\psi}(-\mu_s,\phi_s;\mu',\phi')\,\mathbf{I}^+(\mu',\phi',z)\,d\Omega' + \int_0^{2\pi}\int_0^1 \boldsymbol{\psi}(-\mu_s,\phi_s;-\mu',\phi')\,\mathbf{I}^-(-\mu',\phi',z)\,d\Omega'\right], \tag{11.66b}$$

where

$$d\Omega' = d\mu'\,d\phi' = \sin\theta'\,d\theta'\,d\phi'$$

and $\boldsymbol{\psi}(\mu_s,\phi_s;\mu',\phi')$ is the phase matrix of the middle layer.

The boundary conditions are

$$\mathbf{I}^-(-\mu_s,\ \phi_s,\ z=0) = \mathbf{I}_0^i\,\delta(\mu_s-\mu_i)\,\delta(\phi_s-\phi_i), \tag{11.67a}$$

$$\mathbf{I}^+(\mu_s,\ \phi_s,\ z=-d) = \mathbb{R}(\mu_s)\,\mathbf{I}^-(-\mu_s,\ \phi_s,\ z=-d), \tag{11.67b}$$

where $\mathbf{I}_0^i$ is the specific intensity incident in medium 1 along the direction (μ_i,ϕ_i) and $\mathbb{R}(\mu_s)$ is the reflectivity matrix at $z=-d$ at angle μ_s. The expression for $\mathbb{R}(\mu_s)$ is given by Eq. (11.61a). Repeat of the steps used in Section 6-6.3 leads to the following general solution for Eqs. (11.65a and b):

$$\mathbf{I}^+(\mu_s,\phi_s,z) = e^{-\kappa_e(z+d)/\mu_s}\,\mathbf{I}^+(\mu_s,\ \phi_s,\ z=-d) + \int_{-d}^{z} e^{-\kappa_e(z-z')/\mu_s}\,\mathcal{F}^+(\mu_s,\ \phi_s,\ z')\,dz', \tag{11.68a}$$

$$\mathbf{I}^-(-\mu_s,\phi_s,z) = e^{\kappa_e z/\mu_s}\,\mathbf{I}^-(-\mu_s,\ \phi_s,\ z=0) + \int_{z}^{0} e^{\kappa_e(z-z')/\mu_s}\,\mathcal{F}^-(-\mu_s,\ \phi_s,\ z')\,dz', \tag{11.68b}$$

By applying the boundary conditions given by Eqs. (11.67a and b), we have

$$\mathbf{I}^+(\mu_s,\phi_s,z) = e^{-\kappa_e(z+d)/\mu_s}\,\mathbb{R}(\mu_i)\,e^{-\kappa_e d/\mu_i}\mathbf{I}_0^i\,\delta(\mu_s-\mu_i)\,\delta(\phi_s-\phi_i) \cdot e^{-\kappa_e(z+d)/\mu_s}\,\mathbb{R}(\mu_s)\int_{-d}^{z} e^{\kappa_e(-d-z')/\mu_s}\,\mathcal{F}^-(-\mu_s,\phi_s,z')\,dz' + \int_{-d}^{z} e^{-\kappa_e(z-z')/\mu_s}\,\mathcal{F}^+(-\mu_s,\phi_s,z')\,dz', \tag{11.69a}$$

$$\mathbf{I}^-(-\mu_s,\phi_s,z) = e^{\kappa_e z/\mu_i}\mathbf{I}_0^i\,\delta(\mu_s-\mu_i)\,\delta(\phi_s-\phi_i) + \int_{z}^{0} e^{\kappa_e(z-z')/\mu_s}\,\mathcal{F}^-(-\mu_s,\phi_s,z')\,dz'. \tag{11.69b}$$

In the iterative approach, the solutions are expanded into a series of perturbation orders:

$$\mathbf{I}(\mu,\phi,z) = \mathbf{I}_0(\mu,\phi,z) + \mathbf{I}_1(\mu,\phi,z) + \mathbf{I}_2(\mu,\phi,z) + \cdots, \tag{11.70}$$

where $-1 < \mu < 1$. Because the scattering is treated as an iterative parameter, the perturbation orders have one-to-one correspondence with the multiple scattering process. The solution $\mathbf{I}_0$ represents reduced incident intensity, $\mathbf{I}_1$ represents the single scattering solution, and $\mathbf{I}_2$ represents the double scattering solution. The iterative solution method is applicable only when the medium's single scattering albedo $a = \kappa_s/\kappa_e$ is small (i.e., $a \lesssim 0.2$).

11-6.3 Zeroth-Order Solution

The zeroth-order solution is obtained by setting $\mathcal{F}^+ = 0$ and $\mathcal{F}^- = 0$ in Eqs. (11.69a and b):

$$\mathbf{I}_0^-(-\mu_s,\phi_s,z) = e^{\kappa_e z/\mu_i}\mathbf{I}_0^i\,\delta(\mu_s-\mu_i)\,\delta(\phi_s-\phi_i), \tag{11.71a}$$

$$\mathbf{I}_0^+(\mu_s,\phi_s,z) = e^{-\kappa_e(z+d)/\mu_i}\,\mathbb{R}\,e^{-\kappa_e d/\mu_i}\mathbf{I}_0^i \cdot \delta(\mu_s-\mu_i)\,\delta(\phi_s-\phi_i). \tag{11.71b}$$

The impulse functions in Eq. (11.71a) specify the direction of the incident wave, and the impulse functions in Eq. (11.71b) specify that reflection by the lower boundary occurs only along the specular direction.

> ► The zeroth-order solution is simply the ***reduced incident intensity***, which attenuates exponentially inside the medium. Scattering is not included, except for its contribution to extinction. ◄

11-6.4 First-Order Solution

Use of the zeroth-order solutions given by Eq. (11.71) in Eq. (11.66) leads to the zeroth-order source functions:

$$\begin{aligned}
&\mathcal{F}_0^+(\mu_s,\phi_s,z) \\
&= \frac{1}{\mu_s}\left[\int_0^{2\pi}\int_0^1 \boldsymbol{\psi}(\mu_s,\phi_s;\mu',\phi')\,\mathbf{I}_0^+(\mu',\phi',z)\,d\Omega'\right. \\
&\qquad \left.\int_0^{2\pi}\int_0^1 \boldsymbol{\psi}(\mu_s,\phi_s;-\mu',\phi')\,\mathbf{I}_0^-(-\mu',\phi',z)\,d\Omega'\right] \\
&= \frac{1}{\mu_s}\left[\int_0^{2\pi}\int_0^1 \boldsymbol{\psi}(\mu_s,\phi_s;\mu',\phi')\,e^{-\kappa_e(z+d)/\mu_i}\,\mathbb{R}(\mu_i)\right. \\
&\qquad \cdot e^{-\kappa_e d/\mu_i}\mathbf{I}_0^i\,\delta(\mu'-\mu_i)\,\delta(\phi'-\phi_i)\,d\Omega' \\
&\qquad + \int_0^{2\pi}\int_0^1 \boldsymbol{\psi}(\mu_s,\phi_s;-\mu',\phi')\,e^{\kappa_e z/\mu_i}\,\mathbf{I}_0^i \\
&\qquad \left.\cdot\,\delta(\mu'-\mu_i)\,\delta(\phi'-\phi_i)\,d\Omega'\right] \\
&= \left[e^{-\kappa_e(z+2d)/\mu_i}\,\boldsymbol{\psi}(\mu_s,\phi_s;\mu_i,\phi_i)\,\mathbb{R}(\mu_i)\right. \\
&\qquad \left.+e^{\kappa_e z/\mu_i}\,\boldsymbol{\psi}(\mu_s,\phi_s;-\mu_i,\phi_i)\,\mathbb{R}(\mu_i)\right]\frac{\mathbf{I}_0}{\mu_s},
\end{aligned} \tag{11.72a}$$

$$\begin{aligned}
&\mathcal{F}_0^-(-\mu_s,\phi_s,z) \\
&= \frac{1}{\mu_s}\left[\int_0^{2\pi}\int_0^1 \boldsymbol{\psi}(-\mu_s,\phi_s;\mu',\phi')\,\mathbf{I}_0^+(\mu',\phi',z)\,d\Omega'\right. \\
&\qquad \left.\int_0^{2\pi}\int_0^1 \boldsymbol{\psi}(-\mu_s,\phi_s;-\mu',\phi')\,\mathbf{I}_0^-(-\mu',\phi',z)\,d\Omega'\right] \\
&= \frac{1}{\mu_s}\left[\int_0^{2\pi}\int_0^1 \boldsymbol{\psi}(-\mu_s,\phi_s;\mu',\phi')\,e^{-\kappa_e(z+d)/\mu_i}\,\mathbb{R}(\mu_i)\right. \\
&\qquad \cdot e^{-\kappa_e d/\mu_i}\mathbf{I}_0^i\,\delta(\mu'-\mu_i)\,\delta(\phi'-\phi_i)\,d\Omega' \\
&\qquad + \int_0^{2\pi}\int_0^1 \boldsymbol{\psi}(-\mu_s,\phi_s;-\mu',\phi')\,e^{\kappa_e z/\mu_i}\,\mathbf{I}_0^i \\
&\qquad \left.\cdot\,\delta(\mu'-\mu_i)\,\delta(\phi'-\phi_i)\,d\Omega'\right] \\
&= \left[e^{-\kappa_e(z+2d)/\mu_i}\,\boldsymbol{\psi}(-\mu_s,\phi_s;\mu_i,\phi_i)\,\mathbb{R}(\mu_i)\right. \\
&\qquad \left.+e^{\kappa_e z/\mu_i}\,\boldsymbol{\psi}(-\mu_s,\phi_s;-\mu_i,\phi_i)\,\mathbb{R}(\mu_i)\right]\frac{\mathbf{I}_0}{\mu_s}.
\end{aligned} \tag{11.72b}$$

To obtain the first-order solutions for the upward- and downward-propagating intensities, $\mathbf{I}_1^+$ and $\mathbf{I}_1^-$, we insert the zeroth-order source functions given by Eq. (11.72)

into Eq. (11.69):

$$\begin{aligned}
\mathbf{I}_1^+(\mu_s,\phi_s,z) = {} & e^{-\kappa_e(z+2d)/\mu_i}\,\mathbb{R}(\mu_i)\,\mathbf{I}_0^i\,\delta(\mu_s-\mu_i)\,\delta(\phi_s-\phi_i) \\
& + e^{-\kappa_e(z+d)/\mu_s}\,\mathbb{R}(\mu_s)\int_{-d}^{z} e^{\kappa_e(-d-z')/\mu_s} \\
& \cdot\Big[e^{-\kappa_e(z'+2d)/\mu_i}\,\boldsymbol{\psi}(-\mu_s,\phi_s;\mu_i,\phi_i)\,\mathbb{R}(\mu_i) \\
& \quad + e^{\kappa_e z'/\mu_i}\,\boldsymbol{\psi}(-\mu_s,\phi_s;-\mu_i,\phi_i)\Big]\frac{\mathbf{I}_0^i}{\mu_s}\,dz' \\
& + \int_{-d}^{z} e^{-\kappa_e(z-z')/\mu_s} \\
& \cdot\Big[e^{-\kappa_e(z'+2d)/\mu_i}\,\boldsymbol{\psi}(\mu_s,\phi_s;\mu_i,\phi_i)\,\mathbb{R}(\mu_i) \\
& \quad + e^{\kappa_e z'/\mu_i}\,\boldsymbol{\psi}(\mu_s,\phi_s;-\mu_i,\phi_i)\Big]\frac{\mathbf{I}_0^i}{\mu_s}\,dz' \qquad (11.73a)
\end{aligned}$$

and

$$\begin{aligned}
\mathbf{I}_1^-(-\mu_s,\phi_s,z) = {} & e^{\kappa_e z/\mu_i}\mathbf{I}_0^i\,\delta(\mu_s-\mu_i)\,\delta(\phi_s-\phi_i) \\
& + \int_{z}^{0} e^{\kappa_e(z-z')/\mu_s} \\
& \cdot\Big[e^{-\kappa_e(z'+2d)/\mu_i}\,\boldsymbol{\psi}(-\mu_s,\phi_s;\mu_i,\phi_i)\,\mathbb{R}(\mu_i) \\
& \quad + e^{\kappa_e z'/\mu_i}\,\boldsymbol{\psi}(-\mu_s,\phi_s;-\mu_i,\phi_i)\Big]\frac{\mathbf{I}_0^i}{\mu_s}\,dz'. \qquad (11.73b)
\end{aligned}$$

The expressions given by Eq. (11.73) are applicable at any height z within the middle layer and for any direction (μ_s,ϕ_s) for $\mathbf{I}_1^+$ and $(-\mu_s,\phi_s)$ for $\mathbf{I}_1^-$. To compute the backscattering coefficient $\sigma_{pq}^0(\theta_i)$, we should set $z=0$, $\mu_s=\mu_i$ and $\phi_s=\pi+\phi_i$ in Eq. (11.73a), which leads to

$$\begin{aligned}
\mathbf{I}_1^+(\theta_i,\phi_i,0) = {} & e^{-2\kappa_e d/\mu_i}\,\mathbb{R}(\mu_i)\,\mathbf{I}_0^i\,\delta(\phi_s-\phi_i=\pi) \\
& + \Bigg[e^{-4\kappa_e d/\mu_i}\,\mathbb{R}(\mu_i)\,\boldsymbol{\psi}(-\mu_i,\phi_i+\pi;\mu_i,\phi_i)\,\mathbb{R}(\mu_i) \\
& \quad \cdot\int_{-d}^{0} e^{-2\kappa_e z'/\mu_i}\,dz' \\
& + e^{-2\kappa_e d/\mu_i}\,\boldsymbol{\psi}(-\mu_i,\phi_i+\pi;-\mu_i,\phi_i)\,\mathbb{R}(\mu_i)\int_{-d}^{0} dz' \\
& + e^{-2\kappa_e d/\mu_i}\,\mathbb{R}(\mu_i)\,\boldsymbol{\psi}(\mu_i,\phi_i+\pi;\mu_i,\phi_i)\int_{-d}^{0} dz' \\
& + \boldsymbol{\psi}(\mu_i,\phi_i+\pi;-\mu_i,\phi_i)\int_{-d}^{0} e^{2\kappa_e z'/\mu_i}\,dz'\Bigg]\frac{\mathbf{I}_0^i}{\mu_i} \\
= {} & \Upsilon^2\,\mathbb{R}(\theta_i)\,\mathbf{I}_0^i\,\delta(\phi_s-\phi_i=\pi) \\
& + \Bigg[\Upsilon^2\,\mathbb{R}(\theta_i)\,\boldsymbol{\psi}(-\mu_i,\phi_i+\pi;\mu_i,\phi_i)\,\mathbb{R}(\theta_i)\,\frac{\mu_i}{2\kappa_e}\,(1-\Upsilon^2) \\
& + d\,\Upsilon^2\,\boldsymbol{\psi}(-\mu_i,\phi_i+\pi;-\mu_i,\phi_i)\,\mathbb{R}(\theta_i) \\
& + d\,\Upsilon^2\,\mathbb{R}(\theta_i)\,\boldsymbol{\psi}(\mu_i,\phi_i+\pi;\mu_i,\phi_i) \\
& + \boldsymbol{\psi}(\mu_i,\phi_i+\pi;-\mu_i,\phi_i)\,\frac{\mu_i}{2\kappa_e}\,(1-\Upsilon^2)\Bigg]\frac{\mathbf{I}_0^i}{\mu_i}, \qquad (11.74)
\end{aligned}$$

where Υ is the one-way transmissivity of the middle layer, defined by Eq. (11.2).

The five terms of Eq. (11.74) are diagrammed in Fig. 11-13:

① The first term represents the transfer of the incident power through the middle layer down to the interface between layers 2 and 3, followed by specular reflection and propagation through layer 2 and beyond. This term does not contribute to the backscatter, except at normal incidence.

② The second term includes single volume backscatter downward by the middle layer and double specular reflection by the boundary at $z=-d$.

③ The third and fourth terms each includes single bistatic scattering by the middle layer and single reflection by the lower boundary.

④ The last term represents single volume backscatter upwards by the middle layer and no involvement of the lower boundary.

After deletion of the first term in Eq. (11.74) and comparison with Eq. (11.62), we obtain the transformation matrix

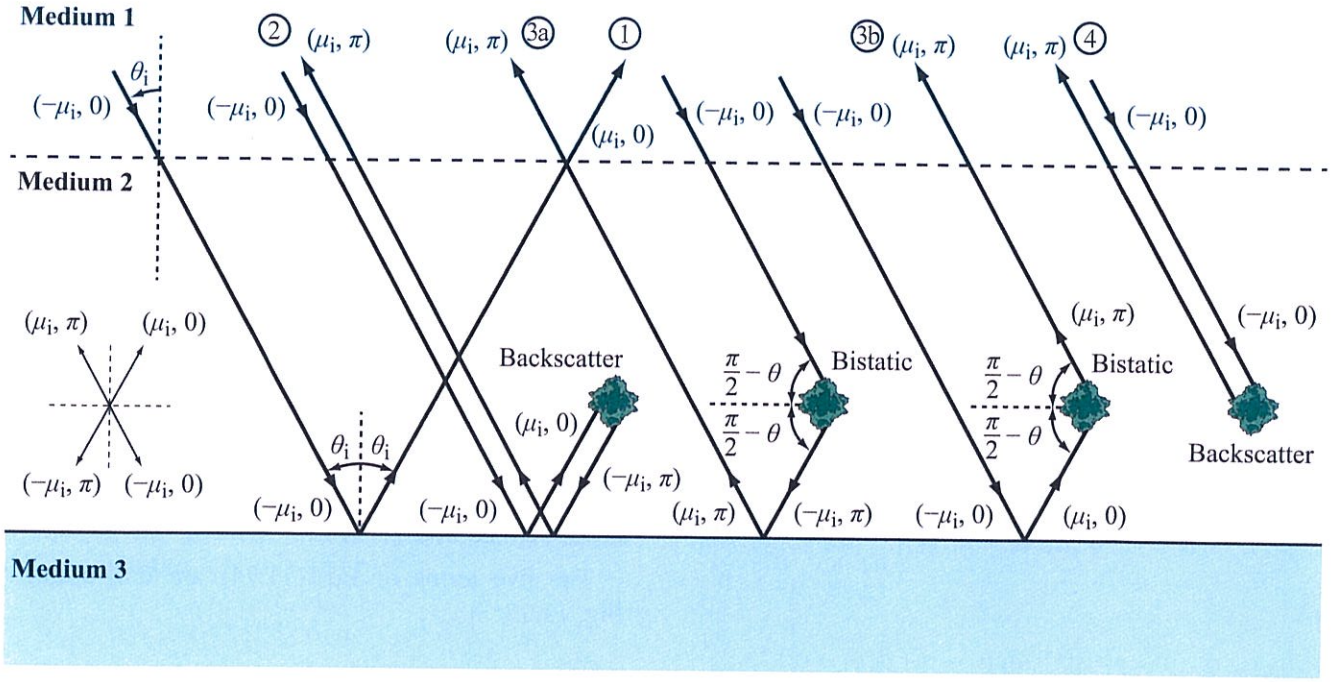

Figure 11-13: Volume scattering mechanisms.

$$\begin{aligned}\mathcal{T}_t(\mu_i, \phi_i + \pi; -\mu_i, \phi_i) = \\ \frac{(1-\Upsilon^2)}{2\kappa_e}\left[\boldsymbol{\psi}(\mu_i, \phi_i + \pi; -\mu_i, \phi_i)\right. \\ \left. + \Upsilon^2 \mathbb{R}(\theta_i)\, \boldsymbol{\psi}(-\mu_i, \phi_i + \pi; \mu_i, \phi_i)\, \mathbb{R}(\theta_i)\right] \\ + \frac{d\,\Upsilon^2}{\cos\theta_i}\left[\boldsymbol{\psi}(-\mu_i, \phi_i + \pi; -\mu_i, \phi_i)\, \mathbb{R}(\theta_i)\right. \\ \left. + \mathbb{R}(\theta_i)\boldsymbol{\psi}(\mu_i, \phi_i + \pi; \mu_i, \phi_i)\right]. \qquad (11.75)\end{aligned}$$

Because the lower boundary is assumed to be a perfectly flat surface, the radiative-transfer solution does not include the attenuated direct backscatter contribution of the lower surface, so it needs to be added. Hence, to synthesize the backscattering coefficient $\sigma^0_{rt}(\theta_i)$ for a specified receive/transmit polarization configuration, the expression for $\mathcal{T}_t$ should be used in Eq. (11.64).

11-6.5 Rayleigh Scatterers

If the middle layer is composed of Rayleigh particles and our interest is in vv polarization, we use Eq. (11.63a) with $[\mathcal{T}_t]_{11}$, which corresponds to Eq. (11.75) after replacing $\mathbb{R}$ with Γ_v and $\boldsymbol{\psi}$ with ψ_{11}. From Eq. (11.56), $\psi_{11} = 3\kappa_s/8\pi$ for all four combinations of incident and scattered directions contained in Eq. (11.75). Hence,

$$\begin{aligned}\sigma^0_{vv}(\theta_i) &= \Upsilon^2\, \sigma^0_{s_{vv}}(\theta_i) + 4\pi\cos\theta_i\, [\mathcal{T}_t]_{11} \\ &= \Upsilon^2\, \sigma^0_{s_{vv}}(\theta_i) + 4\pi\cos\theta_i\, \frac{(1-\Upsilon^2)}{2\kappa_e} \cdot \frac{3\kappa_s}{8\pi} \\ &\quad + 4\pi\cos\theta_i\, \Upsilon^2\Gamma^2\, \frac{(1-\Upsilon^2)}{2\kappa_e} \cdot \frac{3\kappa_s}{8\pi} \\ &\quad + 4\pi\cos\theta_i \cdot \frac{d\,\Upsilon^2}{\cos\theta_i}\left(2\Gamma^2 \cdot \frac{3\kappa_s}{8\pi}\right)\end{aligned}$$

$$= \Upsilon^2 \sigma^0_{s_{vv}}(\theta_i) + \frac{3}{4} a \cos\theta_i (1-\Upsilon^2)(1+\Gamma^2\Upsilon^2) + 3\kappa_s d \Gamma \Upsilon^2, \quad (11.76)$$

(incoherent addition)

where $\Gamma = \Gamma_v$ everywhere in Eq. (11.76). We refer to this expression as the ***single-scattering radiative transfer*** model with Rayleigh scatterers (S²RT/R) under the incoherent addition assumption.†

As was mentioned earlier in Section 11-1, the radiative transfer model adds all energy sources incoherently, without regard to phase interference, if present. The last term in Eq. (11.76) represents the incoherent addition of terms "3a" and "3b" in Fig. 11-13, which (for hh and vv polarizations) undergo the same phase delays due to propagation, the same phase changes due to specular reflection by the underlying ground surface, and probably the same phase changes introduced by bistatic scattering by the same differential volume. Hence, the two contributions should be in phase, in which case the magnitude of the last term in Eq. (11.76) should be increased by a factor of 2. Consequently,

$$\sigma^0_{vv}(\theta_i) = \Upsilon^2 \sigma^0_{s_{vv}}(\theta_i) + \frac{3}{4} a \cos\theta_i (1-\Upsilon^2)(1+\Gamma^2\Upsilon^2) + 6\kappa_s d \Gamma \Upsilon^2.$$

(coherent addition, vv-pol) (11.77)

We refer to this expression as the S²RT/R under the coherent addition assumption.

The single-scattering expression for σ^0_{vv} is identical with the expression given by Eq. (11.23) based on the heuristic model developed earlier in Section 11-1. It is extendable to hh polarization by replacing $\sigma^0_{s_{vv}}(\theta_i)$ with $\sigma^0_{s_{hh}}(\theta_i)$ and Γ^v with Γ^h. For hv polarization, Rayleigh particles do not generate cross polarization; hence none of the volume scattering terms contribute, in which case Eq. (11.77) simplifies to

$$\sigma^0_{hv}(\theta_i) = \Upsilon^2 \sigma^0_{s_{hv}}(\theta_i). \quad (11.78)$$

(hv polarization)

†Computer Code 11.1.

11-6.6 Distinct Upper Boundary

For a snow layer over ground or sea ice over water, we incorporate the presence of the distinct upper boundary by modifying the expression for σ^0 using the same steps outlined earlier in Section 11-3. Hence, for vv polarization

$$\sigma^0_{vv}(\theta_i) = \mathbb{T}^2_{12}(\theta_i) \left[\Upsilon^2 \sigma^0_{23}(\theta_i') + \frac{3}{4} a \cos\theta_i' (1-\Upsilon^2)(1+\Gamma^2_{23}(\theta_i')\Upsilon^2) + 6\kappa_s d \Gamma_{23}(\theta_i')\Upsilon^2 \right] + \sigma^0_{12}(\theta_i), \quad (11.79)$$

where $\mathbb{T}_{12}(\theta_i)$ is the v-polarized boundary transmissivity between media 1 and 2 (with medium 2 being the middle layer containing snow or sea ice), Υ is the one-way transmissivity of the middle layer along direction θ', $\sigma^0_{23}(\theta_i')$ is the vv-polarized backscattering coefficient of the lower boundary separating media 2 and 3, $\sigma^0_{12}(\theta_i)$ is the backscattering coefficient of the upper boundary separating media 1 and 2, and $\Gamma_{23}(\theta_i')$ is the v-polarized reflectivity of the lower boundary. A similar expression can be developed for hh polarization.†

11-7 Approximate Form of S²RT/R Model

In the absence of information about the roughness and moisture content of the lower boundary, it is difficult to assign lower and upper bounds on its backscattering coefficient σ^0_s. Imaging radar seldom operates at incidence angles below 20° or above 50°. Within this angular range, a careful review of experimental data and model predictions leads to the conclusion that for hh and vv polarizations σ^0_s of a random soil surface does not exceed 0 dB (or 1 m²/m²). The same upper limit applies to the overwhelming surface-roughness conditions associated with water surfaces. The lower bound, however, may be as low as −30 dB (or 10^{-3}

†Computer Code 11.2.

m^2/m^2) or lower for both land and water surfaces. Hence, we should keep this range in mind as we examine the volume scattering terms in Eq. (11.77) under various scenarios.

The last term in Eq. (11.77) includes the product $\kappa_s d$, which can be written as

$$\kappa_s d = \frac{\kappa_s}{\kappa_e}(\kappa_e d) = a\frac{\tau}{\sec\theta}, \tag{11.80}$$

where $a = \kappa_s/\kappa_e$ and, from Eq. (11.3), $\tau = \kappa_e d \sec\theta$. Also, from Eq. (11.2),

$$\Upsilon = e^{-\tau}, \qquad \text{or } \tau = -\ln\Upsilon. \tag{11.81}$$

Hence,

$$\kappa_s d = -a\cos\theta_i\,(\ln\Upsilon). \tag{11.82}$$

Let us consider Eq. (11.77) for pp polarization (with $p = $ v or h) for a vegetation canopy over a ground surface, and let us rewrite it in the form

$$\sigma^0_{pp}(\theta_i) = \sigma^0_g(\theta_i) + \sigma^0_c(\theta_i) + \sigma^0_{gcg}(\theta_i) + \sigma^0_{cg}(\theta_i), \tag{11.83}$$

where

$$\sigma^0_g(\theta_i) = \Upsilon^2\,\sigma^0_s(\theta_i) \tag{11.84a}$$

(ground contribution),

$$\sigma^0_c(\theta_i) = \frac{3}{4}a\cos\theta_i\,(1-\Upsilon^2) \tag{11.84b}$$

(direct canopy contribution),

$$\sigma^0_{gcg}(\theta_i) = \Gamma^2(\theta_i)\,\Upsilon^2\,\sigma^0_c(\theta_i) \tag{11.84c}$$

(ground-canopy-ground contribution),

$$\sigma^0_{cgt}(\theta_i) = -6a\cos\theta_i\,\Gamma(\theta_i)\,\Upsilon^2\,(\ln\Upsilon), \tag{11.84d}$$

(total ground-canopy contribution).

By applying the relationship given by Eq. (11.82), the three volume-related contributions (σ^0_c, σ^0_{gcg}, and σ^0_{cgt}) are now defined in terms of four quantities, namely: θ_i, $\Gamma(\theta_i)$, a, and Υ. Also, all three contributions are directly proportional to the albedo a. To gain some insight into the relative magnitudes of the three contributions, let us fix θ_i at 30° and evaluate the three contributions under six scenarios corresponding to three values of Υ (namely, 0.8, 0.5, and 0.1) and two soil moisture conditions (dry and wet). From Fig. 10-7:

$$\left.\begin{aligned}\Gamma^v &= 0.06\\ \Gamma^h &= 0.08\end{aligned}\right\} \text{ at } \theta = 30^\circ \text{ and } m_v = 0,$$

$$\left.\begin{aligned}\Gamma^v &= 0.36\\ \Gamma^h &= 0.46\end{aligned}\right\} \text{ at } \theta = 30^\circ \text{ and } m_v = 0.35 \text{ g/cm}^3.$$

Table 11-1 displays the magnitudes of the ratios $\sigma^0_{gcg}/\sigma^0_c$ and $\sigma^0_{cgt}/\sigma^0_c$ for the various aforementioned scenarios. Under all scenarios but one, σ^0_{gcg} is at least one order of magnitude smaller than σ^0_c. The one exception is when the soil is very wet and the canopy is only slightly lossy ($\Upsilon = 0.8$); for vv polarization, $\sigma^0_{gcg} = 0.135\sigma^0_c$, which may seem significant, but it is only 4% of the sum of σ^0_c and σ^0_{cgt}. Hence, the contribution σ^0_{gcg} may be ignored altogether, in which case Eq. (11.77) simplifies to

$$\sigma^0_{pp}(\theta_i) = \Upsilon^2\,\sigma^0_{s_{pp}}(\theta_i) + \frac{3}{4}a\cos\theta_i\left[(1-\Upsilon^2) - 8\Gamma^p(\theta_i)\,\Upsilon^2(\ln\Upsilon)\right]. \tag{11.85}$$

Note that because $0 \le \Upsilon \le 1$, it follows that $\ln(\Upsilon) \le 0$.

11-7.1 Applicability of the Single-Scattering Model

At this juncture, the reader may ask the following question: "How applicable is the single-scattering Rayleigh model to real media such as vegetation canopies, snow cover, and sea ice?" The simple answer is: The applicability of the Rayleigh model depends on the sizes of the scattering elements relative to λ, and on their orientations and the average spacing between them. However, even when the model is not applicable, its form often is used as a starting point for generating applicable semiempirical models.

The model derived in the previous subsections is predicated on several limiting assumptions, namely that:

Table 11-1: Ratios $\sigma^0_{gcg}/\sigma^0_c$ and $\sigma^0_{cgt}/\sigma^0_c$ computed for a Rayleigh layer at $\theta_i = 30°$ for hh and vv polarizations under dry and wet soil conditions for three values of the canopy one-way transmissivity Υ.

	$m_v = 0$ (dry)			$m_v = 0.35$ g/cm^3 (very wet)		
	$\Upsilon = 0.8$	0.5	0.1	$\Upsilon = 0.8$	0.5	0.1
$\sigma^0_{gcg}/\sigma^0_c$, hh-pol	4.1×10^{-3}	1.6×10^{-3}	6.4×10^{-5}	0.135	5.3×10^{-2}	2.1×10^{-3}
$\sigma^0_{gcg}/\sigma^0_c$, vv-pol	2.3×10^{-3}	9×10^{-4}	3.6×10^{-5}	8.3×10^{-2}	3.2×10^{-2}	1.3×10^{-3}
$\sigma^0_{cgt}/\sigma^0_c$, hh-pol	0.40	6.2×10^{-2}	1.5×10^{-2}	2.3	0.36	8.6×10^{-2}
$\sigma^0_{cgt}/\sigma^0_c$, vv-pol	0.30	4.7×10^{-2}	1.1×10^{-2}	1.7	0.28	6.6×10^{-2}

(a) the lower boundary is perfectly flat, thereby limiting the volume scattering contributions made by the middle layer to specific directions that simultaneously satisfy the specular reflection condition by the lower boundary and that the incidence and backscatter directions are exactly opposite of one another,

(b) the scattering constituents of the middle layer are sufficiently small in size relative to λ so as to satisfy the Rayleigh phase-function criterion,

(c) second- and higher-order scattering contributions are significantly smaller than first-order contributions and, therefore, may be ignored.

In the microwave region, the underlying surface is not electromagnetically smooth, and in the case of a vegetation canopy, the leaves and branches are comparable to or larger than λ in size. A flat leaf, for example, exhibits an elaborate scattering pattern similar to the radiation pattern of an antenna aperture of the same size and shape, as illustrated by the experimental measurements shown in Fig. 11-14. Furthermore, the scattering pattern changes if the leaf is not flat (Sarabandi et al., 1988). Wheat and corn stalks and tree branches are modeled as dielectric cylinders, which exhibit strong polarization-dependent scattering. In a tree canopy, the scattering elements have size, shape and orientation distributions, all of which may vary as a function of height between the ground surface and the top of the canopy.

To address these physical attributes of the scattering medium, several theoretically sophisticated and computationally demanding models were developed and used to compare their predictions with experimental observations (Ulaby et al., 1990b; Sun and Ranson, 1995; Lin and Sarabandi, 1999a,b; Marliani et al., 2002). Because in most cases the various size, shape, and orientation distributions are either unknown or only rudimentary estimates of them are available, numerous assumptions and parameter adjustments are made in

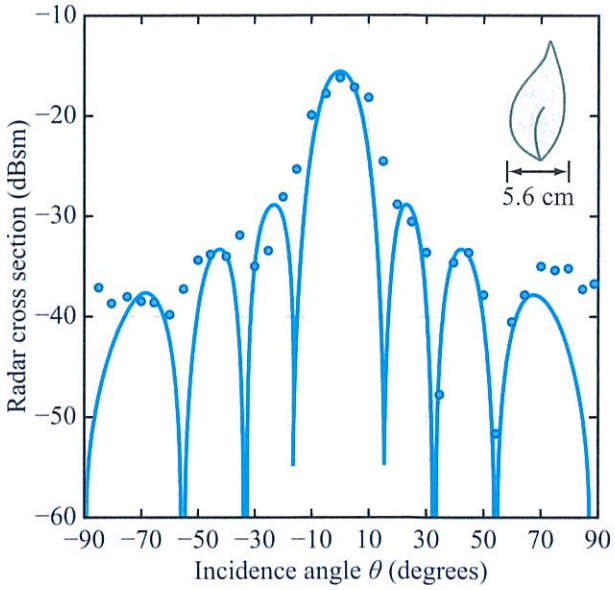

Figure 11-14: Radar scattering pattern of a leaf as a function of illumination angle relative to normal incidence [Senior et al., 1987].

computational models so as to arrive at good agreement with experimental observations. The other problem with many-parameter models is that they are rather difficult to invert.

Even though the scattering pattern of an individual leaf or branch in a canopy is strongly dependent on the direction and polarization of the illumination incident upon it, the scattering pattern of an ensemble of such leaves and branches of various sizes, shapes, and orientations is not. The randomness "destroys" most of the sensitivity to these physical parameters. Consequently, the simple single-scattering Rayleigh model often is a viable contender in many volume scattering situations of interest. One of its attracting features is that it consists of only three parameters, the extinction coefficient κ_e, the albedo a, and the depth of the layer d. These, in addition to the roughness and dielectric properties of the underlying surface, are sufficient to compute σ^0_{vv} and σ^0_{hh} of a vegetation canopy. The average dielectric constant of the canopy layer may be assumed to be ≈ 1. For a snow or ice layer, the average dielectric constant may depart significantly from 1, in which case it needs to be added to the total list of parameters. We should also note that even though one of its implicit assumptions is that the scattering layer is a weakly scattering medium (small albedo a), the model is often applied with no restriction on the value of a (between 0 and 1).

For the most part, the single-scattering Rayleigh model provides good agreement with experimental observations for many scene conditions, but only for hh and vv polarizations: the only contributions to σ^0_{hv} are due to scattering by the lower and upper surfaces. This implies that for a high-loss vegetation canopy, $\sigma^0_{hv} = 0$, which certainly is not the case.

11-7.2 Comparison with Experimental Observations

Using the combination of the I^{2}EM model to compute surface scattering and the S^{2}RT/R (single-scattering radiative transfer model with Rayleigh particles) to compute volume scattering, model parameters were selected to fit the model to experimental data for vegetation over soil, snow over soil, and sea ice over ocean water. Examples are displayed in Figs. 11-15 to 11-17.

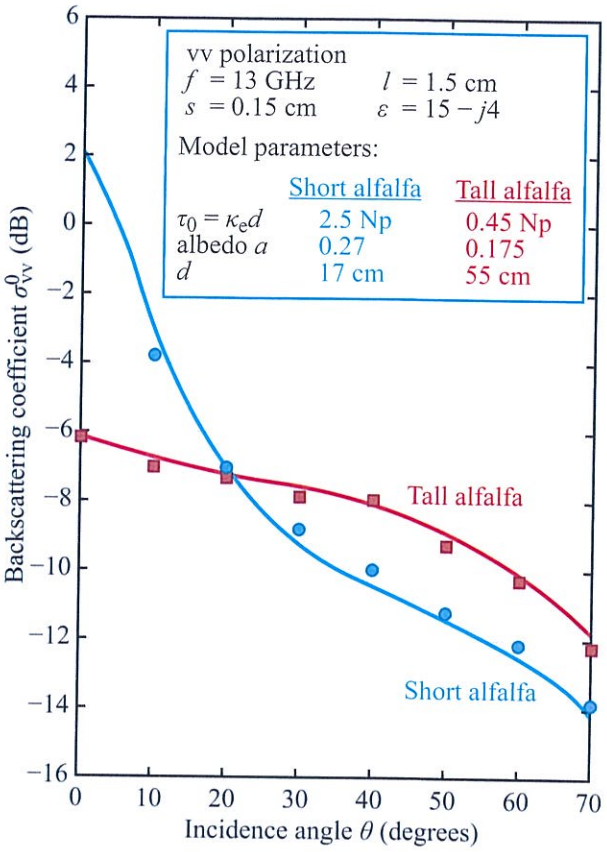

Figure 11-15: Fitting the S^{2}RT/R model to backscattering data measured for a short alfalfa canopy and a tall alfalfa canopy.

The alfalfa measurements include two canopies, a 17 cm tall canopy with a zenith optical thickness $\tau = 0.45$ Np, and a 55 cm tall canopy with $\tau = 2.5$ Np. The second canopy is not only three times taller, but the vegetation density also is greater. As expected, the backscatter response of the short canopy is dominated by the soil-surface contribution, particularly at incidence angles below 40°. In contrast, the gentle angular response of the tall canopy suggests that the canopy masks the soil contribution and the backscatter is dominated by the direct canopy term σ^0_c.

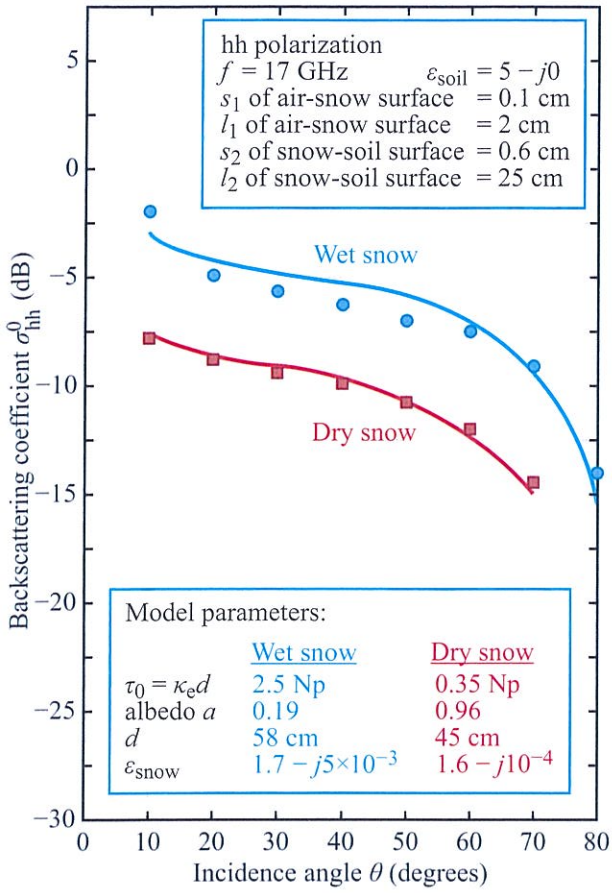

Figure 11-16: Fitting the S²RT/R model to dry and wet snow data measured at 17 GHz.

Dry snow is modeled as low-loss ice crystals in a background of air. At 17 GHz, scattering by the ice crystals dominates over absorption. Consequently, the model parameters chosen for matching the measured data in Fig. 11-16(a) to the model include an albedo $a = 0.96$ and $\tau = 0.35$ Np. In contrast, the data measured for wet snow [Fig. 11-16(b)] required values of $a = 0.19$ and $\tau = 2.5$ Np because wet snow is a lossy medium.

The 10 GHz data shown in Fig. 11-17 for sea ice was reported by Onstott (1990). The model parameters include $a = 0.4$ and $\tau = 0.75$ Np. As a volume scattering medium, the ice layer is intermediate between those of dry and wet snow.

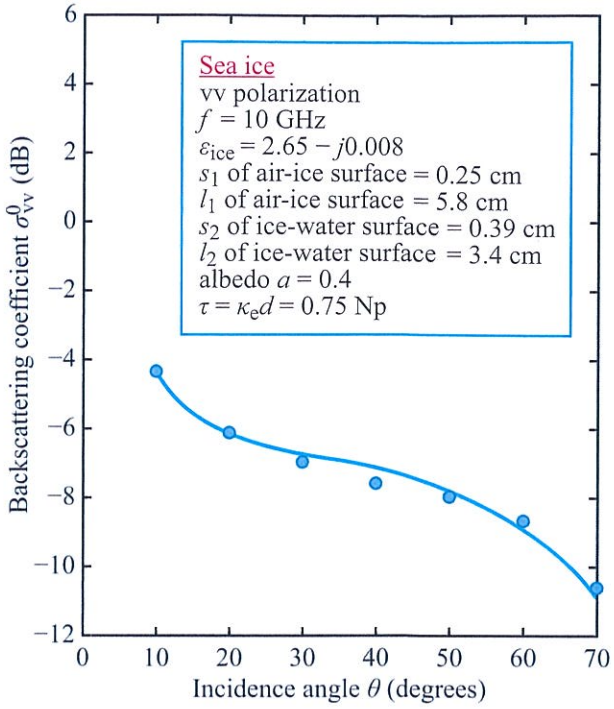

Figure 11-17: Fitting S²RT/R model to sea-ice data at 10 GHz. Data reported by Onstott (1990).

11-8 Radar Observations of Vegetation Canopies

The purpose of this section is to provide an overview, based on models and experimental observations, of how the backscattering coefficient responds to the various physical parameters of a vegetation canopy. Before we embark on such an overview we summarize our understanding of the penetration and propagation properties of vegetation canopies and the soil surface underneath them.

11-8.1 Penetration Depth in Soil

For perfectly dry soil, $2 \lesssim \varepsilon'_{soil} \lesssim 4$ and $\varepsilon''_{soil} < 0.05$. The exact values of ε'_{soil} and ε''_{soil} depend on the soil density and composition. For $\varepsilon'_{soil} = 3$ and $\varepsilon''_{soil} = 0.05$, the penetration depth at 1 GHz is $\delta_p = 1.65$ m. This

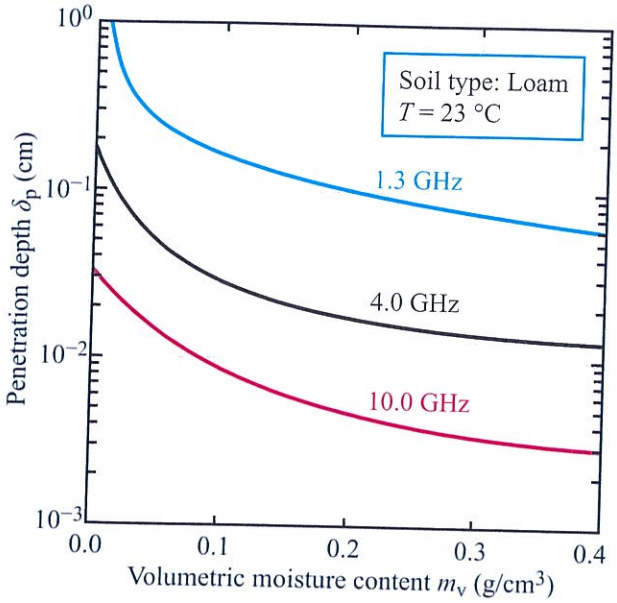

Figure 11-18: Penetration depth in loamy soil as a function of volumetric moisture content.

means that for dry desert sand, signal penetration of a few meters is quite feasible at 1 GHz, which explains why the L-band Shuttle Imaging Radar-A (SIR-A) was capable of detecting and mapping subsurface topography in the Egyptian desert (Schaber et al., 1986).

Increasing the soil volumetric moisture content m_v leads to an exponential-like decrease in the magnitude of δ_p, as shown in Fig. 11-18.

11-8.2 Propagation Properties of Cultural Vegetation

A wheat canopy may be divided into three constituents: (1) leaves, (2) stalks, and (3) heads. For modeling the radiation transfer both within and through the canopy, it may be divided into an upper layer comprising the heads and a lower layer comprising the leaves and stalks. For another crop, such as corn, the canopy may be approximated as an upper layer consisting primarily of leaves and a lower layer consisting of stalks. Similarly, other configurations may be appropriate for other crop types. In modeling or interpreting the emission and scattering from a crop canopy, it is useful to know the propagation characteristics of the canopy as a whole, as well as those of its constituent parts.

The propagation properties of a vegetation canopy may be computed using either a deterministic approach or a statistical one. The ***deterministic approach*** requires that the absorption and scattering cross sections be known for each leaf, stalk, branch, etc., in the canopy and that their locations and orientations and the degree of interaction between them also be known. Clearly, such a problem is rather difficult to solve when the canopy constituents are comparable to or larger than λ in size. Moreover, the size, orientation, shape, and location information usually is not available. Furthermore, a vegetation canopy exhibits some degree of randomness, which means that the canopy architecture contained in a given radar resolution cell is statistically different from those in other resolution cells.

In contrast, the ***statistical approach*** usually (1) assumes that the canopy constituents (leaves, etc.) are randomly distributed in space, either within the canopy as a whole or within a subregion of the canopy (such as in the upper part of the canopy if its plants do not grow leaves in the lower part), (2) ignores interactions between canopy constituents, and (3) uses statistical distribution functions to describe the shapes, sizes, and orientations of the canopy constituents. If these parameters vary with height between the ground surface and the top of the canopy, the canopy is modeled as a series of horizontal layers each with its own statistical distributions.

For an elemental canopy volume—defined such that it is small enough so that the density, type, etc., of canopy constituents is approximately uniform across it and yet large enough to contain a representative sample of constituents, its extinction coefficient κ_e may, in general, be a function of height z above the ground, incidence angle θ, wave polarization p, and azimuth angle ϕ if the canopy architecture is not azimuthally symmetrical. Thus,

$$\kappa_e = \kappa_e(\theta, \phi, z, p).$$

The corresponding ***attenuation*** (***optical thickness***) of a canopy of height h is

$$\tau = \int_0^h \kappa_e z \sec\theta. \qquad (11.86)$$

Computing κ_e for an elemental canopy volume requires knowledge of all of the shape, size, and orientation distributions for each type of canopy constituent, as well as scattering and absorption models for each type of constituent. Stalks and branches usually are modeled as dielectric cylinders, leaves are modeled as dielectric plates, and so on. Because these scattering elements are comparable to λ in size, the scattering models tend to be mathematically complex and computationally demanding. Examples of such models are available in Ulaby and Elachi (1990) and Ulaby et al. (1990b).

The propagation properties of a vegetation canopy can be measured experimentally by transmitting a signal through the canopy. The sketch shown in Fig. 11-19(a) illustrates the setup used by Allen and Ulaby (1984) to measure the optical thickness of a wheat canopy. The transmitting antenna was situated above the canopy, and its boresight direction was at an angle of incidence of 60° and an azimuth angle of 90° relative to the row direction of the crop. The receiving antenna was mounted on a motor-drive platform that could be moved vertically from 23 cm to 132 cm above the soil surface. The total canopy height was 105 cm, of which the heads comprised about 8 cm. The receiving antenna was connected to a detector, which in turn was connected to a power meter. The height of the receiving antenna was converted to a voltage through a potentiometer and was used to drive the x axis of an x-y plotter with the y axis denoting the strength of the received power. After measuring the received power as a function of receiving-antenna height, the system was calibrated by repeating the measurements with no canopy present between the antennas. The net result was a curve of the type shown in Fig. 11-19(b), which displays the measured cumulative attenuation (optical thickness) of the canopy as a function of the path length s as defined in the inset. The average slope of the curve, which is about 4.6 Np/m, represents the slant extinction coefficient of the wheat stalks at $\theta = 60°$ for vertical polarization. Repetition of

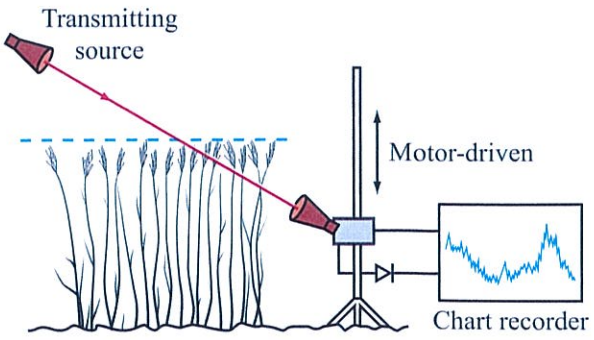

(a) Sketch showing measurement setup

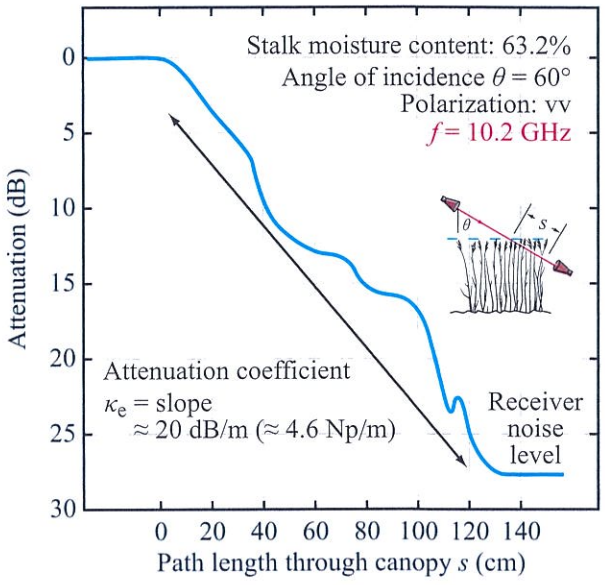

(b) Stalk attenuation

Figure 11-19: Sketch showing the setup used by Allen and Ulaby (1984) to measure canopy attenuation as a function of depth. The receiving antenna was a 5 cm diameter horn.

this type of experiment at five additional locations within the wheat field resulted in an average overall extinction coefficient of 6.91 Np/m (or 30 dB/m) and an associated standard deviation of 2.8 Np/m.

Most attempts to measure the extinction coefficient of vegetation canopies have relied on either (a) measuring

the power transmitted through the canopy as detected by a receiver placed beneath the canopy, or (b) measuring the power reflected from a standard target (such as a trihedral reflector) placed beneath the canopy. In both cases, the attenuation is computed by comparing the power intensity with and without the canopy. The transmission approach measures the one-way total attenuation of the canopy, whereas the reflection approach measures the two-way attenuation.

When using the one-way transmission method, placement of the receiving antenna in close proximity of the vegetation may cause near-field interactions that may distort the gain and pattern of the antenna, thereby leading to inaccurate estimates of attenuation. Similar effects can occur in the two-way transmission method; the scattering pattern of the standard target can be distorted by the close presence of the vegetation. Another source of measurement uncertainty is the spatial inhomogeneity of the vegetation canopy; large fluctuations (due to location) are observed among measurements made through different transects.

Both sources of uncertainty can be reduced through spatial averaging. In the configuration depicted in Fig. 11-20, the receiving antenna and detector are placed on plastic rails close to the ground surface. The antenna assembly is tied to a rope and synchronized with the position of the radar on the truck by means of pulleys. As the track moved alongside the field, the assembly moved as well. Using this technique, a long record of the power transmitted through the canopy can be measured, from which an average value with a small standard deviation can be computed. Based on measurements performed for corn and wheat canopies at 10.2 GHz, Ulaby and Jedlicka (1984) determined that the standard deviation associated with the average value of the total attenuation is on the order of 1 dB (or equivalently, 0.23 Np). Figures 11-21(a) and (b) show the temporal variation of canopy attenuation τ (in dB) over the full growing season for canopies of soybeans and corn. The measurements were made at 10.2 GHz using v-polarized transmit and receive antennas. The incidence angle is 52° and the propagation direction is orthogonal to the row direction.

In both cases, the measured total attenuation τ is small during both the early and final stages of plant growth and is a maximum during the period that begins after the plants have attained their full height and ends when the plants begin to lose their moisture.

Also shown in Figs. 11-21(a) and (b) are plots based on relatively simple models. For soybeans, the model relates the total attenuation τ (in Np) to the canopy height and ***volume fractions*** occupied by leaves and stalks, v_ℓ and v_{st}, as follows:

$$\tau = \tau_\ell + \tau_{st} = (\kappa_\ell + \kappa_{st}) h \sec\theta, \tag{11.87}$$

where κ_ℓ *and* κ_{st} *account for absorption by leaves and stalks* by treating the canopy as a superposition of two canopies (Fig. 11-22), one composed of leaves and has a ***leaf canopy effective index of refraction*** $n_{c,\ell}$, and another composed of stalks and has a ***stalk canopy effective index of refraction*** $n_{c,st}$. The canopy leaf and stalk indices of refraction are related to the ***indices of refraction of the leaf and stalk material***, n_ℓ and n_{st}, via the refractive model given by Eq. (4.45) with $\alpha = 1/2$. That is,

$$n_{c,\ell} = (1 - v_\ell) n_{air} + v_\ell n_\ell, \tag{11.88a}$$

$$n_{c,st} = (1 - v_{st}) n_{air} + v_{st} n_{st}, \tag{11.88b}$$

where $n_{air} = 1$, and v_ℓ and v_{st} are the volume fractions of leaves and stalks contained in the canopy. Both v_ℓ and v_{st} vary as a function of time, but throughout the growth cycle their magnitudes are on the order of 0.01. Hence, Eqs. (11.88a) and (11.88b) yield values for $n'_{c,\ell}$ and $n'_{c,st}$ that are only slightly larger than that of the air background, namely $n_{air} = 1$. Hence, the equations simplify to

$$n''_{c,\ell} \approx v_\ell n''_\ell, \tag{11.89a}$$

$$n''_{c,st} \approx v_{st} n''_{st}. \tag{11.89b}$$

Finally, the extinction coefficients are related to the canopy leaf and stalk indices of refraction by

$$\kappa_e = \frac{2\pi}{\lambda_0} (n''_{c,\ell} + n''_{c,st}) = \frac{2\pi}{\lambda_0} (v_\ell n''_\ell + v_{st} n''_{st}). \tag{11.90}$$

For each date on which direct transmission measurements were made, Ulaby and Jedlicka (1984) measured

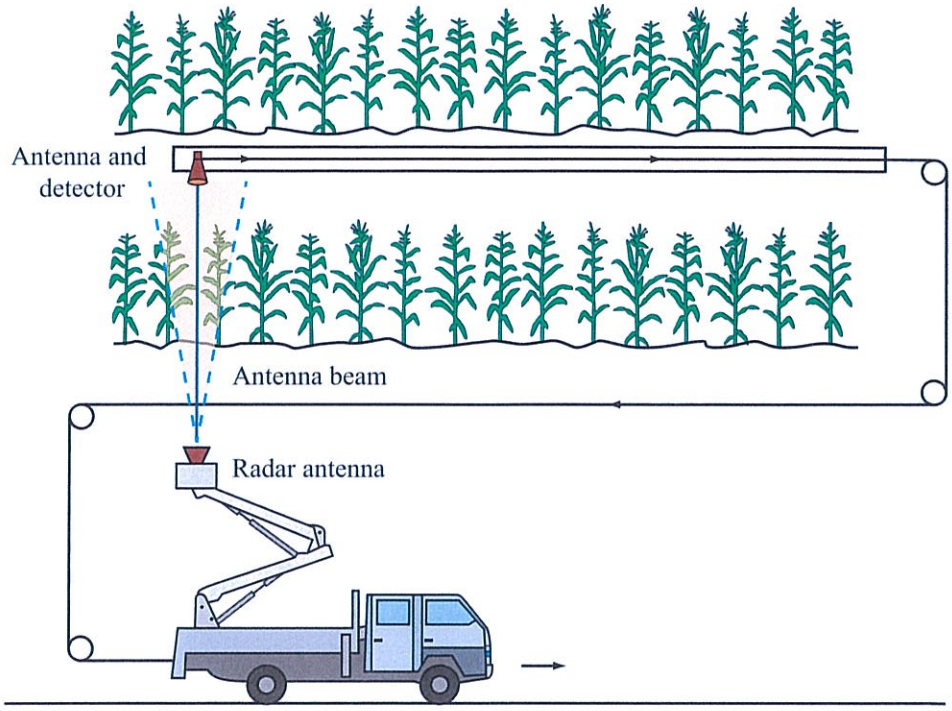

Figure 11-20: Attenuation measurement setup [Ulaby and Jedlicka, 1984].

v_ℓ and v_{st} of the canopy by removing plants from a representative section of the canopy and estimating their leaf and stalk volume fractions, and they also used a dielectric measurement technique to determine the value of ε_ℓ and ε_{st} (and hence $n_\ell = \sqrt{\varepsilon_\ell}$ and $n_{st} = \sqrt{\varepsilon_{st}}$). Good agreement is observed between the measured and model-calculated values shown in Fig. 11-21(a), despite the fact that (a) the model completely ignored scattering by the leaves and stalks and (b) treated the canopy constituents as if they are very small relative to λ, which they are not.

A similar attempt was made for a corn canopy, but the simple model did not provide good agreement with the measured values of τ. The curve labeled "calculated attenuation" in Fig. 11-21(b), which accounts for absorption by only the leaves of the corn plants, underestimates the value of τ. Including absorption by the stalks, as was done previously for the soybeans canopy, leads to overestimation of the value of τ. The apparent inapplicability of the model to the corn canopy is attributed to the fact that the corn stalks have an ordered spacing and orientation, whereas the refractive model assumes the inclusions to be not only small in size, but also randomly oriented within the mixture volume.

11-8.3 Extinction by a Canopy Containing Stalks

To model the propagation properties of a canopy with vertical stalks, Ulaby et al. (1987) developed a canopy model in which the stalks are represented by vertically oriented, lossy dielectric cylinders and the leaves are treated as randomly oriented discs. The model computes absorption and scattering by the cylinders, as well as absorption by the leaves. To evaluate the validity of the model, they also measured the transmission loss for a mature corn canopy at incidence angles of 20°,

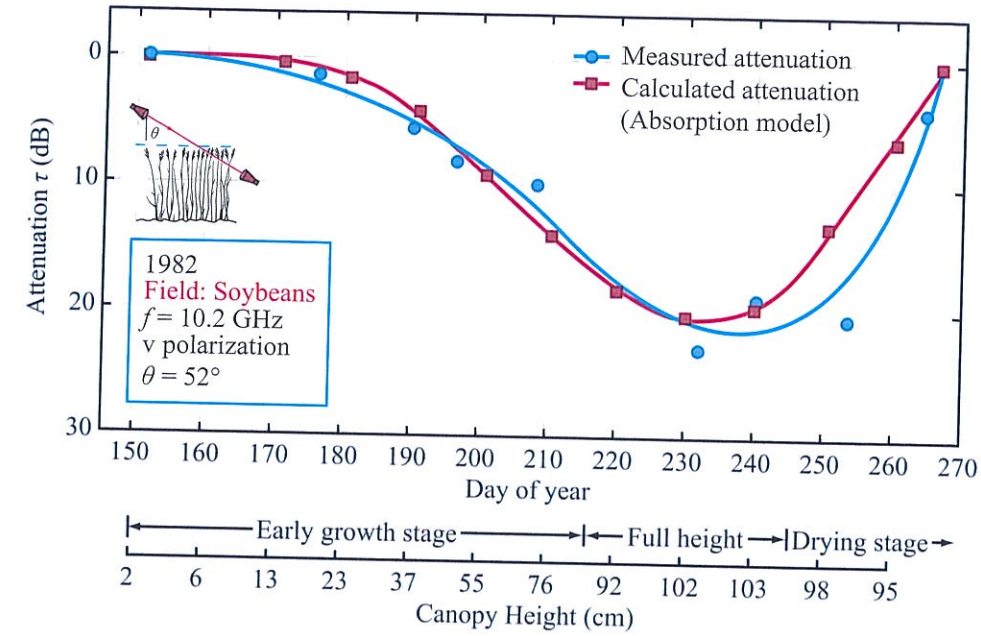

(a) Soybeans

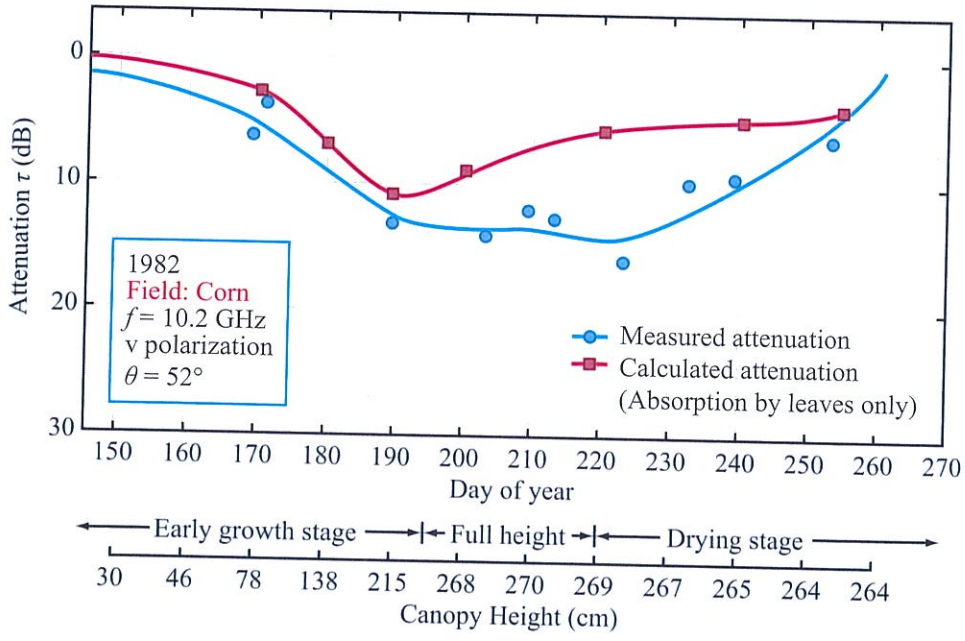

(b) Corn

Figure 11-21: Measured and calculated one-way attenuation of soybean and corn canopies at 10.2 GHz [Ulaby and Jedlicka, 1984].

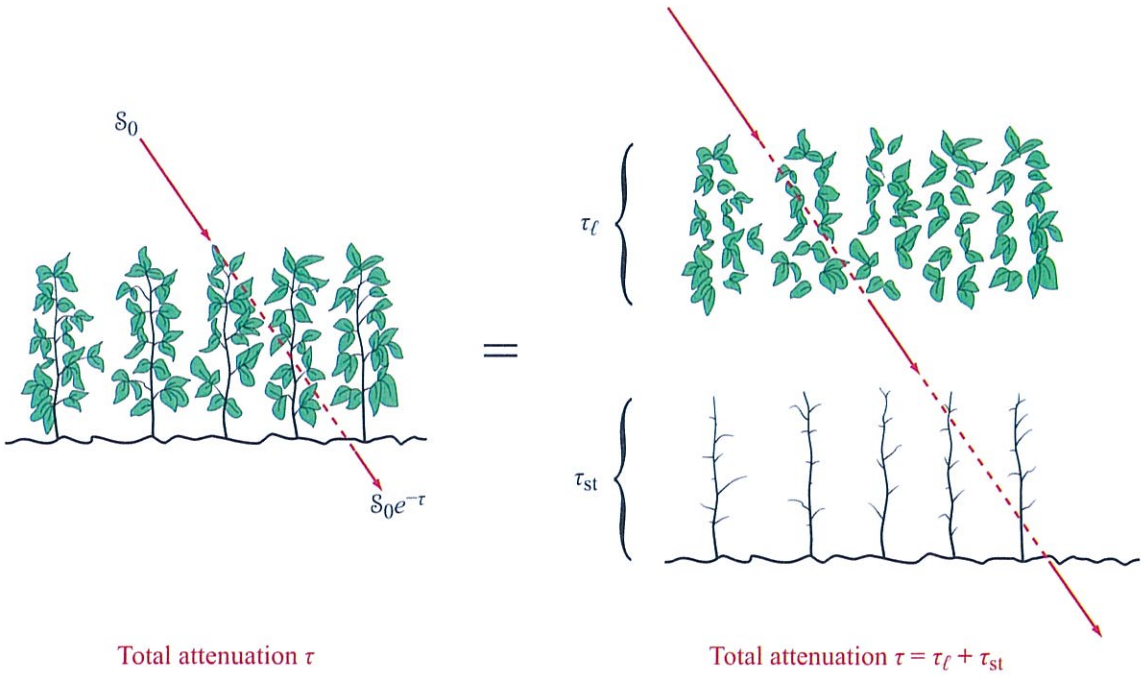

Figure 11-22: A vegetation canopy consisting of leaves and stalks is modeled as the sum of two equivalent canopies, one containing leaves only and another containing the stalks.

40°, 60°, and 90° using the configurations depicted in Fig. 11-23. The transmitters and receivers used dual-polarized antennas with center frequencies at 1.62, 4.75, and 10.2 GHz.

Using the vegetation dielectric model given in Section 4-9.2 and the volumetric moisture content measured for samples of leaves and stalks, it was possible to compute the dielectric spectra displayed in Fig. 11-24 and to use them to compute the extinction cross section for a single stalk, and by extension, the extinction coefficient of the canopy. The stalks, which were about 2.7 m tall, varied in diameter from 2.8 cm at the base to 0.6 cm at the top. In the model, the stalks were assumed to have a uniform diameter of 1.7 cm. Figure 11-25 displays the spectra for the absorption, scattering, and extinction "widths," normalized to the cylinder diameter d, when illuminated along a direction normal to the cylinder axis. Note the strong sensitivity to the polarization direction, particularly at frequencies below 3 GHz. Scattering and absorption by a dielectric cylinder are strongly dependent on the diameter d relative to λ in the cylinder. For the specified value of the stalk dielectric constant given in Fig. 11-25, the wavelength λ at 1 GHz is approximately 30 cm/4.2 $\approx$ 7.1 cm. Hence, $d/\lambda \approx 1.7/7.1 \approx 0.24$. As f is increased to 10 GHz, d/λ increases to 2.4. When the cylinder diameter becomes very large relative to λ, scattering and absorption become insensitive to the direction of the polarization vector.

By extending the model from a single dielectric cylinder to a medium of parallel cylinders illuminated at any incidence angle θ_i, it was possible to compute the extinction coefficient κ_e of the corn canopy and to compare the model predictions with experimental measurements. An example is shown in Fig. 11-26(a) for transmission at 1.62 GHz. For an h-polarized wave, κ_e is less than 0.2 dB/m at all incidence angles, rendering the canopy almost transparent. In contrast, the extinction

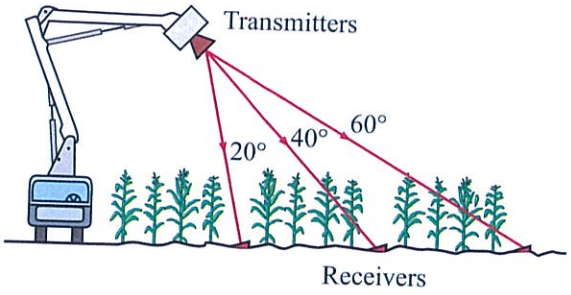

(a)

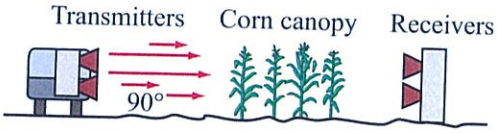

(b)

Figure 11-23: Configurations used for transmission measurements at (a) 20°, 40°, 60°, and (b) 90° [Ulaby et al., 1987].

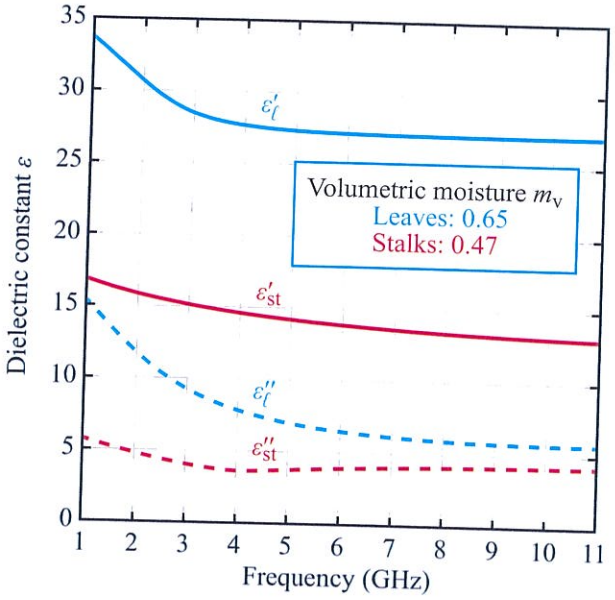

Figure 11-24: Dielectric constant of corn leaves and stalks as a function of frequency [Ulaby et al., 1987].

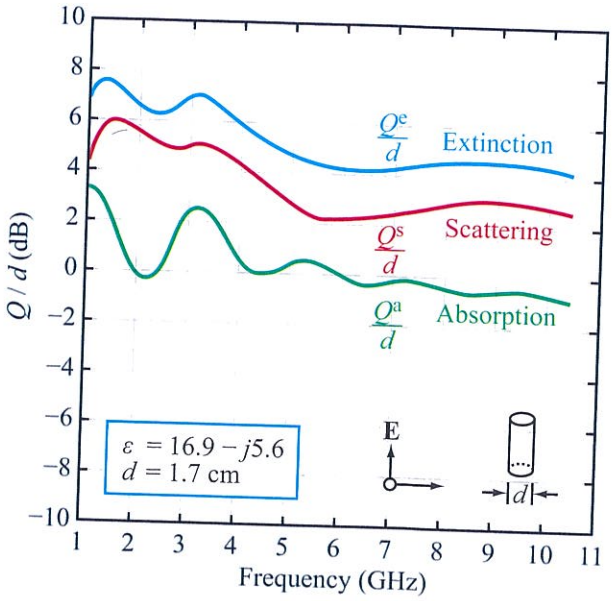

(a) v-polarization

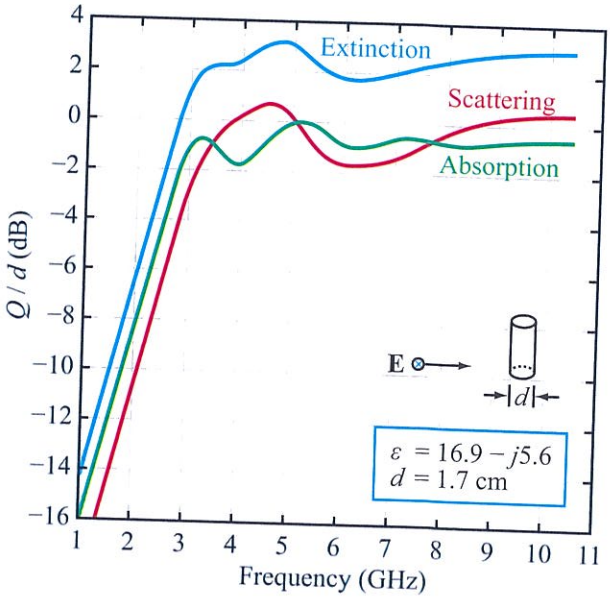

(b) h-polarization

Figure 11-25: Calculated spectral variation of the normalized absorption, scattering, and extinction widths for an infinite cylinder illuminated with (a) a v-polarized wave and (b) an h-polarized wave [Ulaby et al., 1987].

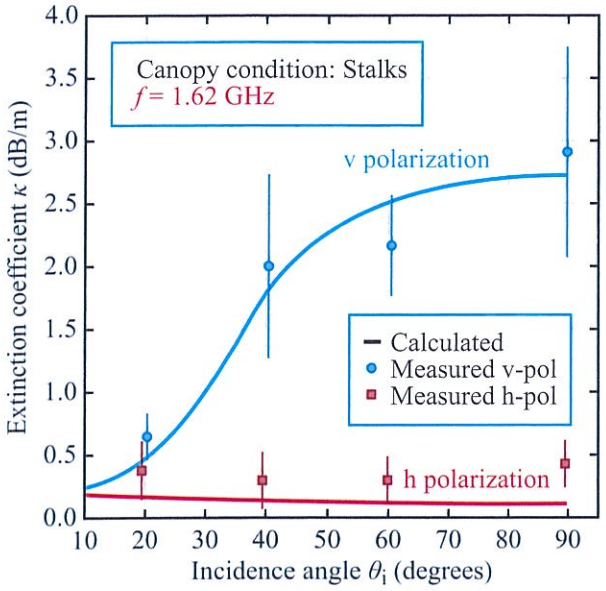

(a) 1.62 GHz

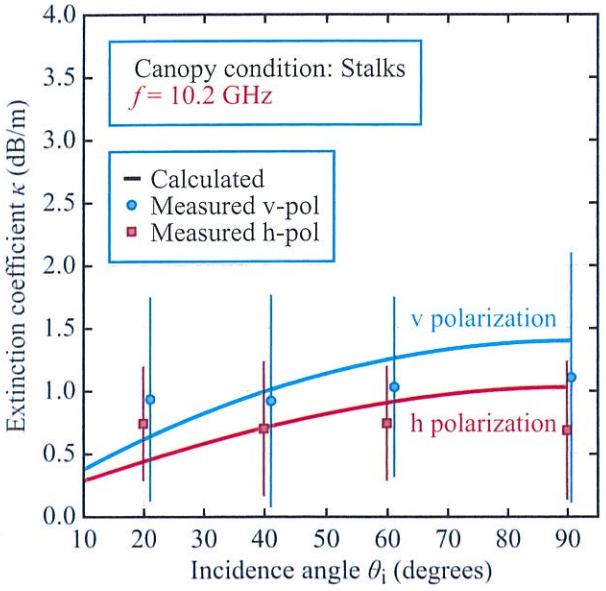

(b) 10.2 GHz

Figure 11-26: Comparison of calculated extinction coefficient for stalks with measured values at (a) 1.6 GHz and (b) 10.2 GHz.

coefficient of a v-polarized wave is strongly dependent on θ_i, increasing from about 0.2 dB at near normal incidence to as high as 2.5 dB/m at grazing incidence ($\theta_i = 90°$).

For a homogeneous medium with a complex index of refraction $n = n' - jn''$, the attenuation coefficient is given by

$$\alpha = \frac{2\pi}{c} f n'', \tag{11.91}$$

where c is the velocity of light. Hence, if n does not vary with the frequency f, α should increase linearly with f. Whereas this is true for a homogeneous medium, as well as approximately so for a medium containing dielectric particles that are sufficiently smaller than λ (thereby representing the medium in terms of an equivalent dielectric medium along the lines outlined in Section 4-4), the stated frequency dependence of α is not always valid. Comparison of the results shown in Fig. 11-26(b) for $f = 10.2$ GHz with those shown in Fig. 11-26(a) for $f = 1.62$ GHz demonstrates that the extinction coefficient for h polarization is indeed larger at the higher frequency, but the reverse is true for v polarization.

11-8.4 Role of Soil Surface Contribution

The volumetric moisture content of a green leaf is typically in the 70% range, in contrast to that of a yellow leaf at the end of the growing season, which may be as low as 10%. According to the leaf dielectric model in Section 4-9, the dielectric constant ε_v is strongly dependent on the leaf's gravimetric moisture content m_g. At 10 GHz, for example, $\varepsilon_v \approx 20 - j8$ for $m_g = 0.7$, compared with $\varepsilon_v \approx 1.9 - j0.2$ for $m_g = 0.1$. Correspondingly, the extinction coefficient is much smaller for the dry vegetation than for the green vegetation. Hence, when a radar was used to measure the angular response of a wheat field at 9 GHz immediately before and after harvesting the wheat plants, no statistically discernible change was observed. The measured plots of σ^0 are shown in Fig. 11-27. A relatively dry canopy of wheat is essentially "transparent" to microwaves at all angles of incidence up to at least 60°.

Figure 11-28 shows the results obtained from a

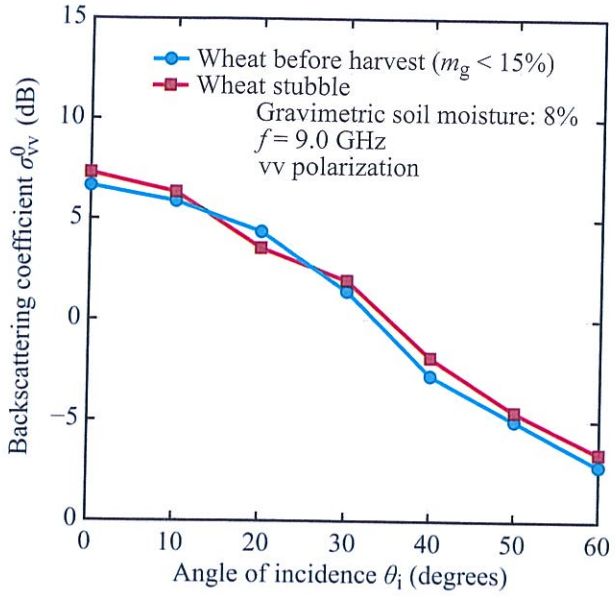

Figure 11-27: A canopy of dry wheat plants is "transparent" to microwaves; no discernible change in σ^0 is observed following the cutting and removal of the wheat plants [from Lopes, 1983].

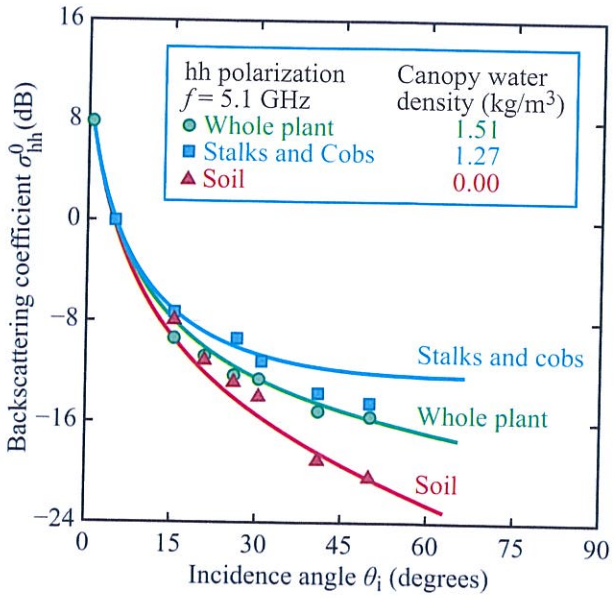

Figure 11-28: Measured σ^0 of a fully mature corn canopy in three consecutive stages of defoliation; all measurements were made on the same day.

defoliation experiment conducted on a corn canopy. A 5.1 GHz scatterometer was used to measure $\sigma^0_{hh}(\theta)$ for:

(a) a mature corn canopy under natural conditions,

(b) the same canopy after removing its leaves, but keeping the stalks and cobs in place, and

(c) the bare soil remaining after removal of stalks and cobs.

Based on the data displayed in Fig. 11-28, we deduce the following conclusions:

(1) At incidence angles $\theta_i \lesssim 20°$, the total canopy backscattering coefficient is dominated by the soil surface contribution.

(2) As θ_i increases beyond 30°, the plant becomes the dominant contributor to the total σ^0 of the canopy.

(3) For $\theta_i \gtrsim 30°$, the level of the curve labeled "stalks and cobs only" is higher than that corresponding to that labeled "whole plant." This implies that the backscattering contribution of the corn stalks and cobs is very significant, but that the attenuation by the leaves present in the upper part of the canopy reduces the stalk contribution to a level comparable to or smaller than the backscattering contribution by the leaves.

These observations suggest that a uniform canopy model in which all of its constituents (leaves, stalks, and cobs) are treated as if they have the same extinction and scattering properties, is not applicable in this case. The constituents should not be modeled as isotropic or Rayleigh particles because their dimensions are comparable to or longer than λ, and their orientations are certainly not randomly distributed.

To illustrate the relative importance of the soil contribution, we show in Fig. 11-29 pairs of angular plots for four vegetation canopies, all observed at 4.25 GHz. For each crop, the experimental observations were made under almost identical canopy conditions, but under very different soil-moisture conditions. Note that the observation dates between the dry-soil and wet-

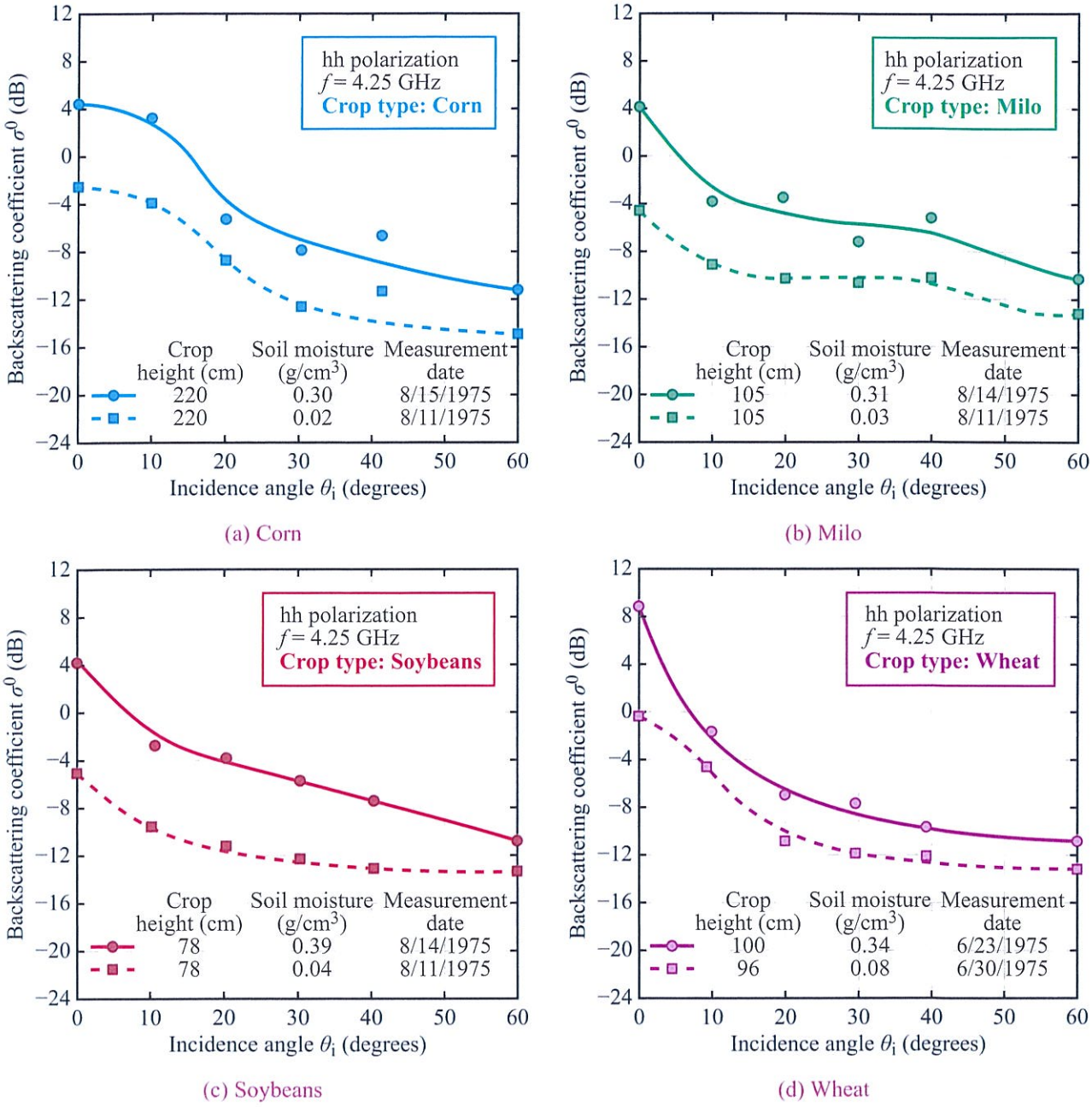

Figure 11-29: Angular response of scattering coefficient for wet and dry soil conditions at 4.25 GHz for (a) corn, (b) milo, (c) soybeans, and (d) wheat.

soil conditions are only a few days apart. The dates corresponding to the wet-soil conditions are only one day after a heavy rain that soaked the soil surface and increased its volumetric moisture content from $m_v \approx 0.04$ g/m^3 to $m_v \approx 0.35$ g/m^3.

Because the canopies were essentially unchanged between the two observation conditions, we attribute the difference in level between the two curves entirely to the underlying soil surface. In general, the wet-soil σ^0 is higher than the dry-soil σ^0 by about 7–8 dB at nadir, decreasing to about 3–4 dB at 60°.

11-8.5 σ^0 Relationship to Leaf-Area Index

Consider the plots displayed in Fig. 11-30. The left-hand vertical scale pertains to σ^0 of a corn canopy, plotted as a function of time over the growing season (approximately 100 days). The units of σ^0 are m^2/m^2 (rather than dB). The right-hand scale pertains to the temporal variation of the canopy's green ***leaf-area index*** (LAI), defined as the total single-sided surface area of all leaves contained in the canopy over a unit ground area. For the corn canopy of Fig. 11-30, the LAI $L(t)$ increases from zero at planting to a maximum of about 3.5 when the plants reach full maturity (known as Hanway stage 5), and then slowly decreases back to zero by the end of the growth cycle. Note the general similarity between the shapes of the temporal plots of $\sigma^0(t)$ and $L(t)$. Similar patterns also were observed for sorghum and wheat canopies.

To some extent, the leaf-area index is a surrogate for the amount of water contained in the canopy constituents, which is the single most important parameter influencing the attenuation by and scattering from vegetation. Also, even though the leaf-area index pertains to green leaves only, its temporal variation is correlated with the temporal variation of the amount of water contained in the stocks. With the understanding that the leaf area index $L(t)$ serves as an approximate representative of the canopy mass, Ulaby et al. (1984) used the form of the single-scattering model of Section 11-1 to develop a semiempirical model of the form

$$\sigma^0 = A_1 L^n (1 - e^{-bL}) + A_2 e^{-bL}, \qquad (11.92)$$

where A_1, A_2, and b are empirically determined constants, and $n = 0$ for corn and sorghum and 1 for wheat. The model parameters were determined using only the radar observations at times t such that $L \geq 0.2$. The results, displayed in Fig. 11-31, confirm the general applicability of the relatively simple semiempirical model.

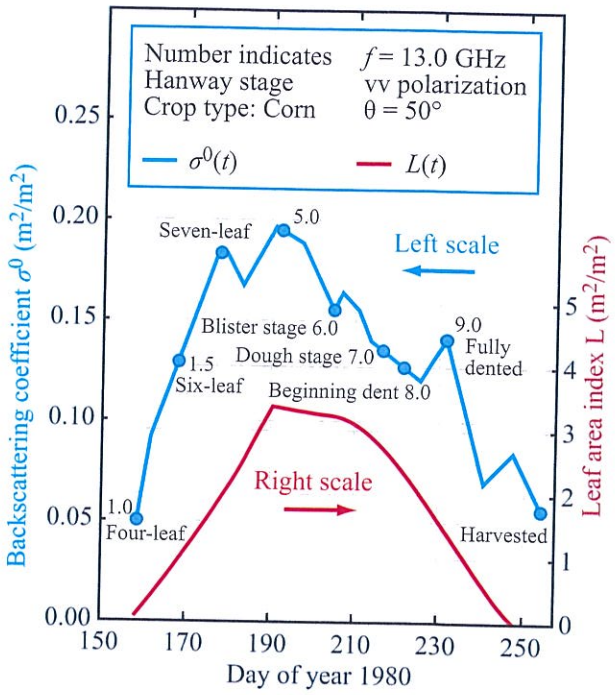

Figure 11-30: Measured temporal patterns of the backscattering coefficient σ^0 and leaf-area index (LAI) of a corn field. Stage of growth is indicated by the Hanway (1971) stage [from Ulaby et al., 1984]. Note that σ^0 is expressed in (m^2/m^2) instead of in dB.

Another example demonstrating high correlation between σ^0 and L is shown in Fig. 11-32 for savannas observed by the SeaWinds 13.6 GHz scatterometer that flew on board of the QuikSCAT satellite (Table 1-2). The incidence angle is $\approx 50°$. The radar data shown in Fig. 11-32, which covers approximately six years (Yang et al., 2011), is highly correlated with the LAI observations made by optical sensors aboard the MODIS satellite.

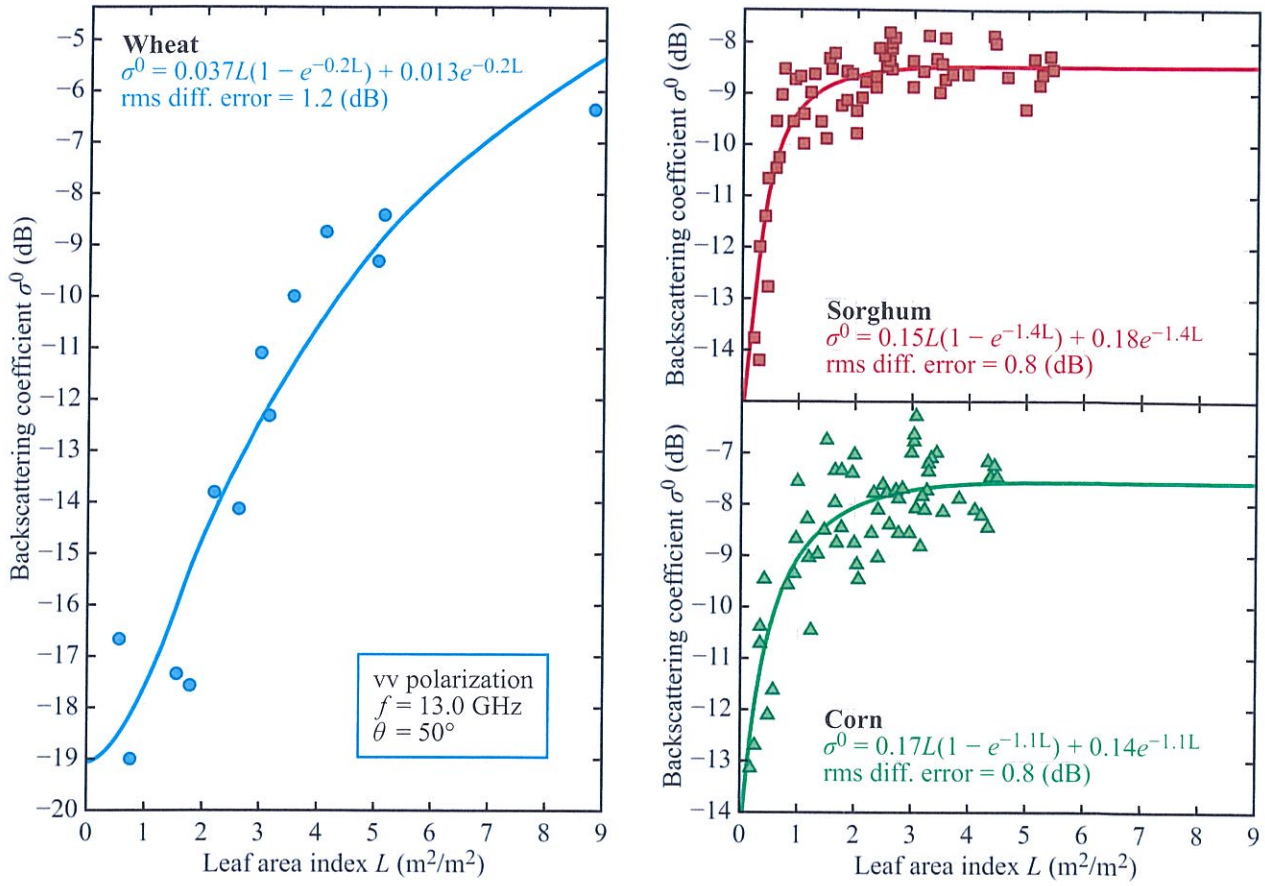

(a) Wheat (b) Sorghum, (c) Corn

Figure 11-31: Comparison of measured backscattering coefficient of (a) corn, (b) wheat, and (c) sorghum with that computed on the basis of the single-parameter (LAI) model.

11-8.6 σ^0 Relationship to Canopy Water Content

As stated earlier, the (green) leaf-area index L should be highly correlated to the ***integrated canopy volume water content*** M_w measured in kg/m^2 and defined as the total mass of water contained in a vertical column of the canopy per unit ground surface area. That is,

$$M_w = M_f - M_d \qquad (\text{kg/m}^2), \tag{11.93}$$

where M_f and M_d are the weights of the biomass fresh and after drying, respectively, above 1 m^2 of the ground surface. In essence, M_w represents the columnar water content of the ***cloud-equivalent*** canopy.

Figure 11-33 displays the results of measurements reported by Macelloni et al. (2001) relating L to M_f, the fresh biomass/m^2, for five crops. Over most of the growing season, M_f is much larger than M_d, so the relationship between L and the canopy volume water content M_w would be only slightly shifted from that shown in Fig. 11-33.

Building on studies aimed at relating σ^0 to biophysical parameters of vegetation canopies (Jin and Liu, 1997; Bouvet et al., 2009; Kim et al., 2000; Maity

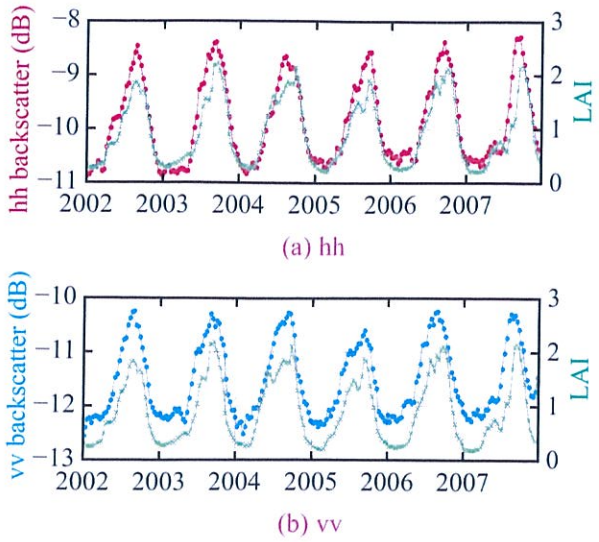

Figure 11-32: The temporal evolution of QuikSCAT backscatter (left axis) at the Savannas (10.528N, 3.976W) from 2002 to 2007, and the green time series is LAI (right axis) [from Yang et al., 2011].

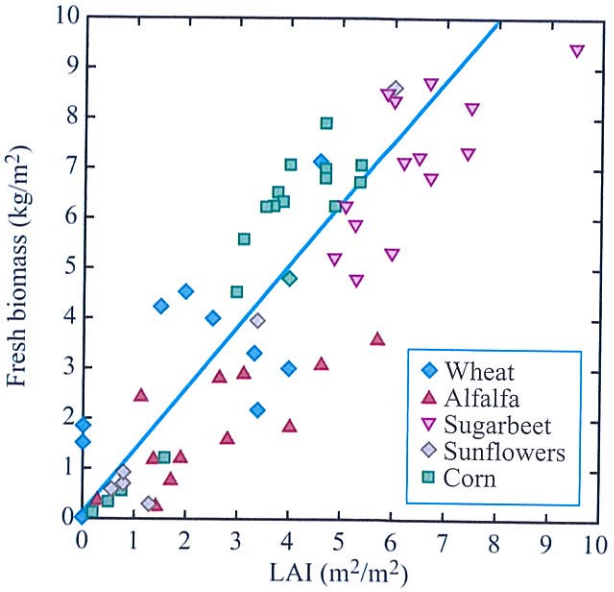

Figure 11-33: Relationship between canopy fresh biomass M_f (kg/m^2) and the leaf area index L (m^2/m^2) of various crop types [from Macelloni et al., 2001].

et al., 2004; Inoue et al., 2002; Oh et al., 2009), Kim et al. (2012) conducted extensive multitemporal experiments for fields planted in rice and soybeans using a ground-based multifrequency polarimetric scatterometer system. The system's center frequencies are 1.27 GHz (L-band), 5.3 GHz (C-band), and 9.65 GHz (X-band). The fields were observed over the entire growth period of the rice and soybeans plants, and all radar observations were made at an incidence angle of 40°.

Figure 11-34 displays plots of the temporal variations of LAI and volumetric moisture content M_w for fields planted in rice and soybeans. As expected, the two quantities are highly correlated to one another, for both types of crops. In part (a) of Fig. 11-35, we display plots of $\sigma^0(t)$ for rice over the growing season for vv, hh, and hv polarizations. In part (b) of the same figure we display a plot of $M_w(t)$ and a temporal plot of a radar-related quantity called the ***radar vegetation index*** (RVI), which was proposed by Kim and Van Zyl (2009) as a parameter for separating vegetation-covered surfaces from bare-soil surfaces. For a canopy composed of randomly oriented thin cylinders, the RVI expression given by Eq. (5.177) reduces to (Kim and van Zyl, 2001):

$$R_{VI} = \frac{8\sigma^0_{hv}}{\sigma^0_{hh} + \sigma^0_{vv} + 2\sigma^0_{hv}} . \qquad (11.94)$$

We observe that R_{VI} and M_v exhibit similar temporal patterns, for both rice and soybeans. The soybeans data are shown in Fig. 11-36.

The study by Kim et al. (2012) concludes with the plots shown in Fig. 11-37, in which M_w is plotted against R_{VI} for both rice and soybeans combined. The sensitivity (slope) of R_{VI} to M_w is highest at L-band and lowest at X-band.

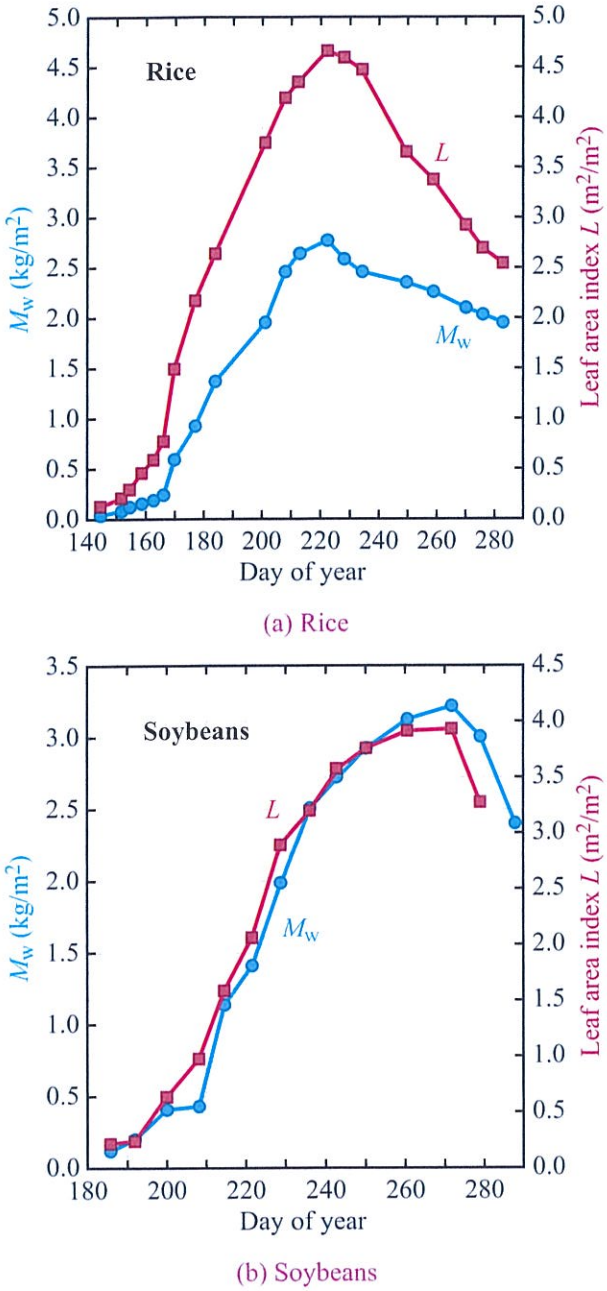

Figure 11-34: Temporal variations of leaf area index L and canopy water content M_w for fields planted in (a) rice and (b) soybeans [Kim et al., 2012].

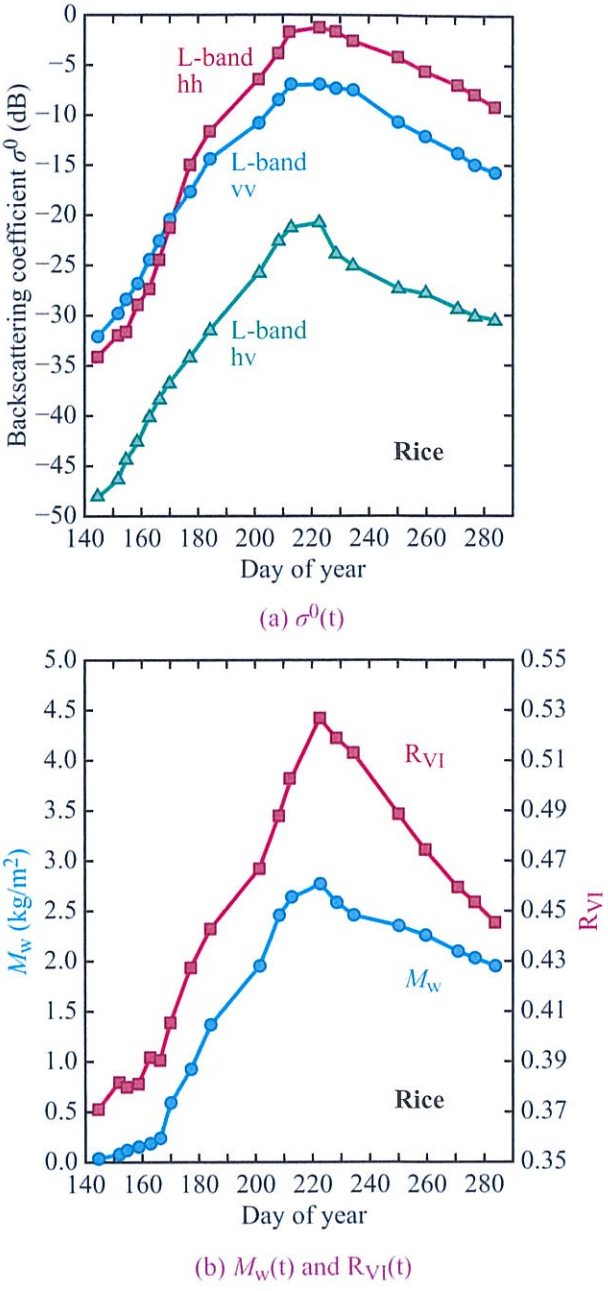

Figure 11-35: Temporal variations of (a) σ^0 and (b) radar vegetation index R_{VI} and canopy water content M_w for a field planted in rice [Kim et al., 2012].

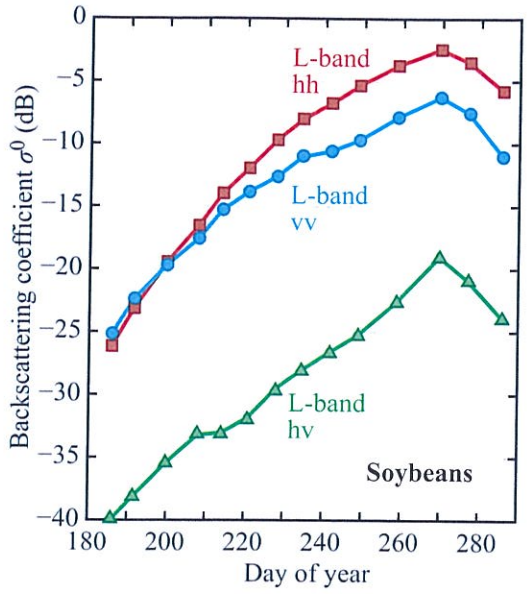

(a) σ^0(t)

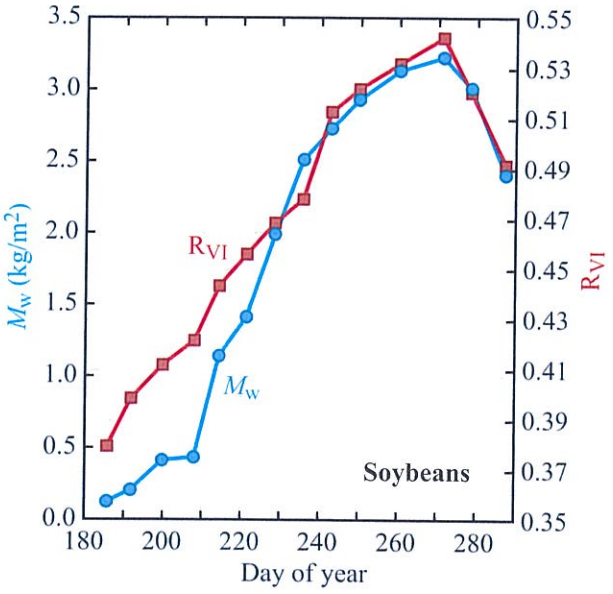

(b) M_w(t) and R_{VI}(t)

Figure 11-36: Temporal variations of (a) σ^0 and (b) radar vegetation index R_{VI} and canopy water content M_w for a field planted in soybeans [Kim et al., 2012].

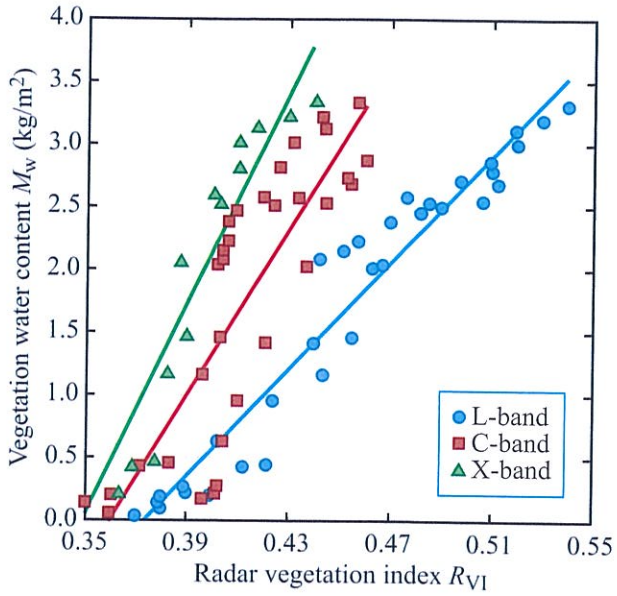

Figure 11-37: Relationship between vegetation water content M_w and L-, C-, and X-band R_{VI} for rice and soybean combined [Kim et al., 2012].

11-9 Soil-Moisture Inversion Example

To explore the possibility of developing an inversion model to estimate the soil moisture content underneath a vegetation canopy from radar observations, De Roo et al. (2001) used a truck-mounted radar to measure the backscatter from two adjacent soybean canopies over the entire growing season of 1996. Fully polarimetric L-band (at 1.25 GHz) and C-band (at 5.4 GHz) scatterometers observed the canopy at an incidence angle of 45° and an azimuth angle of 45° with respect to the row direction. Approximately 60 radar data sets were acquired over a temporal span of 130 days, covering a wide range of conditions, extending from 0.02 kg/m^2 to 0.97 kg/m^2 in vegetation water content M_w, 3% to 26% in volumetric soil moisture content m_v, and 12 cm to 63 cm in canopy depth d. The measured temporal history of m_v is shown in Fig. 11-38. The vertical bars around the mean values of m_v represent the ± 1 standard deviation. The goal of the study is to estimate m_v from the radar observations, while keeping in mind that the

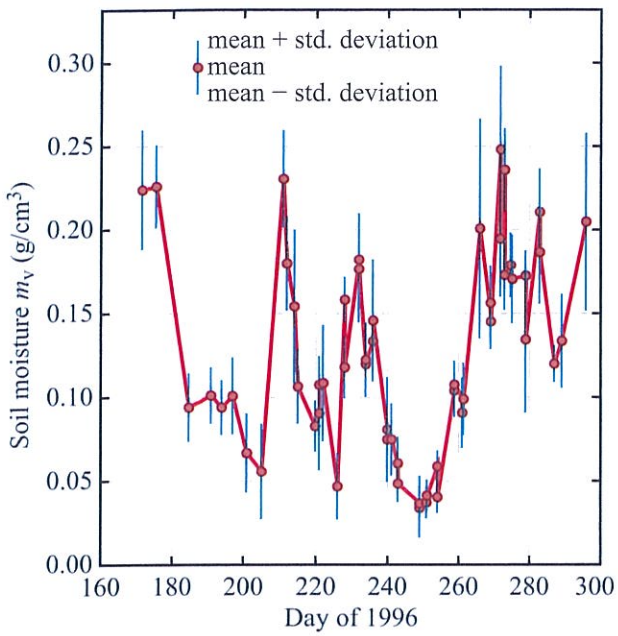

Figure 11-38: Temporal history of volumetric soil moisture content m_v under the soybean canopy. Each moisture value is based on measurements made by a soil-moisture probe at multiple locations [De Roo et al., 2001].

in-situ-measured value of m_v has an error on the order of ± 0.03.

11-9.1 The Direct Model

The investigation reported by De Roo et al. (2001) adopted the single-scattering coherent model given by Eq. (11.17) as

$$\sigma^0_{pq}(\theta_i) = \Upsilon_p \Upsilon_q \, \sigma^0_{s_{pq}}(\theta_i) + \frac{\sigma^{\text{back}}_{v_{pq}} \cos\theta_i}{\kappa_e^p + \kappa_e^q} (1 - \Upsilon_p \Upsilon_q)(1 + \Gamma^p \Gamma^q \Upsilon_p \Upsilon_q) + n \sigma^{\text{bist}}_{v_{pq}} \, d(\Gamma^p + \Gamma^q) \Upsilon_p \Upsilon_q \qquad (p, q = \text{v or h}), \tag{11.95}$$

where Γ^p is the p-polarized soil surface reflectivity at incidence angle θ_i (defined in Table 2-5), $\sigma^0_s(\theta_i)$ is the pq-polarized backscattering coefficient of the soil surface, σ^{back}_v and σ^{bist}_v are the pq-polarized volume backscatter and bistatic scattering coefficients of the soybeans canopy, and Υ_p is the canopy one-way transmissivity,

$$\Upsilon_p = e^{-\kappa_e^p d \sec\theta_i}. \tag{11.96}$$

The index n is 1 for hv polarization and 2 for hh and vv polarizations. The soil-surface backscattering coefficient $\sigma^0_{s_{pq}}$ is modeled by the semiempirical expressions given by Eqs. (10.37) to (10.39), which rely on two physical parameters, namely the rms surface height s and the soil moisture content m_v. The vegetation-related quantities were assumed to depend on the canopy ***water content per unit height***, $\rho_w = M_w/d$, as follows:

$$\sigma^{\text{back}}_{v_{pq}} = a_2^{pq} \rho_w, \tag{11.97a}$$

$$\sigma^{\text{bist}}_{v_{pq}} = a_3^{pq} \rho_w, \tag{11.97b}$$

$$\kappa_e^{pq} = \frac{\kappa_e^p + \kappa_e^q}{2} = a_4^{pq} \sqrt{\rho_w}, \tag{11.97c}$$

$$\Upsilon_p \Upsilon_q = e^{-2\kappa_e^{pq} \sec\theta_i}, \tag{11.97d}$$

where the coefficients a_i^{pq} for $i = 2$, 3, and 4 are free parameters to be determined empirically. In addition, the expression given by Eq. (11.95) is multiplied by an empirically determined scaling constant a_1^{pq}.

At each frequency (1.25 GHz or 5.4 GHz) and polarization configuration (hh, vv, or hv), the known or measured quantities are θ_i, d, ρ_w, and $\sigma^0_{pq}(\theta_i)$, and the unknown parameters are a_i^{pq}, for $i = 1$ to 4, and the surface rms height s. To determine s, radar measurements were made early in the growing season and then used in PRISM-1 to invert for the value of s, which was found to be 2.8 cm. Using an error minimization routine, the values of the other four unknown parameters were selected such that the multiparameter error between the measured and computed values of σ^0 is a minimum. The result of the parameter-fitting process led to the values given in Table 11-2. Among the six frequency-polarization combinations, the rms error between measured and computed values of σ^0 is between 0.55 dB and 0.81 dB, which is comparable to the precision of the radar measurements. The parameter P is an indicator of the

Table 11-2: Best-fit free parameters for the semiempirical soybean model [De Roo et al., 2001].

f (GHz)	Pol	a_2	a_3	a_4	a_1	rms error	max error	P
		m^2/kg	m^2/kg	$Np/(kg/m)^{1/2}$	dB	dB	dB	%
5.4	hh	0.151	$=a_2$	0.341	2.50	0.71	1.79	23
5.4	vv	0.170	$=a_2$	0.484	3.47	0.73	1.82	16
5.4	hv	0.051	$=a_2$	0.948	5.16	0.55	1.26	84
1.25	hh	0.0	0.132	0.126	3.39	0.81	1.38	1.5
1.25	vv	0.0025	0.0605	0.0	4.78	0.62	1.81	49
1.25	hv	0.0	0.0351	0.125	5.06	0.70	1.95	15

goodness-of-fit of the model. A good fit requires P to be greater than 5%. In Table 11-2, $P > 5\%$ for five of the six frequency-polarization combinations. Comparisons of the semiempirical model calculations with the measured data are shown in Figs. 11-39 and 11-40 for L-band and C-band, respectively. Overall, the model tracks the temporal variations of the radar measurements quite well.

11-9.2 The Inverse Model

The goal of the inverse model is to use the radar data to obtain reliable estimates of the volumetric soil moisture content m_v and the canopy water content M_w. Because the direct model is highly nonlinear in M_w, it is very difficult to invert it analytically. The alternative is to explore empirical relations involving ratios of backscattering coefficients. The process led to the following inverse models:

Soil Moisture:

$$m_v = 0.234 + 0.024\sigma^0_{L-vv} - 0.014(\sigma^0_{C-hv} - \sigma^0_{C-vv}) \quad (g/cm^3),$$

$$\text{rmse} = 1.75\%, \qquad R^2 = 0.90, \qquad (11.98)$$

with all three σ^0 values expressed in dB. Note that the ratio of two quantities in natural units becomes the difference between their values when their values are converted to dB.

Canopy Water Content:

$$M_w = 3.84\left(\frac{\sigma^0_{L-hv}}{\sigma^0_{L-vv}}\right)^{0.97} \quad (kg/m^2),$$

$$\text{rmse} = 0.068\ kg/m^2, \qquad R^2 = 0.87, \qquad (11.99)$$

and in this case, σ^0 is in (m^2/m^2).

Comparison of radar-derived values with *in-situ* measurements is provided in Fig. 11-41.

11-10 Look-Direction Dependence

In Section 9-4.2 we examined the dependence of σ^0 on the radar look direction for periodic bare soil surfaces, wherein we defined the ***look direction*** as the azimuth angle ϕ_0 between the ground projection of the antenna beam axis and the row direction. Parallel-look direction is designated $\phi_0 = 0$ and perpendicular-look direction is designated $\phi_0 = 90°$. Now we consider a similar situation for row crops.

Using truck-mounted multifrequency scatterometers, Batlivala and Ulaby (1976) and Ulaby and Bare (1979) conducted several experiments to determine the variation of σ^0 with incidence angle θ at $\phi_0 = 0$ and $\phi_0 = 90°$ for fields planted in soybeans and wheat. Samples of their results are shown in Figs. 11-42 and 11-43 for a soybeans canopy observed at 1.1 GHz and 4.25 GHz, respectively. Strong sensitivity is observed for hh polarization at 1.1 GHz, whereas independence of look direction is observed at 4.25 GHz and higher

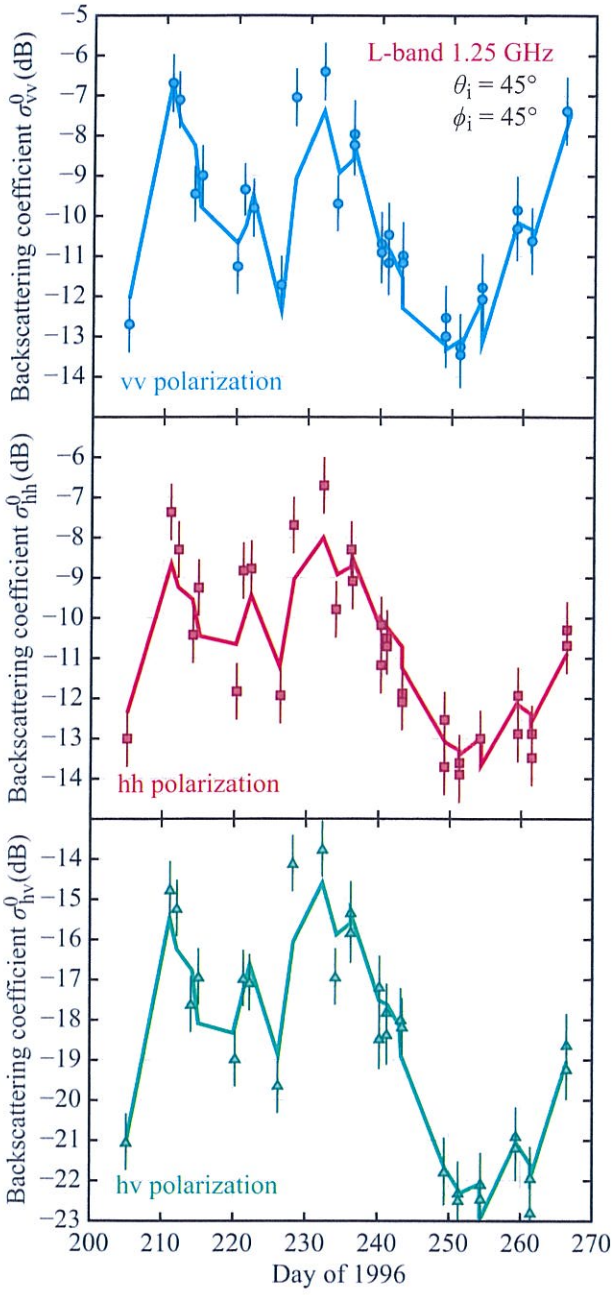

Figure 11-39: Comparison of the semiempirical model with the measured data at L-band [De Roo et al., 2001].

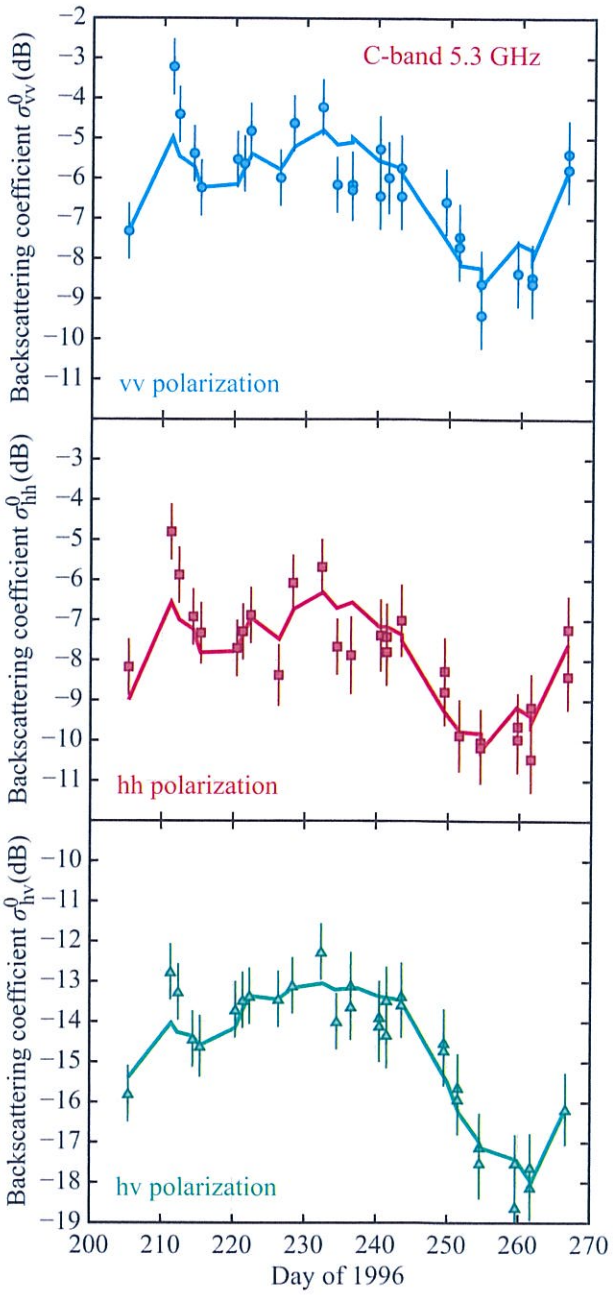

Figure 11-40: Comparison of the semiempirical model with the measured data at C-band [De Roo et al., 2001].

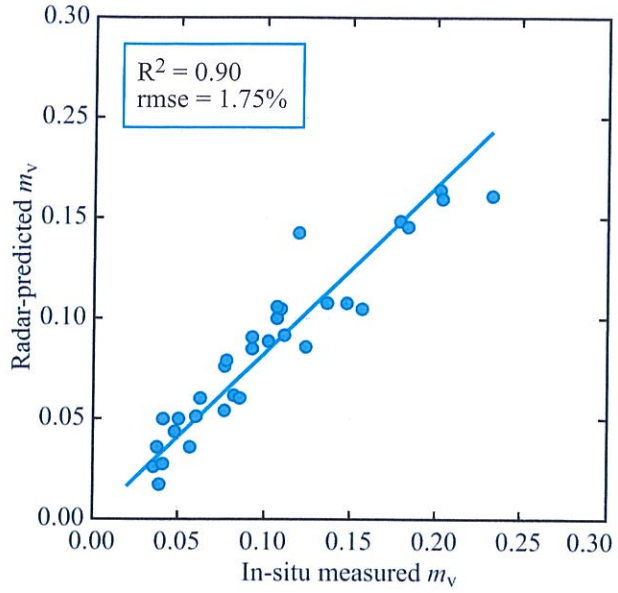

(a) m_v

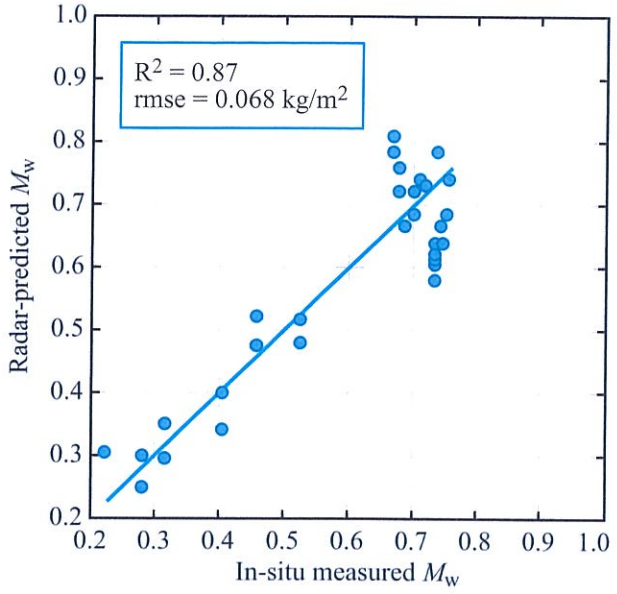

(b) M_w

Figure 11-41: Comparison of (a) *in-situ* measured soil moisture with inverted soil moisture derived from radar measurements, and (b) similarly for canopy water content M_w [De Roo et al., 2001].

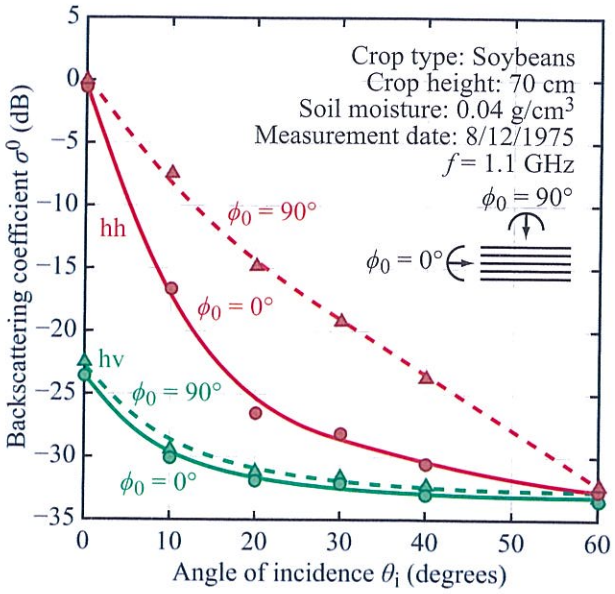

Figure 11-42: Comparison of the angular responses of $\sigma^0_\perp$ ($\phi_0 = 90°$) and $\sigma^0_\parallel$ ($\phi_0 = 0$) of a soybeans canopy at 1.1 GHz.

frequencies. Also, for hv polarization, σ^0 appears to be independent of look direction at all microwave frequencies. This observation for hv is consistent with the base-soil results discussed in Section 10-4.2, as well as with the attenuation data reported in Figs. 11-25 and 11-26. Similar conclusions were reached for wheat and other canopies observed at various stages of growth.

► For fields planted in wheat, soybeans, and corn, σ^0_{hh} and σ^0_{vv} exhibit no sensitivity to radar look direction (relative to row direction) so long as $f \gtrsim 4$ GHz. For cross polarization, σ^0_{hv} exhibits no sensitivity to look direction at all frequencies even as low as 1 GHz. ◄

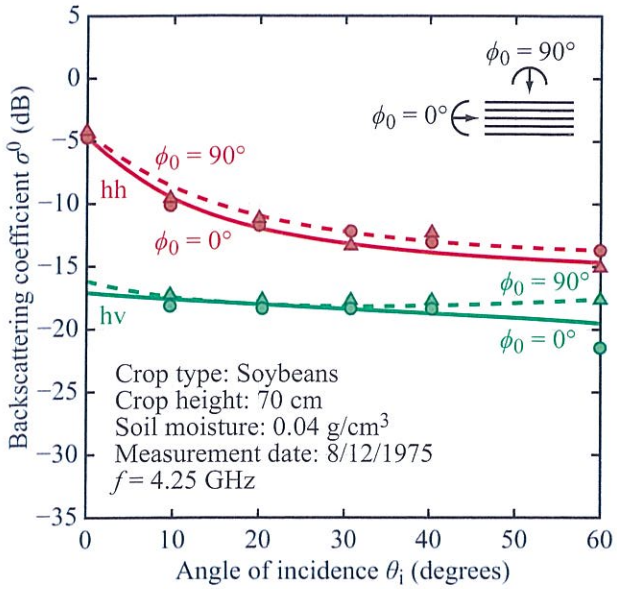

Figure 11-43: Comparison of the angular responses of $\sigma^0_\perp$ ($\phi_0 = 90°$) and $\sigma^0_\parallel$ ($\phi_0 = 0$) of a soybeans canopy at 4.25 GHz.

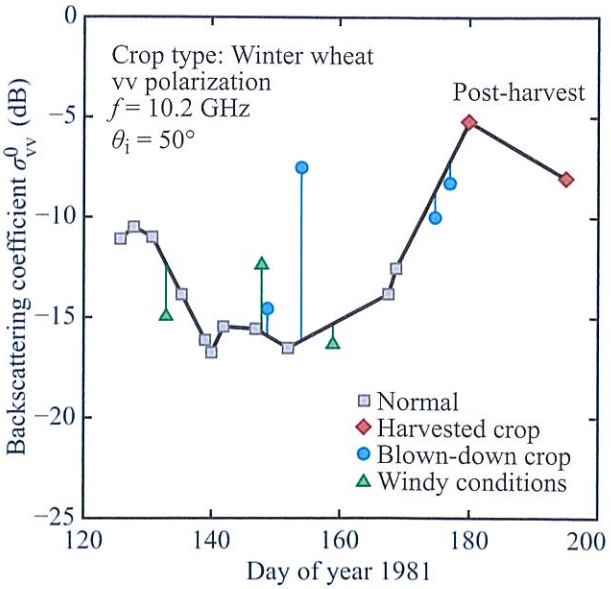

Figure 11-44: The solid curve connects backscattering measurement points made for a wheat canopy under "normal" environmental conditions. Deviations from the normal pattern caused by winds are denoted ▲, and those related to rain-caused "blowdown" by ●.

11-11 Effects of Dew, Wind, and Other Environmental Factors

The backscattering models and experimental data presented in the preceding sections pertain to "normal environmental and crop developmental conditions." Ordinarily, such models are based on certain assumptions about canopy geometry, which if violated are likely to render the model invalid. For example, logically, a wheat-canopy model is based on the assumption that most of the wheat stalks in the canopy are vertically oriented, which is a reasonable assumption under normal conditions. However, in the presence of strong winds, the stalks are likely to be bent away from the vertical by the force of the wind, thereby violating the model's initial assumption. Moreover, the effects of abnormal environmental factors usch as strong winds, heavy rain, and hail on σ^0 of a vegetation canopy are difficult to incorporate into the design of a backscattering model because of the associated complexity of the canopy's geometry. Hence, such effects may be regarded as deviations from normal behavior, as illustrated in Fig. 11-44. The plot consisting of line segments that connect points denoted by solid squares (■) represents the temporal variation of σ^0_{vv} for a field of winter wheat observed during the latter part of the wheat's growth cycle. These points are regarded as "normal" data according to the criteria that (a) relatively calm winds (i.e., with gusts of less than 25 mph) prevailed at the time of measurement and (b) the canopy's geometry appeared normal to visual inspection. The points denoted by triangles (▲) represent observations made for wind conditions under which the wheat plants were bent away from their normal, vertical orientation, and the points denoted by solid circles (●) represent observations of a canopy partially damaged by heavy rain, strong wind, or hail, which are collectively referred to as "blown-down" canopies.

The presence of water droplets on the leaf surfaces

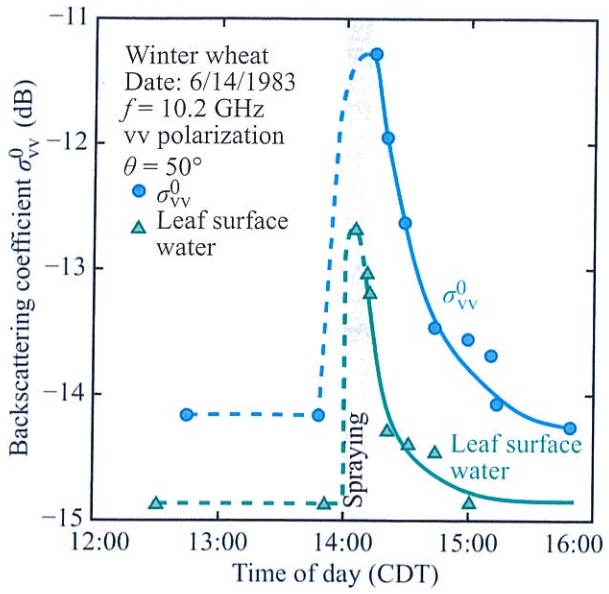

Figure 11-45: The presence of water droplets on the leaves of wheat plants can have a significant effect on σ^0 [Allen et al., 1984].

of plants—dew, for example—can modify the scattering behavior of the canopy. To evaluate this effect, Allen et al. (1984) conducted an experiment in which σ^0_{vv} of a winter wheat canopy was measured prior to and immediately after the canopy had been sprayed with water (Fig. 11-45). Conductivity plates were attached to the wheat stalks to monitor the amount of water (which the leaves retain in the form of surface droplets) present as a function of time following spraying. The conductivity plates have thermal properties similar to those of vegetation and thereby act as leaf analogs from the standpoint of the evaporation rate of surface water. The plots in Fig. 11-45 indicate that σ^0_{vv} increased by about 3 dB as a result of the spraying and then decreased to its original level over a period of about two hours as the surface water of the leaves evaporated. The experiment demonstrated that the effect of leaf-surface water on σ^0_{vv} may be significant, although its variation with frequency, angle, and polarization has not yet been established.

11-12 Radar Backscattering from Tree Canopies

11-12.1 Propagation Properties of Forest Canopies

Because a forest canopy is an inhomogeneous, random, and possibly anisotropic medium, proper characterization of its propagation properties entails measuring the attenuation loss and phase delay through many paths, so as to establish the mean values and associated statistics. The quantities of interest are the attenuation (optical depth) τ_h and τ_v for horizontal and vertical polarization, and the ***polarization phase difference*** $\Delta\phi = \phi_v - \phi_h$, where ϕ_v and ϕ_h are the one-way phase delays for v and h polarizations.

To demonstrate how to measure these quantities, Ulaby et al. (1990b) used a 1.6 GHz polarimetric scatterometer mounted atop a 19 m high platform, looking down at a dense, 13.7 m tall canopy of pine trees. The incidence angle was 40°. Figure 11-46(a) depicts the layout. The truck boom was rotated in a conical scan arrangement, thereby maintaining the range to the ground constant for all measurements. A total of 30 measurements were made, approximately 1 m apart. The first four locations were outside the canopy, and the remaining locations were inside the canopy. At each location, two scattering matrix measurements were made, one with a trihedral reflector placed in the illuminated area and another without the trihedral reflector. The dimensions of the antenna footprint on the ground were 2.3 m in the azimuth direction and 2.5 m in the range direction. The front surface of the trihedral reflector had 85 cm edges. The combination of 30 scattering matrix measurements, with and without the trihedral reflector, allowed for extracting values for the horizontal and vertical polarized attenuations τ_h and τ_v (both in dB), as well as $\Delta\phi = \phi_v - \phi_h$. The distributions and mean values are shown in Fig. 11-47.

The attenuation values extend over a wide range, from $\tau \approx 0$ for an unobstructed view of the radar beam through the canopy, to about 4.6 Np (or approximately 20 dB) for a beam intercepted by several trees. The average one-way attenuation $\tau_{av} \approx 2$ Np, which

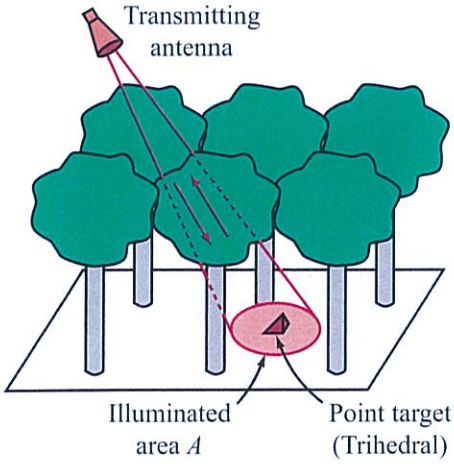

(a) Sketch showing a receive antenna placed under trees for measuring propagation properties of canopy

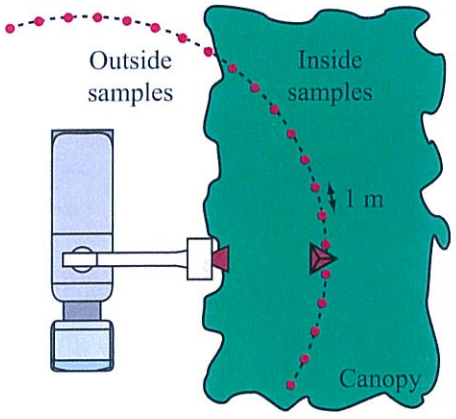

(b) Plan view of attenuation experiment arrangement

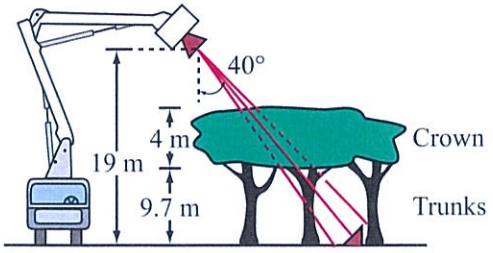

(c) Elevation of attenuation experiment arrangement

Figure 11-46: Tree attenuation experiment setup used by Ulaby et al. (1990b) at 1.6 GHz.

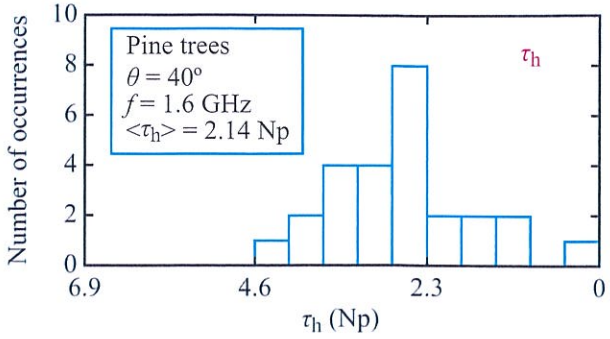

(a) h-pol attenuation

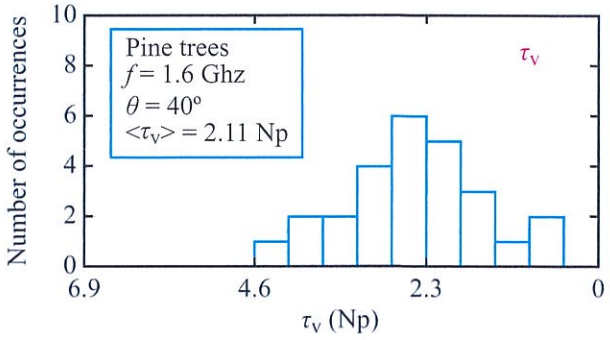

(b) v-pol attenuation

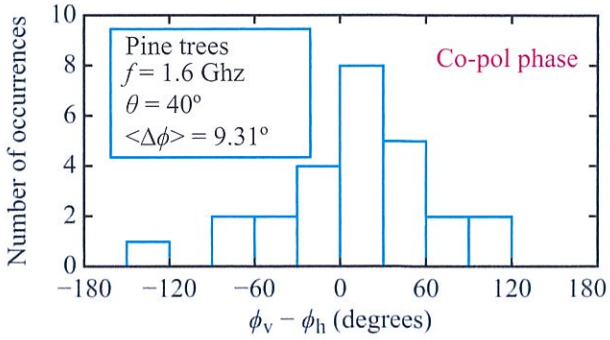

(c) Co-pol phase difference

Figure 11-47: Measured distribution of one-way attenuations τ_h and τ_v, and phase delay difference $\Delta\phi$ [Ulaby et al., 1990b].

corresponds to a two-way transmissivity

$$\Upsilon^2 = e^{-2\tau_{av}} = e^{-4} \approx 0.02.$$

Hence, except possibly along incidence directions very close to normal incidence, even at the low microwave frequency of 1.6 GHz, the attenuation by the canopy is sufficiently high as to reduce the average ground backscattering contribution to a level much smaller than that of the canopy's direct backscattering contribution. In general, τ_{av} increases with frequency, so the aforementioned conclusion should be valid not only at L-band, but also across the microwave spectrum ($f \geq 1$ GHz). Obviously, this assertion does not apply to short or sparse canopies, but when it does, the canopy appears like a semi-infinite lossy medium, in which case Eq. (11.18) is applicable:

$$\sigma^0_{pq}(\theta) = \frac{\sigma^{\text{back}}_{v_{pq}} \cos\theta}{\kappa_e^p + \kappa_e^q}, \qquad (p,q = \text{h or v}).$$

For a particular tree canopy, the volume backscattering coefficient $\sigma^{\text{back}}_{v_{pq}}$ and the extinction coefficients κ_e^p and κ_e^q are likely to have constant values over a wide range of the incidence angle θ. Hence, σ^0_{pq} should exhibit a simple cosine dependence, or equivalently, $\gamma_{pq} = \sigma^0_{pq}/\cos\theta$ should exhibit a flat response. This is indeed the case, as shown in the next subsection.

In a similar study reported by Kurum et al. (2009), which also used a truck-mounted platform (Fig. 11-48), time-domain analysis of the recorded backscattered signal was used to measure the signal attenuation τ of a tree canopy composed of 11–14 m tall trees with approximately 13 kg/m^2 in above-ground biomass. The measurements were conducted at 1.25 GHz, along four incidence angles (15° to 45° in 10° increments), and for two canopy conditions: full-canopy and leaf-drop (no leaves). Their results, which were reported in dB, were converted to Np and are plotted in Fig. 11-49. These are average values based on observations made along 28 different azimuth orientations. As expected, τ_{av} increases with incidence angle for both wave polarizations and both canopy conditions. In general, τ_{av} is slightly larger for v polarization, and the leaf-drop attenuation is about 10% smaller than its full-canopy counterpart.

Figure 11-48: 1.25 GHz radar system deployed over a stand of Paulownia trees [Kurum et al., 2009].

11-12.2 Angular and Frequency Response of σ^0

Most tree canopies are spatially nonuniform, consisting of a random distribution of trees (or groups of trees) and open spaces. Hence, to obtain a representative value for the backscattering coefficient σ^0 of a tree canopy, it is important that sufficient spatial and temporal averaging be performed during the measurement process to ensure that the measured value of σ^0 is not adversely influenced by wind or local variations of the canopy cover fraction. This consideration is particularly important for high-resolution observations (such as those made using a low-altitude, narrowbeam scatterometer or a high-resolution imager) at angles close to normal incidence.

As noted earlier, if we model a tree canopy as a

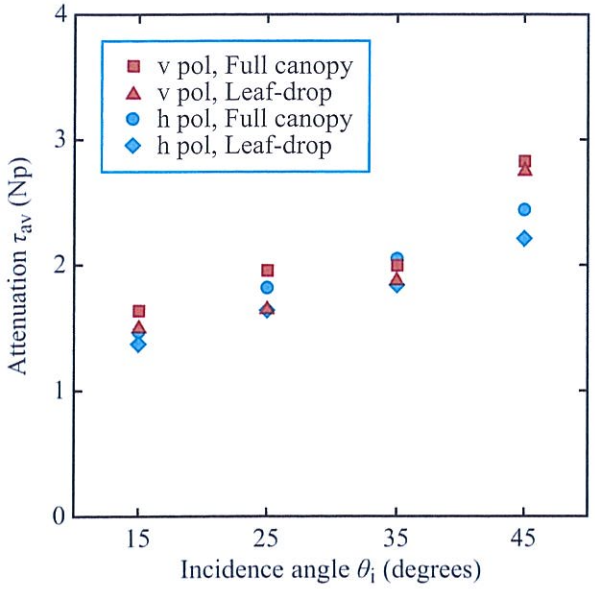

Figure 11-49: Average one-way attenuations through a canopy of Paulownia trees under full-canopy and leaf-drop conditions. Tree height ≈ 11–14 m and above-ground biomass ≈ 13 kg/m^2 [Kurum et al., 2009].

lossy scattering volume consisting of a collection of random scatterers of varying sizes and orientation, its backscattering coefficient σ^0 should exhibit an angular dependence approximately equal to $\cos\theta$, which is equivalent to $\gamma(\theta) = \sigma^0(\theta)/\cos\theta = \text{constant}$. Such an angular variation is indeed typical of most observations reported in the literature; the examples given in Fig. 11-50 for deciduous trees at 3.3 GHz and 8.6 GHz show that $\gamma(\theta)$ is essentially constant (within 1 to 2 dB) for $\theta \geq 20°$ for all linear polarization configurations. In general, deciduous trees in leaf exhibit a σ^0 level higher than that of defoliated trees (leaf-drop) by typically 2 to 8 dB, depending on angle, frequency, and polarization (Figs. 11-51 and 11-52). These observations are based on measurements made over the 1–18 GHz band. Similar observations were noted by Trebits et al. (1978) on the basis of their measurements at 9.4, 35, and 95 GHz.

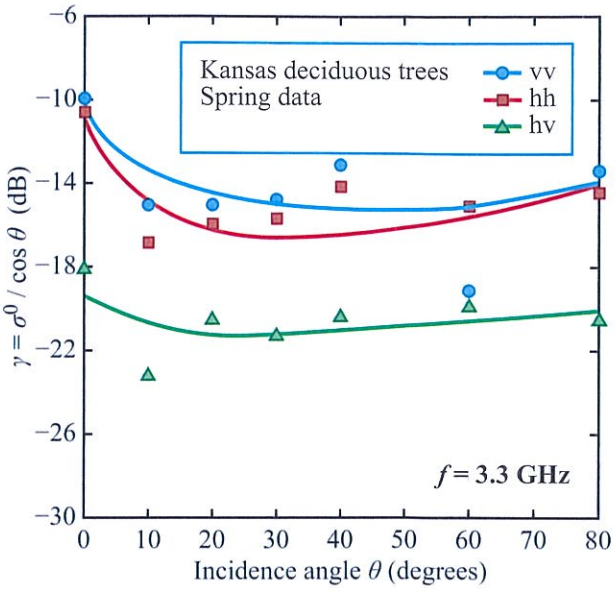

(a) 3.3 GHz

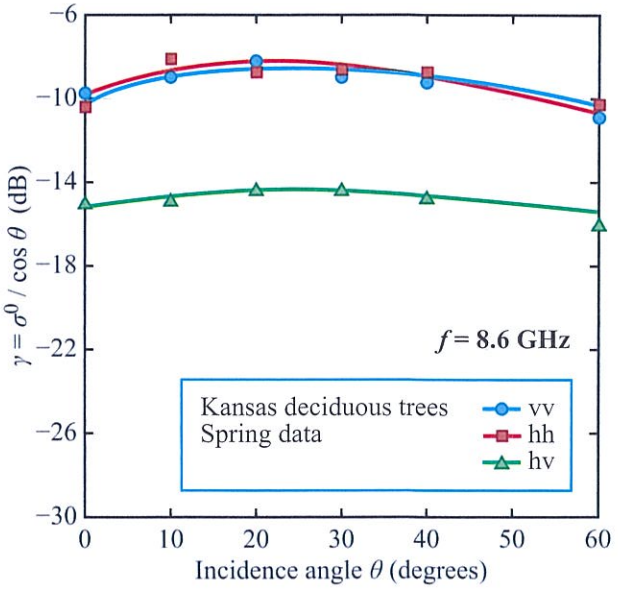

(b) 8.6 GHz

Figure 11-50: Angular variation of γ at 3.3 and 8.6 GHz as a function of θ for deciduous trees with leaves [from Bush et al., 1976]. Note that $\gamma\,(\text{dB}) = 10\log(\sigma^0/\cos\theta)$.

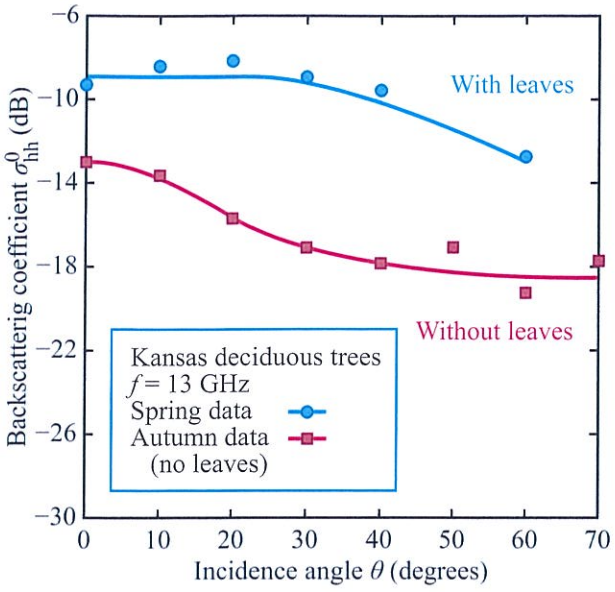

(a) hh polarization

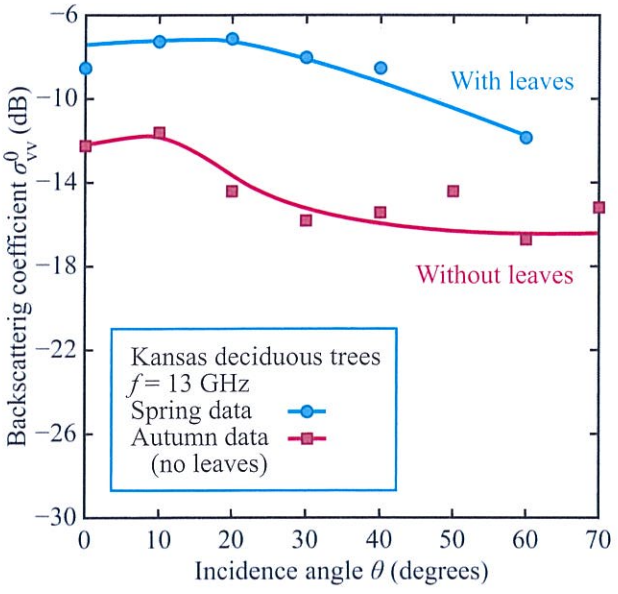

(b) vv polarization

Figure 11-51: Angular variation of σ^0_{hh} of trees measured at 13.0 GHz in the spring and autumn [from Bush et al., 1976].

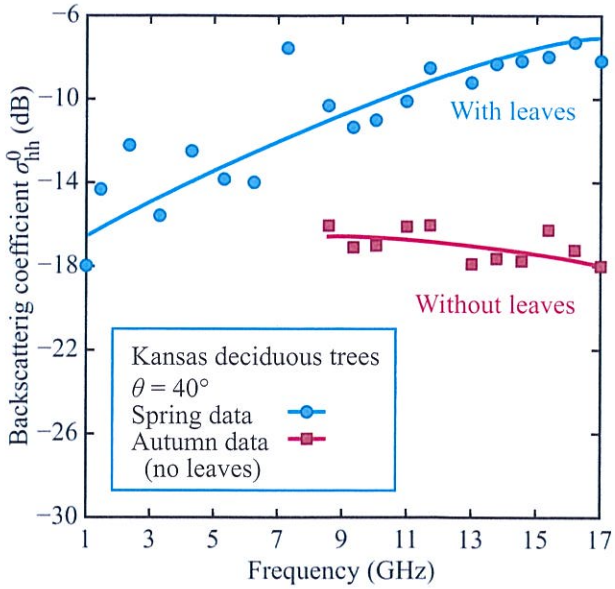

(a) hh polarization

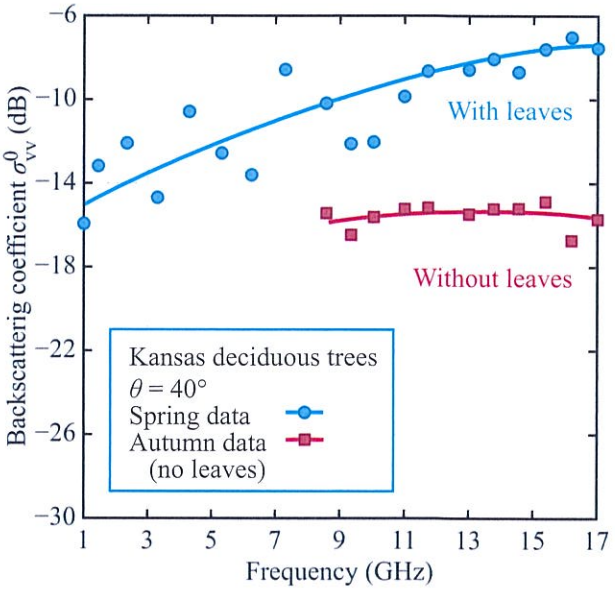

(b) vv polarization

Figure 11-52: Spectral responses of (a) σ^0_{hh} and (b) σ^0_{vv} of trees measured at 40° [Bush et al., 1976].

11-12.3 MIMICS

The purpose of this subsection is to demonstrate that the single-scattering solution of the radiative transfer equation is perfectly suitable for modeling the backscatter from forest canopies, provided sufficient care is taken in characterizing the physical and dielectric properties of the canopy and underlying soil surface. We do so by offering a brief overview of MIMICS: the *Mi*chigan *Mi*crowave *C*anopy *S*cattering model. The first generation of MIMICS, known as MIMICS-1, was developed by Ulaby et al. (1988c) for canopies with continuous crown layers. Later generations addressed discontinuous canopies (McDonald and Ulaby, 1993) and periodic canopies (Whitt and Ulaby, 1994). We limit our present discussion to MIMICS-1 (continuous canopies).

MIMICS-1 is a generalized version of the single-scattering solution given in Section 11-6; it is fully polarimetric, which means that all scattering and extinction processes are defined in terms of 4×4 matrices. It models a forest canopy as two distinct horizontal vegetation layers over a dielectric ground surface (Fig. 11-53), the top layer contains the tree crowns, has vertical extent h_c, and consists of an appropriate combination of leaves and branches. The bottom layer contains the tree trunks and has height h_t. The leaves are modeled as flat circular disks of radius a and orientation (θ, ϕ), where θ is the angle between the zenith direction and the vector normal to the leaf surface. Similar definitions apply to the branches and the trunks, both of which are modeled as dielectric cylinders.

Walnut canopy experiment

In 1987, a field experiment was carried out at the Kearney Agricultural Center in Fresno, California, using the University of Michigan POLARSCAT system. The site contained separate orchards of water-stressed and unstressed plots of walnut trees. This study pertains to the orchard with unstressed trees. The trees were irrigated in the evening with the amount of water equivalent to 100% of the water that evaporated from the canopy during the day, as determined by meteorological measurements made at a nearby weather station. The radar experiments were designed to investigate the backscatter response to diurnal variations in canopy condition. Two experiments were conducted. The first is a set of multiangle measurements (40°–55°) recorded over a short span of 2 hours. The second set consisted of a three-day measurement series during which the walnut canopy was observed continuously at $\theta = 55°$.

Canopy architecture

Statistical sampling of the canopy geometry was performed for eight trees. It included measuring the length, diameter at midlength, and zenith and azimuth orientation angles for all branches with diameters greater than 2 cm. The number and size classes of all lateral branches were also recorded. All branch segments were numbered so that the tree skeletons could be reconstructed from these observations. In addition, the smaller branches with diameters less than 4 cm were statistically subsampled by class size. Four sample classes were considered (0–1, 1–2, 2–3, and 3–4 cm diameters). To adapt the branch geometry data for input to MIMICS, the orchard is divided into distinct crown and trunk layers with heights 2.5 m and 1.7 m, respectively. These heights correspond to the observed canopy architecture. The branches are then divided into four size classes. Figure 11-54 is a sketch of the geometry of an individual tree, showing the four branch classes and the leaves. The larger branches tend to be located in the lower portion of the canopy and are therefore considered to be part of the trunk layer. This layer consists of the trunk-branch size class and includes the tree trunks and all branches with diameters greater than 4.0 cm. The remaining three branch size classes are distributed throughout the crown layer.

In general, the larger branches tend to have mostly vertical orientations whereas the smaller branches exhibit no preferred orientation. Plots of the branch orientation pdfs are shown in Fig. 11-55. The branches in the trunk layer were assigned a $\cos^6\theta$ distribution so that the mean value of θ is 0. The primary branches were assigned a distribution of $\sin^4(2\theta)$ so that θ has a mean value of 45°. The secondary branches and higher-order stems were assigned spherical distribution functions $(\sin\theta)$ so that they show no preferred pointing direction

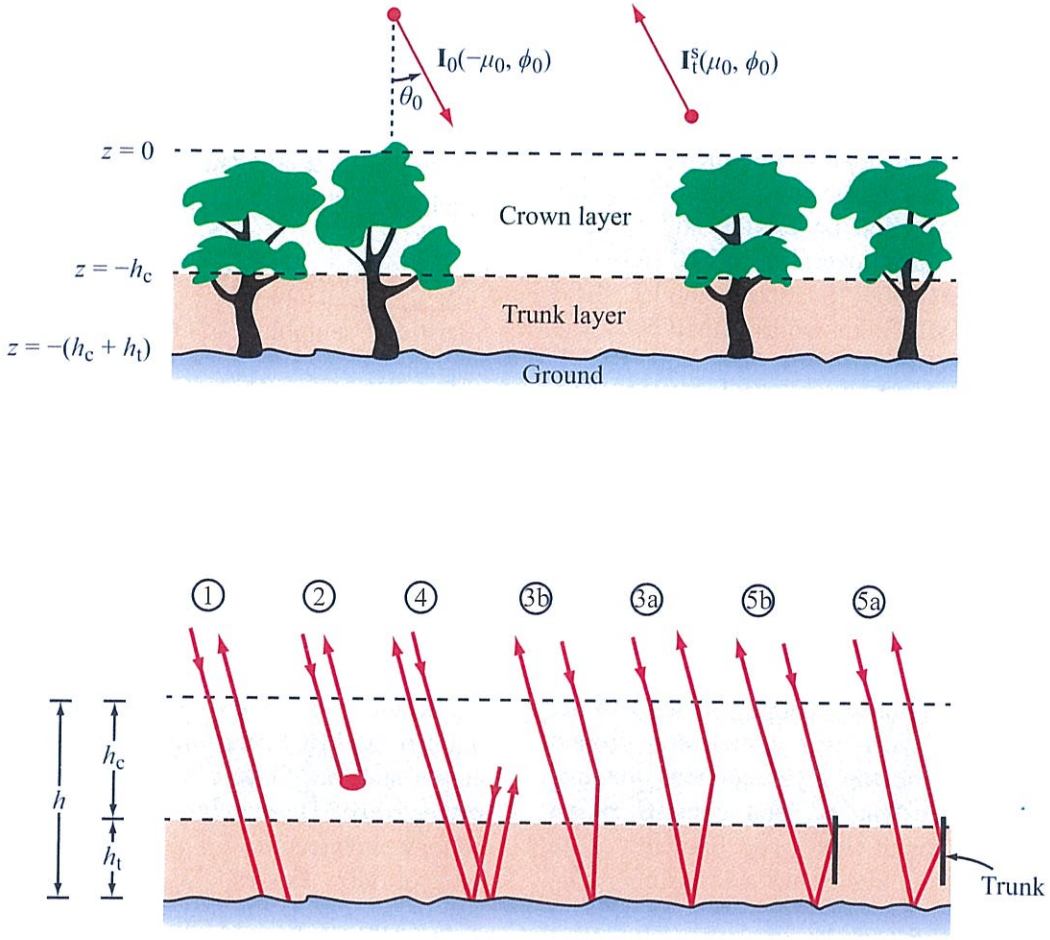

Figure 11-53: Illustration of geometry used to model tree canopy and scattering contributions obtained by MIMICS-1 [Ulaby et al., 1990b].

in the elemental solid angle $d\Omega = \sin\theta\ d\theta\ d\phi$. This implies that these branches are oriented such that their axis directions are uniformly distributed on a spherical surface.

Canopy dielectric constant

Observations of the relative dielectric constant of soil and vegetation were made *in situ* at 1.2 GHz using a field portable dielectric probe. Observations were made of the soil surface and tree trunks. Trunk measurements included both the exterior bark and the interior sapwood. The vegetation measurements were made using coaxial probe tips designed specifically for insertion into the tree boles. A statistically insignificant amount of dielectric data were obtained for the vegetation in the crown layer. However, the dielectric behavior of these constituents may be inferred from observations of other canopy physiological parameters—and the models applied here to predict the relative dielectric constant do in fact agree with the few recorded observations.

The dielectric properties of the tree boles were seen to vary dramatically with time and exhibit a repetitive

Leaf density	652 leaves / m^3
Average leaf diameter	5.0 cm
Average leaf thickness	0.02 cm
Leaf area index	3.2
Leaf orientation pdf	spherical

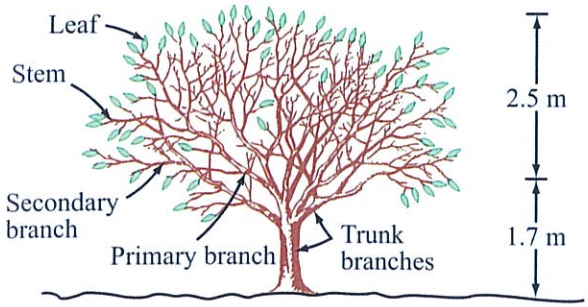

Characteristic	Branch size class			
	Trunk branches	Crown branches		
		Primary	Secondary	Stems
Max. diam. (cm)	-	4.0	0.9	0.4
Min. diam. (cm)	4.0	0.9	0.4	-
Ave. diam. (cm)	7.3	1.9	0.6	0.1
Ave. length (cm)	92.8	35.8	10.9	5.0
Density (# / m^3)	0.13	1.55	1.41	900
Orientation $f(\theta)$	$\cos^6\theta$	$\sin^4 2\theta$	$\sin\theta$	$\sin\theta$

Figure 11-54: Illustration of walnut tree showing four branch classes and leaves [McDonald et al., 1991].

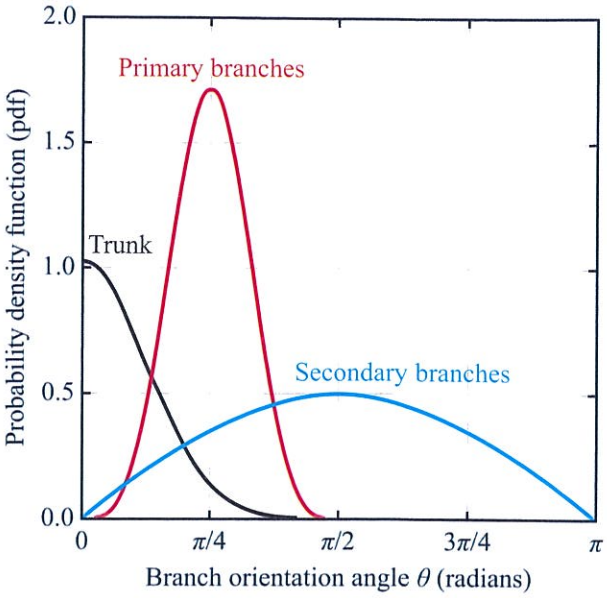

Figure 11-55: Branch orientation probability distribution functions [McDonald et al., 1991].

diurnal pattern. Figure 11-56 shows a piecewise fit to the measured values of the dielectric constant. The numbers on the time axis correspond to midnight on that day of August. The dielectric constant is seen to reach a peak near daybreak at about 6:00 am. Shortly thereafter, the values decrease rapidly until a minimum is reached at about 12 noon. Beginning at about 7:00 pm, the dielectric constant increases until the maximum is reached again. These trends are consistent with data observed throughout the entire course of the experiment. Note that ε'_v varies between a low of 10 and a high of 75, close to that of water.

Soil dielectric constant

The soil was monitored on an hourly basis. Each observation consisted of a minimum of 15 independent, randomly selected samples used to calculate the mean ε_{soil} of the surface layer. Because of spatial variations associated with the locations of the sprinkler heads used to irrigate the soil, the measured dielectric data exhibited a high degree of scatter that made it difficult to estimate an effective soil dielectric. Therefore the soil surface area that received irrigation and remained mostly wet was analyzed separately from the area that received no irrigation and remained mostly dry (Fig. 11-57). The overall effective dielectric behavior was then estimated by combining these results.

Angular response of σ^0

To test the MIMICS-1 model, it was run as a function of θ for $f = 1.25$ GHz using the geometrical information given in Figs. 11-54 and 11-55 and the dielectric constant data listed in conjunction with

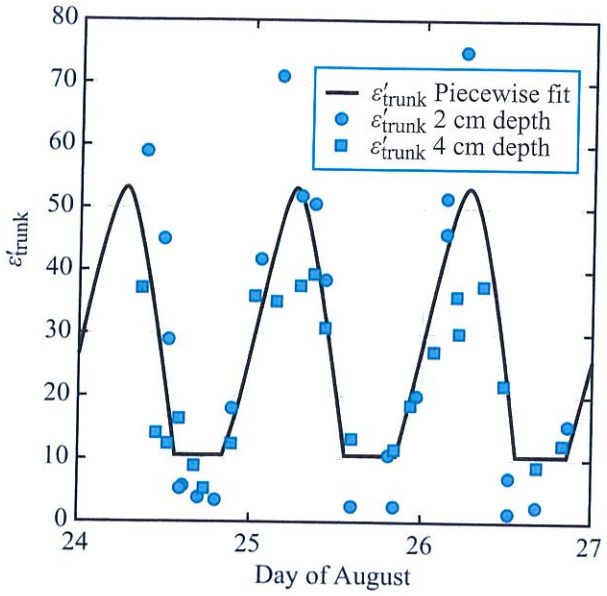

(a)

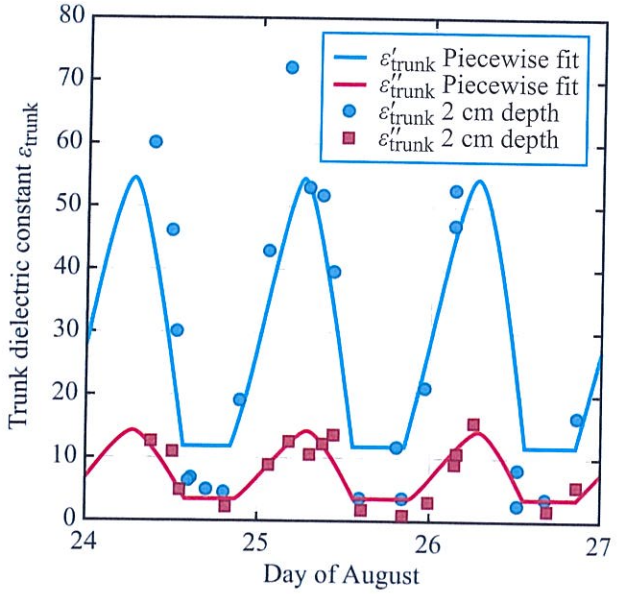

(b)

Figure 11-56: Comparison of periodic piecewise fit to measured trunk dielectric constant data: (a) for two insertion depths and (b) for real and imaginary parts at 2 cm insertion point [McDonald et al., 1991].

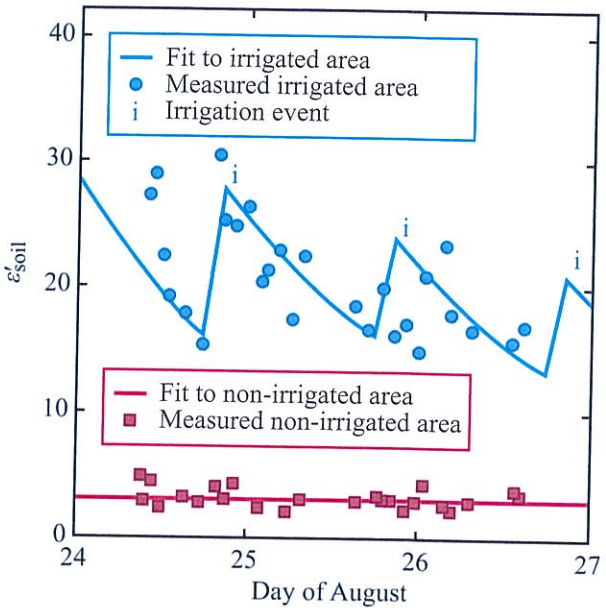

Figure 11-57: Behavior of soil dielectric constant. Fits to measured dielectric constants of irrigated and nonirrigated areas. The (i) indicates beginning of 2.5-hour irrigation period [McDonald et al., 1991].

Fig. 11-58. These dielectric values were measured at the approximate time of the multiangle experiment. The comparison of modeled and measured data shown in Fig. 11-58 demonstrates very good agreement between MIMICS-1 and the backscattering values measured by the scatterometer.

Temporal response of σ^0

Having established that MIMICS-1 successfully predicts canopy backscatter as a function of angle, the model was run at a constant incidence angle, $\theta = 55°$, while varying the canopy dielectric parameters so as to simulate the variations seen over the three-day diurnal experiment. Figure 11-59 presents the computed backscatter along with the measured values of canopy backscatter for the like- and cross-polarizations. In each case, MIMICS successfully predicts the appropriate level of the measured data together with the decreasing trend in backscatter observed over the three-day period.

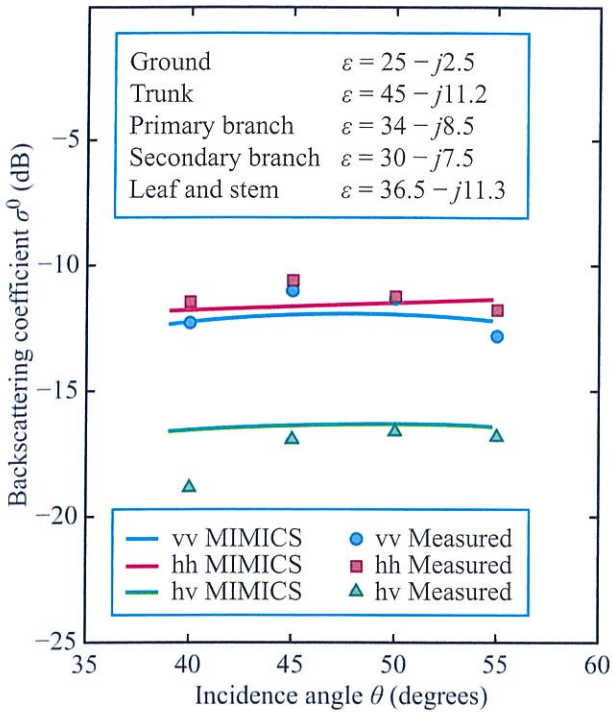

Figure 11-58: Comparison of MIMICS with recorded data for the multiangle data set [McDonald et al., 1991].

Furthermore, MIMICS-1 predicts the 1–2 dB dip seen in σ^0_{vv} and σ^0_{hv} in the early afternoon of each day.

11-12.4 Canopy Biophysical Parameters

Forest canopies are characterized by elaborate architectures that may vary not only by species, but also by age. The most important biophysical parameters of forest canopies include:

- ***Tree height*** $h = h_t + h_c$
- ***Trunk height*** h_t (m)
- ***Crown depth*** h_c (m)
- ***Tree (or stock) density*** N: # of trunks/hectare (ha) or trunks/m^2
- ***Trunk diameter*** d (averaged over the trunk height)

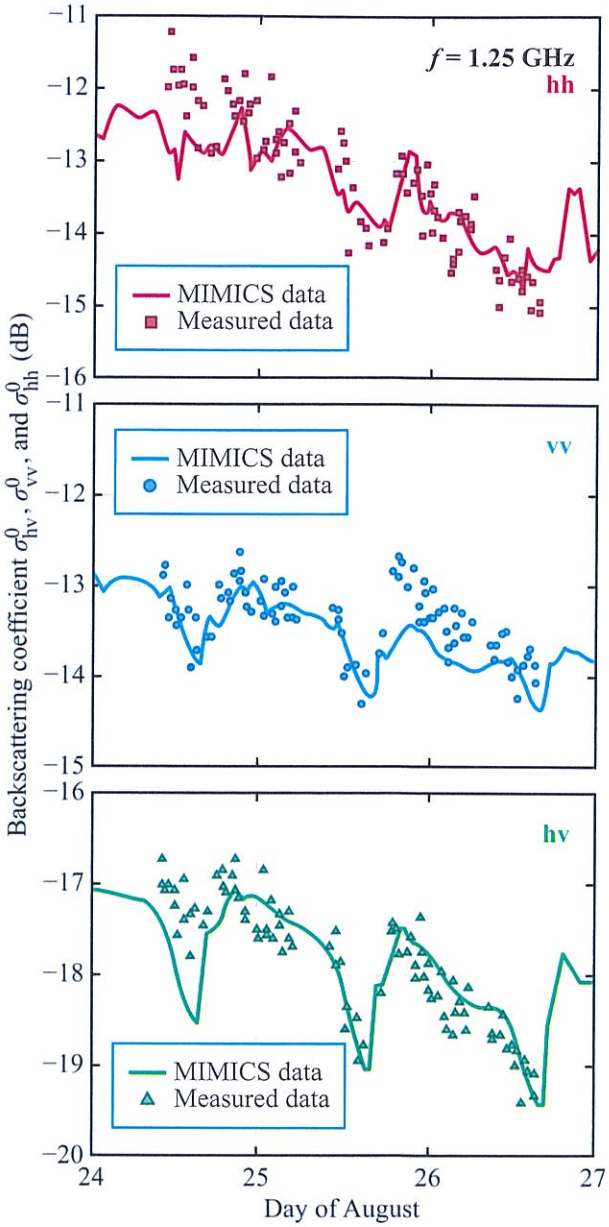

Figure 11-59: Measured and predicted backscatter during three-day diurnal experiment: (a) hh-polarized response, (b) vv-polarized response, (c) hv-polarized response [McDonald et al., 1991].

- ***Trunk (or stem) volume*** $V_t = Nh_t(\pi d^2/4)$, in m^3/m^2 (or m^3/ha where 1 m^3/ha $= 10^{-4}$ m^3/m^2)
- ***Stem (or trunk) biomass*** $B_t = \rho_t V_t$ = trunk *dry* mass per unit area (kg/m^2). Sometimes biomass is expressed in tons per hectare (tons/ha); the conversion factors are 1 ton $= 10^3$ kg and 1 ha $= 10^4$ m^2. Hence, 1 ton/ha $= 0.1$ kg/m^2.
- ***Basal area*** $A_b = V_t/h_t$, in m^2/m^2 or m^2/ha
- ***Crown biomass*** B_c: kg/m^2 of crown section
- ***Above ground standing dry biomass*** $B_d = B_t + B_c$

The term ***stem*** often is used as a generic term for trunk. The canopy architecture describes the size, shape, and orientation distributions of the canopy constituents. A popular model called AMAP is the subject of an excellent article by Castel et al. (2001) in which the authors connect the statistical information provided by AMAP (for many tree species) to the parameters commonly used in radiative transfer models for computing σ^0. Also, for many forest species, empirical ***allometric equations*** have been developed to relate height to diameter of trunks, and those two dimensions to biomass. If height and diameter were perfectly correlated for a given species, then the trunk biomass B_t can be uniquely determined from only the trunk height h_t or its diameter d. This, however, is not always the case; competition, natural disturbance processes, and silvicultural management modify tree density over time. Consequently, B_t does not necessarily vary in a monotonic fashion with either h_t or d.

Figure 11-60 presents a structural classification model for vegetation based on six classes. The distinction between classes is based on the presence or absence of woody stems, and leaf size and shape. Thus, the proposed model was developed from the perspective of how a polarized radar signal is expected to interact with a vegetation canopy (Dobson et al., 1996).

11-12.5 Backscatter Response to Forest Parameters

In this subsection, we explore answers to the following direct and *inverse* questions:

(a) How does σ^0 respond to the biophysical parameters introduced in the preceding subsection?

(b) What radar wave parameters are best suited for estimating tree height and stem and crown biomasses?

The answer to the first question depends not only on the radar wave parameters (incidence angle θ, frequency f, and polarization configuration), but also on the tree species and the degree of spatial uniformity of the canopy. The literature includes two types of reports, one in which σ^0 is plotted against a biophysical parameter of a single species, and another in which multiple tree species are combined together. As we see shortly, plots representing the combination of multiple species exhibit more scatter of the data about the trend lines than single-species data.

Ideally, we may want to develop a radar system that can measure trunk biomass with usable accuracy regardless of tree species. Realistically, however, this is not likely to succeed; the vast diversity of canopy architectures suggests that a more viable approach entails a two-step process:

(1) a land-cover classification step that identifies the species of individual forest parcels, followed by

(2) a biophysical parameter estimation step in which tree species-specific inversion algorithms are used.

Let us briefly examine the expected roles of the incidence angle θ, the frequency f, and receive/transmit polarization configuration pq (with p and q = h or v).

Incidence angle

Because the range resolution of a SAR is proportional to $1/\sin\theta$, it is impractical to operate it at θ smaller than about 20°. By operating at $\theta \geq 20°$, we also avoid the issues associated with the near-nadir steep angular variation of σ^0 of the underlying surface. On the other hand, the transmissivity of the canopy, Υ, decreases with increasing θ because of the longer (slant) pathlength through the canopy. At very large values of θ (such as $\theta > 75°$), the canopy approaches an electromagnetically semi-infinite medium, which may provide a good estimate of the crown biomass, but not of the tree height or trunk biomass. Hence, most

	Herbaceous		Woody			
	Blade-like	Broadleaf	Shrubs	Trees		
Growth form	 (e.g. grass)	 (e.g. soybeans)	 (e.g. alder)	Excurrent  Gymnosperms (e.g. pine)	Decurrent  Angiosperms Dicotyledons (e.g. oak)	Columnar  Angiosperms Monocotyledons (e.g. palm)
Structural characteristics						
Trunks	None	None	Many small trunks with characteristic orientations	Conical trunk with layered dielectric	Cylindrical, forked trunk with layered dielectric	Cylindrical trunk of homogeneous dielectric
Branches	Non-woody stalks or stems	Non-woody stems	Many small branches and stems	Branch size and orientation vary with height	Branches forked with few horizontal elements	None
Foliage	Blade-like erectophile	Broad leaves	Blade-like or broad leaves	Needles	Broad leaves	Blade-like clump at top of trunk

Figure 11-60: Description of simple structural classes of vegetation [Dobson et al., 1996].

imaging radar systems operate within the angular range $20° \leq \theta \leq 60°$.

Frequency

The data reported earlier in Figs. 11-47 and 11-49 indicate that for a forest populated with trees on the order of 10–15 m in height, the two-way transmissivity at L-band is on the order of 10^{-2}. This means that by operating at C-band or a higher frequency, it may be possible to obtain a useful estimate of the biomass contained in the upper part (crown section) of the canopy, but lower-frequency channels are needed to measure trunk biomass.

Polarization

In general, the canopy volume is a much stronger depolarizing medium than is the underlying surface. Consequently, σ^0_{hv} usually exhibits a greater dynamic range as a function of canopy height or biomass than do σ^0_{hh} or σ^0_{vv}.

This behavior is evident in the plots shown in Fig. 11-61 for a forest parcel of jack pine observed by the L-band channel of the SIR-C SAR. Over the indicated range of the canopy biomass B_d, the dynamic range of σ^0_{hv} is about 10 dB, compared with only 5 dB for σ^0_{hh} and 3 dB for σ^0_{vv}.

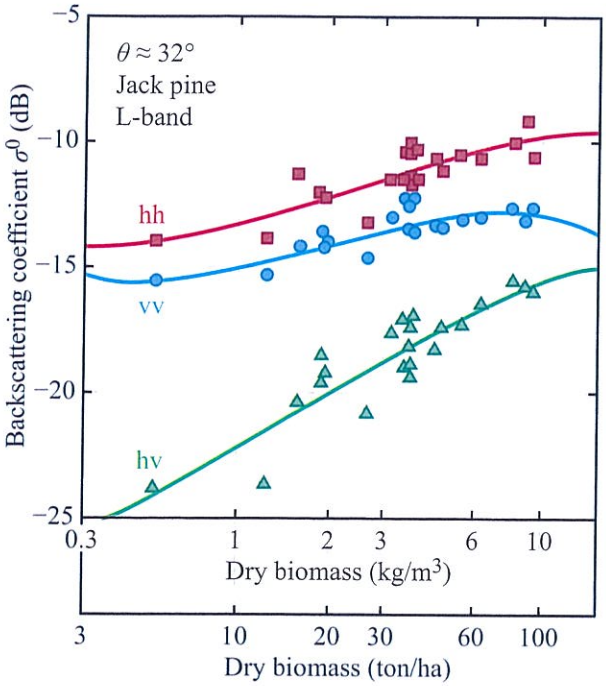

Figure 11-61: SIR-C measured radar response to dry biomass B_d for jack pine canopies. Biomass scale is logarithmic [Dobson et al., 1995a].

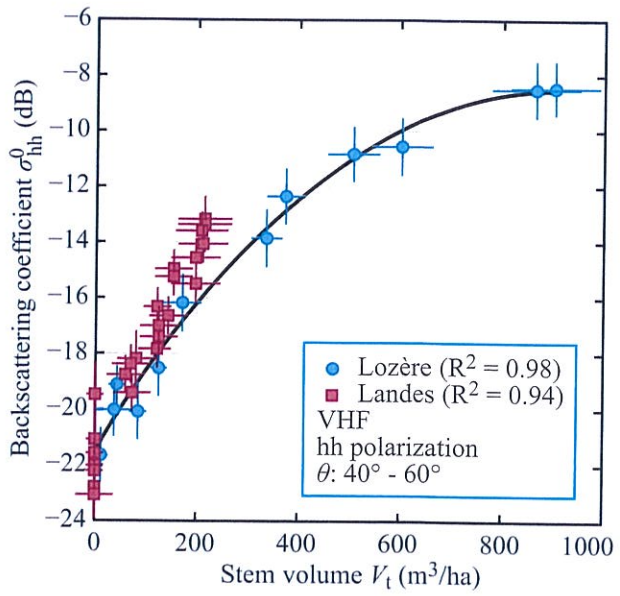

Figure 11-62: VHF backscatter coefficient versus stem volume for two French test sites [Melon et al., 2001].

11-12.6 σ^0 Response at VHF-Band

The CARABAS SAR system—which is an acronym for ***C***oherent ***A***ll-***Ra***dio ***Ba***nd ***S***ensing—is an airborne SAR that operates over the 20–90 MHz range, which is in the lower part of the VHF band. The SAR spatial resolution is on the order of 3 m (Gustavsson et al., 1996). Even though a system at such a low frequency cannot be used from a space platform (because of propagation loss through the ionosphere), it is nevertheless attractive as an airborne imaging system because its long wavelength affords greater penetration through forest canopies.

The CARABAS system was used to image forest test sites in Sweden and France (Manninen and Ulander, 2001; Melon et al., 2001) to determine the response of σ^0 to trunk volume V_t. The results obtained from two French test sites are shown in Fig. 11-62. In both cases, the data exhibit excellent fits to the individual trend lines, primarily because of the special uniformity of the forest parcels. According to the authors of the study (Melon et al., 2001):

> *The Landes forest in southwestern France is almost entirely formed of quasi-uniform large stands of maritime pine* [Pinus pinaster *(Ait.)*] *over sandy terrain and is managed in a consistent fashion which ensures that the canopy is homogeneous. Most of the stands are artificially sown, generally in row[s] of 4 m spacing. The rows follow an east-west direction on the test sites. This flat plantation includes clear-cuts and a range of age classes from seedling to the harvest age of 46 years, corresponding to a maximum stem volume of about 215 m^3/ha.*
>
> *The second test site is the Lozère forest in southern France, [...] Austrian pine stands* (Pinus nigra nigrae) *made of even-aged trees ranging from 0 to 130 years old, [...]*

presenting a very large range of stem volume, up to 900 m^3/ha.

We note that σ^0_{hh} exhibits a dynamic range of about 14 dB between $V_t = 0$ and $V_t = 900$ m^2ha. A similar response was observed for the test site in Sweden.

11-12.7 σ^0 Response at P- and L-Bands

PiSAR is a Japanese airborne, polarimetric, L-band SAR with a 4-look, 2 m resolution. The system was flown over a test site in northern Japan to evaluate its capability as an estimator of forest biomass. The site included stands of conifers and other types of trees. Figure 11-63 displays measured values of σ^0 for hh, vv, and hv polarizations, plotted against three biophysical parameters: the tree height h, the basal area A_b, and the total biomass B_d. The observed dynamic range is about 5 dB for vv polarization, 6 dB for hh polarization, and 7.5 dB for hv polarization. For all polarizations, the general trend of σ^0 as a function of canopy biomass consists of a monotonic increase up to about 100 ton/ha (or equivalently, 10 kg/m^2), followed by a leveling off to a saturation level characteristic of a *semi-infinite* canopy. The scatter around the general trend is attributed, in part, to the different tree species.

Similar results are evident in Fig. 11-64, which displays σ^0 as a function of canopy biomass B_d at L-band and P-band. As expected, the P-band response exhibits a wider dynamic range and a higher saturation level. However, because of the large amount of data scatter around the trend line, it is difficult to quantitatively ascertain the dynamic range of B_d that can be estimated by the radar. The data scatter is attributed to the wide variety of trees and shrubs imaged by the NASA AIRSAR system.

The E-SAR system is a dual-frequency (P- and L-band) airborne system operated by the German Aerospace Center (DLR). The center frequencies of its P- and L-band signals are 340 MHz and 1.3 GHz, respectively. Based on imagery acquired by E-SAR for a test site in the south of Sweden, Sandberg et al. (2011) generated the results shown in Fig. 11-65, which encompass a total of 68 forest stands. The primary tree species were Norway spruce, Scots pine, and birch. To remove most of the angular dependence on θ, the backscattering coefficient σ^0 was converted to $\gamma = \sigma^0/\cos\theta$. The dynamic range of γ is highest for hh polarization at P-band ($\approx$ 12 dB) and smallest for vv polarization at L-band ($\approx$ 2.5 dB). The latter is not surprising, but the former is; in all other studies, σ^0_{hv} (or γ_{hv}) exhibited a wider dynamic range than did σ^0_{hh} (or γ_{hh}).

Given the 6-channel data (3 polarization $\times$ 2 frequencies), the authors of the study (Sandberg et al., 2011) attempted to develop inversion algorithms to estimate the canopy biomass B_d from the measured values of γ. Their best results, shown in Fig. 11-66, use a combination of γ_{hv} and γ_{hh}, both at P-band. The correlation coefficient associated with their regression model is $R^2 \approx 0.8$.

11-13 SIR-C/X-SAR Case Study

The SIR-C/X-SAR, which flew onboard of the Space Shuttle in April of 1994, consisted of three radar instruments: fully polarimetric SARs at L- and C-band and a single-polarization vv-channel at X-band. As such, SIR/C/X-SAR provided a unique opportunity to image terrestrial surfaces at three different microwave frequencies. In preparation for the Space Shuttle mission, the Radar Remote Sensing team at the University of Michigan selected a test site at the eastern end of the Upper Peninsula of Michigan, located near Raco, Michigan. Over a three-year period, the Michigan team conducted a comprehensive survey of the approximately 40 km $\times$ 24 km Raco supersite. This section presents a summary of their observations and conclusions (Dobson et al., 1995).

11-13.1 Raco Supersite Description

The site contained many boreal forest species and several temperate species. Homogeneous forest stands usually exceed 10 ha in size. The SIR-C/X-SAR images were processed to 25 m $\times$ 25 pixels (each representing approximately 7.7 looks at L- and C-bands and 6.5 looks at X-band). A 10-ha stand is equivalent to an area

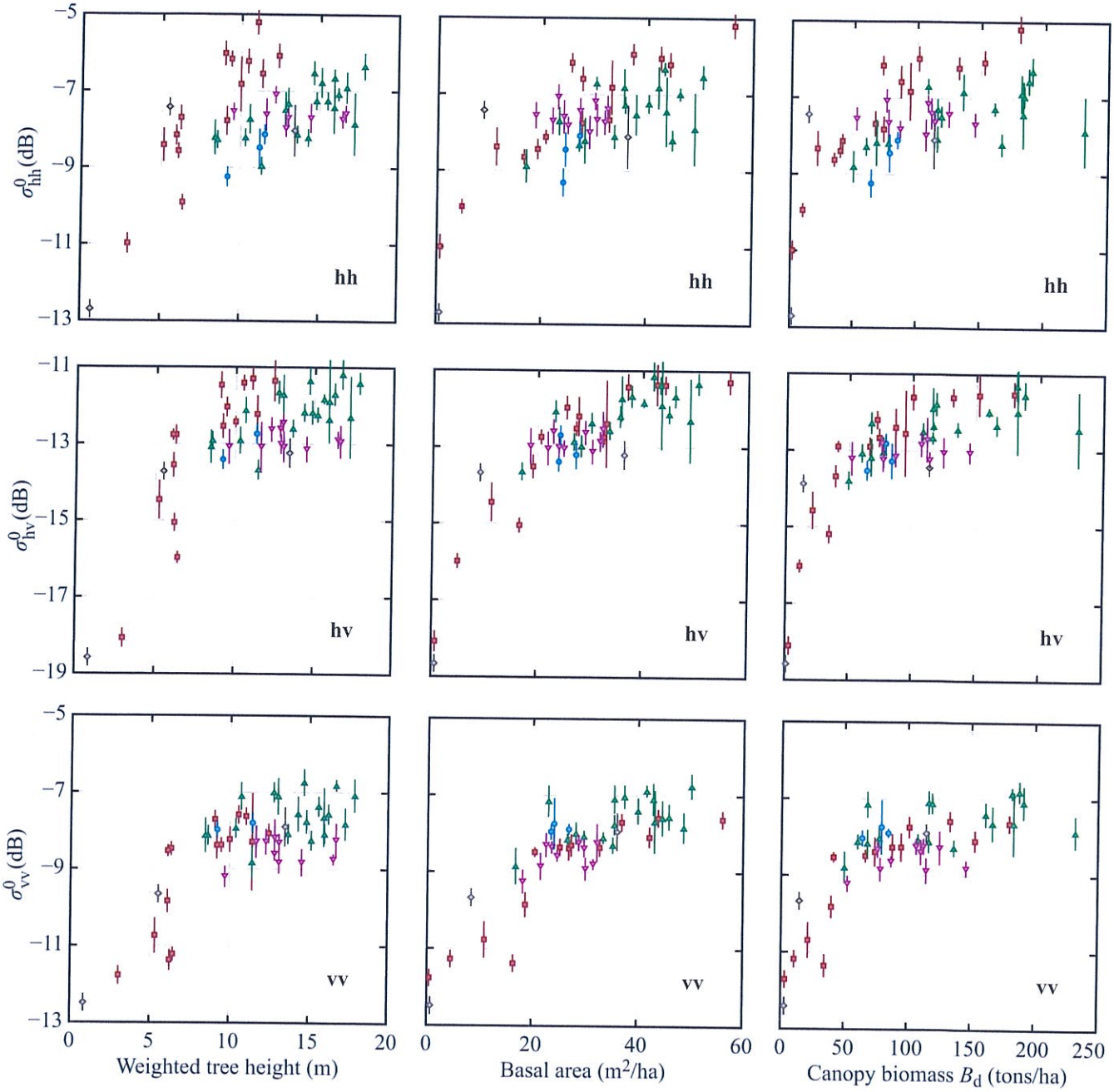

Figure 11-63: Measured L-band backscattering coefficient as a function of tree height, basal area, and canopy dry biomass. Colors represent different tree species, range of incidence angle is 43°–48° [Watanabe et al., 2006].

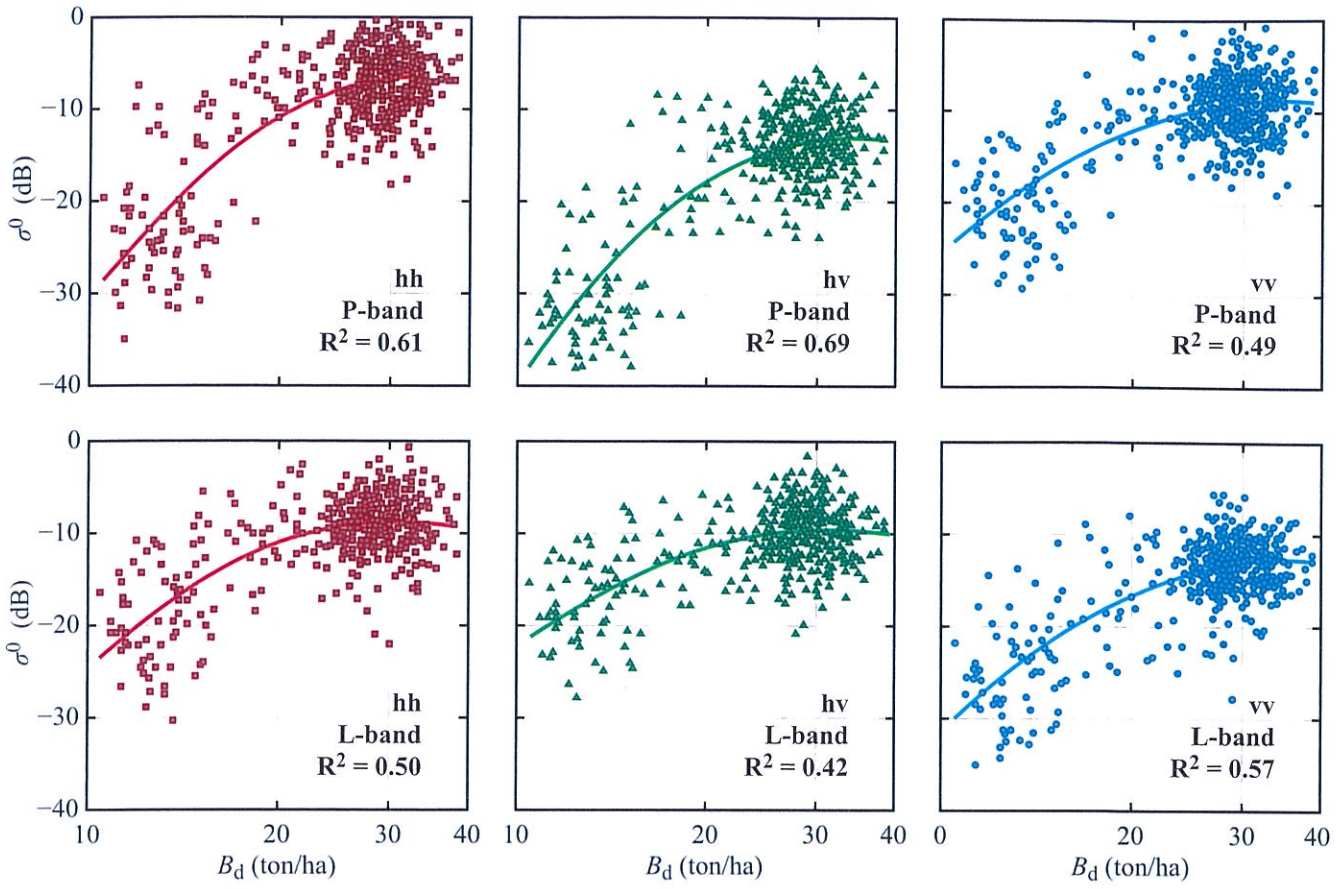

Figure 11-64: Backscattering coefficient at P- and L-band versus B_d with B_d on a log scale. Incidence angle range is 26°–63° [Saatchi et al., 2007].

1000 m × 100 m, which would contain $40 \times 4 = 160$ image pixels.

The forest communities included:

(a) Upland Conifers: they have an ***excurrent architecture*** (see Fig. 11-60) with large branches and long needles, and they include jack pine, red pine, and eastern pine.

(b) Lowland Conifer: they have excurrent architecture with small branches and short needles, and they include black spruce, white spruce, northern white cedar and tamarack.

(c) Northern Hardwoods: they have a ***decurrent architecture*** (see Fig. 11-60) with large branches, and they include sugar maple, red maple, American beech, eastern hemlock, and balsam fir.

(d) Lowland Hardwoods: they have a decurrent architecture with small branches, and they include red maple, white birch, yellow birch, and trembling aspen.

In addition to the preceding four forest categories, the test site included permanent clearings, hayfields, and a large agricultural region in the southeastern portion of

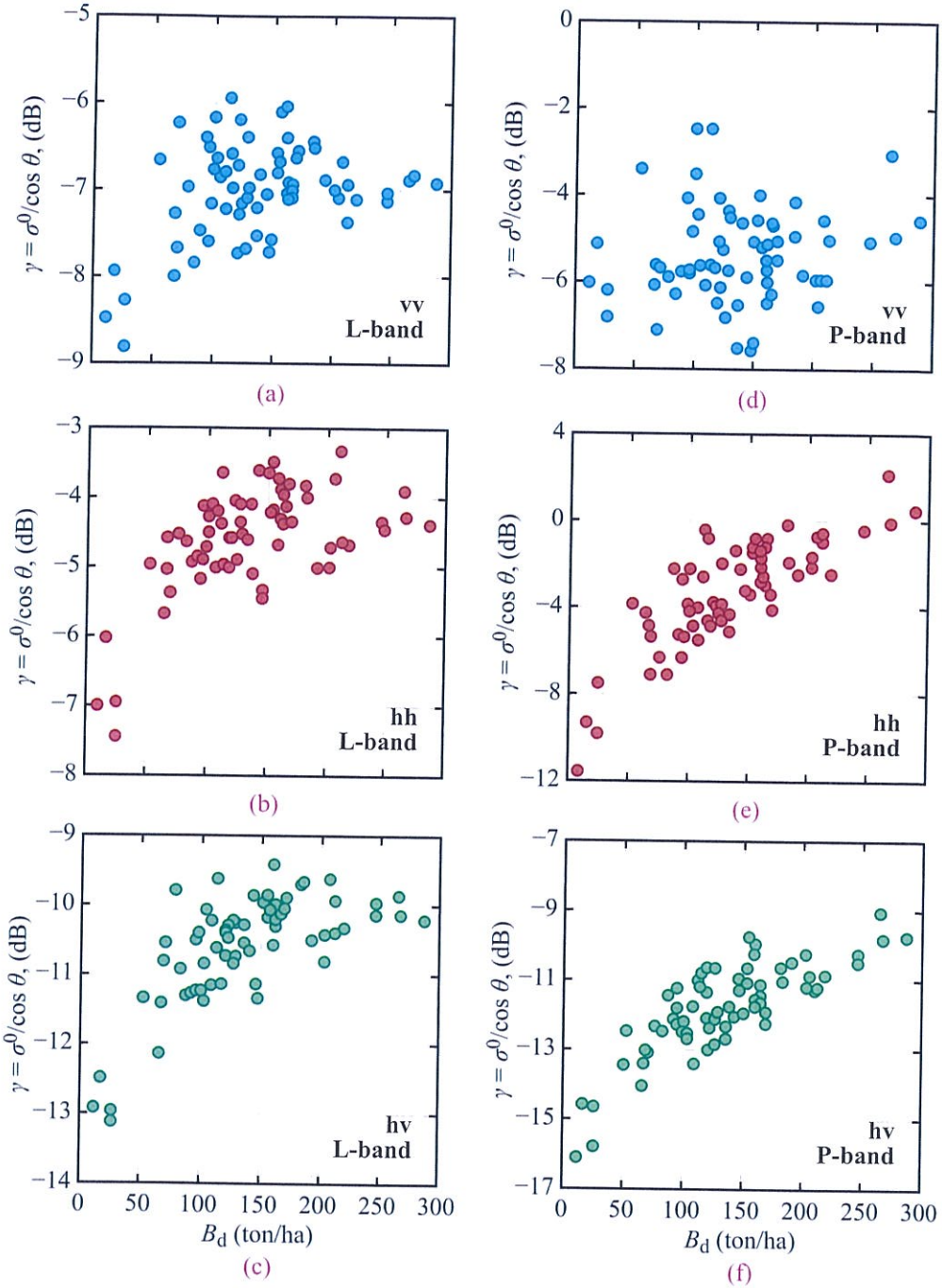

Figure 11-65: Measured backscattering coefficient of forest canopies at L- and P-band, plotted versus dry biomass B_d. Angular range is 28°–50° [Sandberg et al., 2011].

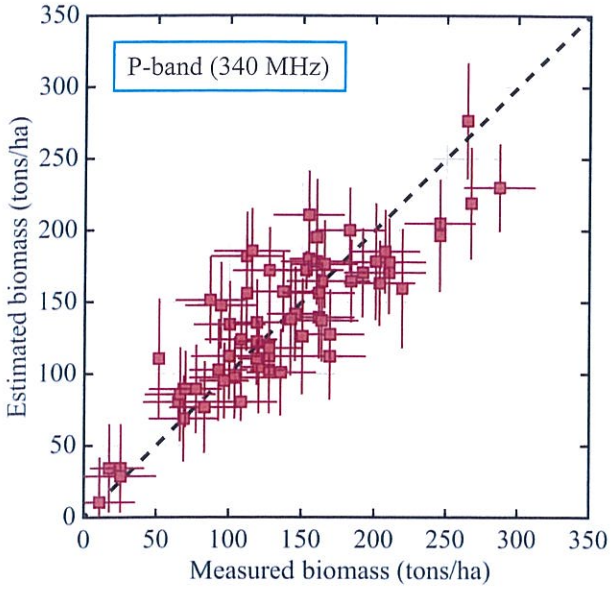

Figure 11-66: Result of biomass estimation using P-band data from 2 May 2007 based on the multipolarized regression model

$$B_d = [\beta_0 + \beta_1 \gamma_{hv}\,(\text{dB}) + \beta_2 \gamma_{hh}\,(\text{dB})]^2,$$

where β_0, β_1, and β_2 are empirically determined constants [Sandberg et al., 2011].

the site. These nonforested areas were designated as either:

(e) Short vegetation, or

(f) Surfaces.

A stratified sample of each of the primary forest communities was selected for biometric survey. A total of over 60 forest stands were selected, each covering an area of 200 m × 200 m. Using GPS with 3-D differential processing, multiple transects were selected within each sampled area to characterize the upper stratum (height > 5 m), the middle stratum ($1 \text{ m} < h < 5$ m) and the lower stratum ($h < 1$ m). The diameters of all live and dead stems were recorded by species to the nearest 0.1 cm. Numerous other measurements were performed including trunk diameter, trunk biomass, trunk density, crown biomass, etc. The total number of trees so sampled was on the order of 64,000!!

11-13.2 Land-Cover Classification

The block diagram in Fig. 11-67 depicts the processing steps applied to each channel of the SAR data. Following full calibration of the SAR images, a digital elevation model is used to mask areas where layover or shadow prohibit analysis. This is part of the ***image segmentation*** step in Fig. 11-67. The remainder of the scene is classified in a three-level hierarchical manner:

(a) ***Level 1***: The goal of the first SAR classifier, which was developed using training data of known classes, is used to differentiate the scene into four general structural classes: urban, surfaces, short vegetation, and tall vegetation (forest).

(b) ***Level 2***: The Level-1 tall vegetation class is further subdivided into subcategories on the basis of the structural characteristics of the vegetation.

(c) ***Level 3***: Following classification into the four forest classes, class-specific inversion algorithms are used to estimate the biophysical properties of the forest canopies.

To reduce the effects of image speckle, all images were post-processed using a 5×5 averaging window, thereby increasing the number of looks from ≈ 7.7 to ≈ 200 at L- and C-bands, and from ≈ 6.5 to ≈ 160 at X-band. The three-level classification algorithms were performed on the post-processed images.

The image shown in Fig. 11-68(a) is a false-color composite of the Raco supersite; the primary colors are assigned as follows: red = L-band hv-pol, green = C-band hv-pol, and blue = X-band vv-pol. The intent of the color composite is to demonstrate that multipolarized radar observations contain a great deal more information about the imaged terrain than the intensity of a single-polarized channel.

The Level-2 classification results are presented in Table 11-3 and displayed in the image shown in Fig. 11-68(b). The average classification accuracy is 94%.

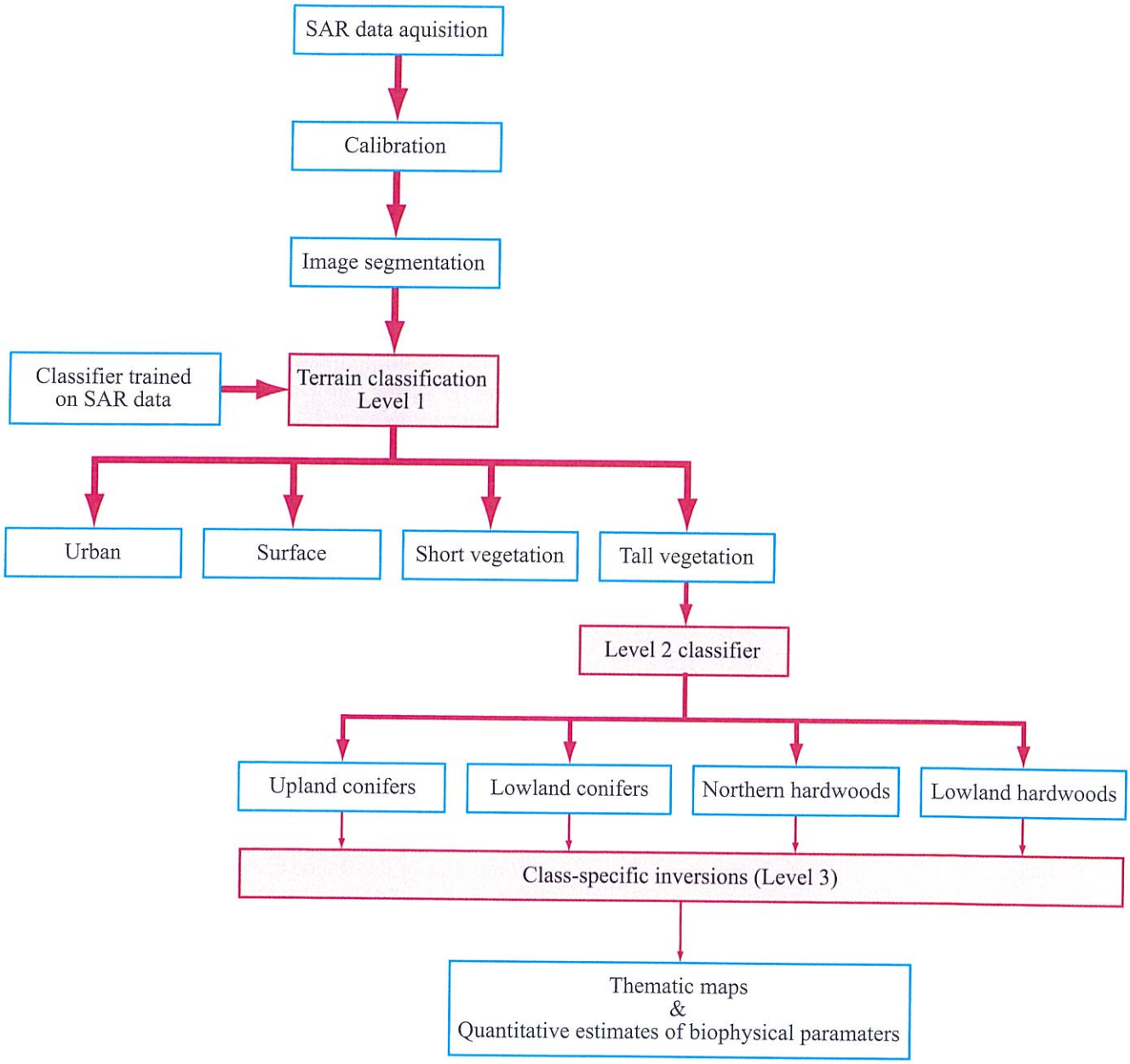

Figure 11-67: Three-level classifier for landcover classification and biophysical parameter estimation [Dobson et al., 1995b].

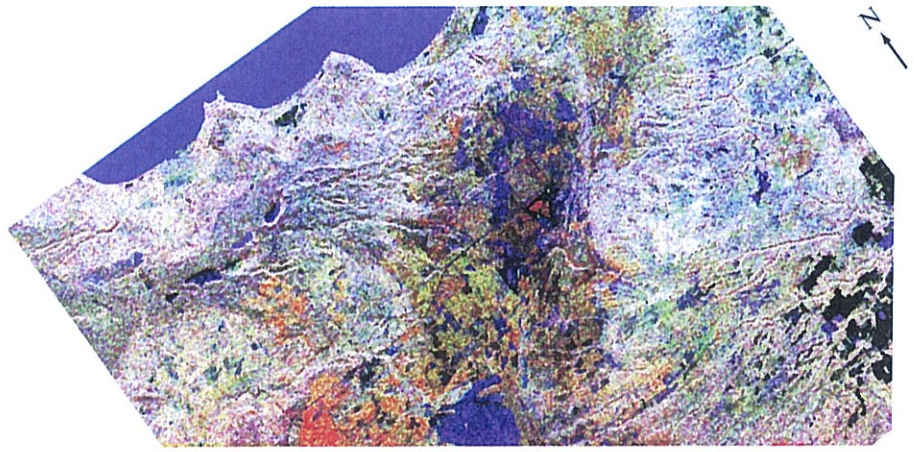

(a) Composite SIR-C / X-SAR image

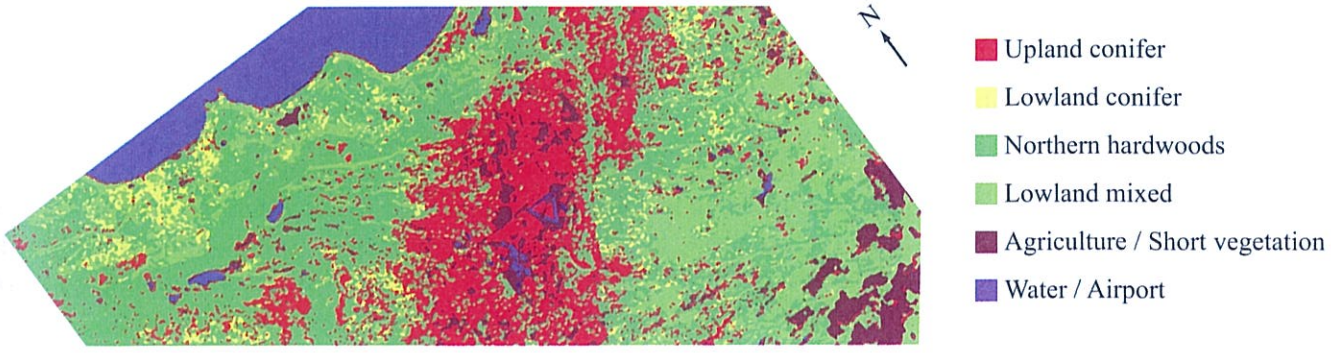

(b) Classified image

Figure 11-68: (a) Composite SIR-C/X-SAR image. Data take 22.2, SRL-2, 1 October 1994. Incidence angle = 22.2°; red, L-band hv; green, C-band hv; blue, X-band vv, (b) Classified image [Dobson et al., 1995b].

11-13.3 Estimation of Forest Biophysical Parameters

In order to decouple the errors associated with the biophysical retrievals of Level-3 from those associated with the Level-2 classifier, only those pixels that were correctly classified by the Level-2 classifier were subjected to the inversion algorithms. Each co-registered post-processed image pixel is represented by a vector of length 9, of which 7 represent the image intensities at X-band (vv polarization) and three each at L- and C-bands (vv, hh, and hv polarizations), and the remaining 2 represent the co-polarized phase differences at L- and C-bands. Using a variety of empirically generated algorithms that utilize various combinations of the 9 elements of the image pixels, Dobson et al. (1995b) were able to develop estimators for tree height h, basal area A_b, trunk biomass B_t, crown biomass B_c, and total biomass B_d, for each of five different forest communities, and to do so with a high degree of accuracy. The results are displayed in

Table 11-3: Level-2 classification results [Dobson et al., 1995b].

			PERCENT CLASSIFIED AS (independent test region)					
	Structural class	Type	Tall vegetation				Short vegetation	Surface
		Tree form	Excurrent		Decurrent		NA	NA
		Branch size	Large	Small	Large	Small		
		Foliage type	Long-needle	Short-needle	None	None		
	Local floristic community		Upland conifers	Lowland conifers	Northern hardwoods	Lowland hardwoods	Grasses, sedges, shrubs	Bare soil, paved, water
TRUE CLASS	Upland conifers		94.53	0.01	5.38	0	0.08	0
	Lowland conifers		4.53	92.88	2.41	0.11	0.07	0
	Northern hardwoods		0.87	7.81	90.30	1.02	0	0
	Lowland hardwoods		0	5.49	6.11	88.40	0	0
	Short vegetation		0.85	0.01	1.41	0.02	96.38	1.33
	Surface		0	0	0	0	1.05	98.95

Figs. 11-69 and 11-70. The indicated vertical error bars represent ± 1 standard deviation of the "ground-truth" in-situ measurements, and the horizontal error bars represent the ± 1 standard deviation of SAR-related uncertainties, which include co-registration errors of the SAR images and calibration errors. The excellent agreement between the *in-situ* measured values and the SAR-estimated values is a testimonial for why the world needs to have multifrequency polarimetric SAR systems orbiting the earth on a continuing basis.

Finally, by way of illustrating the type of information products that such as a system is capable of generating, we show in Fig. 11-71 images displaying:

(a) Total above-ground biomass B_d.

(b) Below-ground biomass contained in the root system, estimated using allometric relations (Bergen et al., 1998).

(c) Total above- and below-ground biomass.

11-14 Propagation Properties of Snow

A layer of dry snow is a dielectric medium consisting of ***ice crystals*** in an ***air background***. Wet snow is somewhat more complicated, as we see later in this section. Assuming that the ice particles in snow are spherical, the ***absorption***, ***scattering***, and ***extinction*** cross section of each ice particle (Q_a, Q_s, and $Q_e = Q_a + Q_s$), respectively) may be calculated in terms of the particle radius r and the relative dielectric constant ε_i using the ***Mie expressions*** given in Section 8-5.2.[†] Actually, the expressions are formulated in terms of the parameters

$$\chi = k_b r = \frac{2\pi r}{\lambda_b} = \frac{2\pi r}{\lambda_0}\sqrt{\varepsilon_b'} \tag{11.100a}$$

and

$$n = \frac{n_i}{n_b} = \left(\frac{\varepsilon_i}{\varepsilon_b}\right)^{1/2} = \varepsilon^{1/2}, \tag{11.100b}$$

where k_b is the wave number in the background medium; ε_b' is the relative permittivity of the background medium; n_i, n_b, and n are the complex indices of refraction of the particle (ice), the background medium, and the particle relative to the background medium, respectively; and ε_i, ε_b, and ε, are the corresponding complex dielectric constants. In the case of dry snow, the background is air; hence $\varepsilon_b' = 1$ and $\varepsilon = \varepsilon_i$.

For reasons that will become clear later, scattering in both dry and wet snow is attributed to the ice particles

[†] **Computer Codes 11.3 and 11.4.**

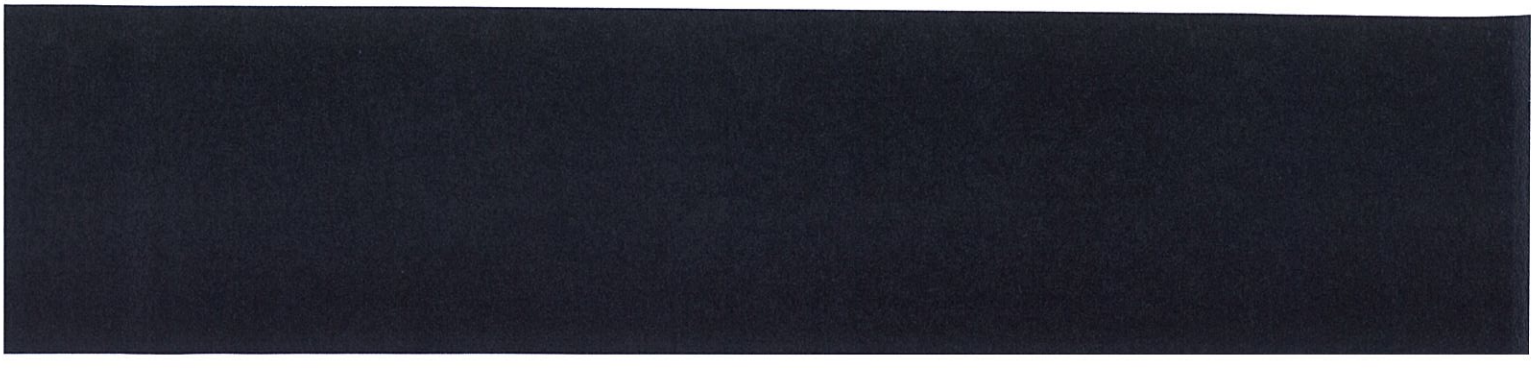

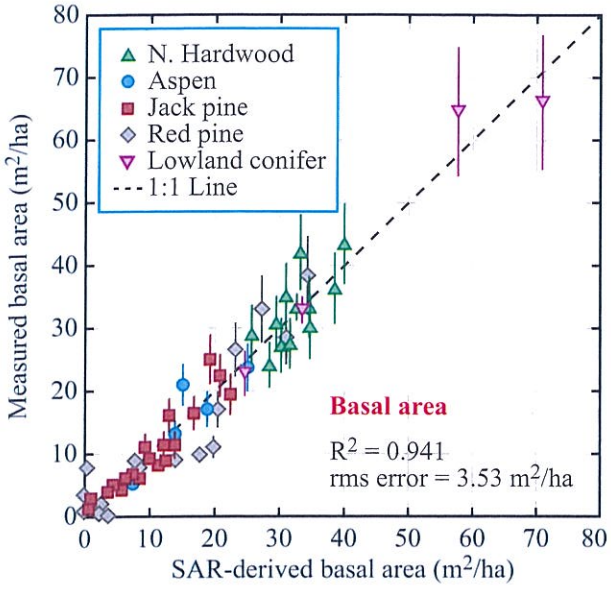

(a) Basal area

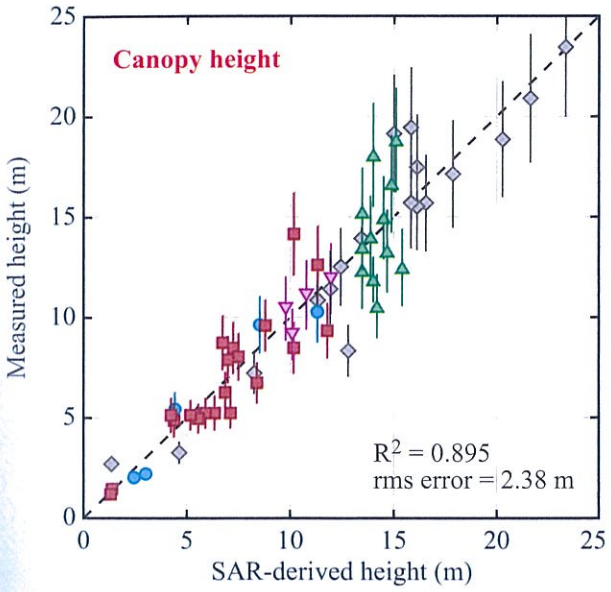

(b) Canopy height

Figure 11-69: *in-situ* measured basal area and tree height versus SAR-derived values based on SIR-C/X-SAR measurements [Dobson et al., 1995b].

in the snow. Ignoring the mutual interaction between the ice particles, κ_s is the sum of the scattering cross sections of all ice spheres contained in a unit volume:

$$\kappa_s = \sum_{j=1}^{N_v} Q_s(r_j, n), \tag{11.101}$$

where N_v is the number density of ice spheres in m^{-3}.

In the general case, the absorption coefficient κ_a consists of two components,

$$\kappa_a = \kappa_{ai} + \kappa_{ab}, \tag{11.102}$$

where κ_{ai} accounts for absorption by the ***ice spheres*** and κ_{ab} accounts for absorption by the ***background***. These quantities are given by

$$\kappa_{ai} = \sum_{j=1}^{N_v} Q_a(r_j, n), \tag{11.103}$$

and

$$\kappa_{ab} = 2k_0(1 - v_i)n_b'' = 2k_0(1 - v_i)\left|\Im\mathrm{m}\{\sqrt{\varepsilon_b}\}\right|, \tag{11.104}$$

where $k_0 = 2\pi/\lambda_0$ and v_i is the volume fraction of ice particles in the mixture. For dry snow, the background is air, and $n_b'' = 0$. Hence, $\kappa_{ab} = 0$ and $\kappa_a = \kappa_{ai}$. For wet snow, the background is taken to be the air-water mixture (as discussed later). Hence, $n_b'' \neq 0$.

If $\varepsilon_b''/\varepsilon_b' \ll 1$, which is the case for low values of the liquid-water content m_v, κ_{ab} can be calculated using an approximate form of Eq. (11.104), namely,

$$\kappa_{ab} \approx k_0(1 - v_i)\frac{\varepsilon_b''}{\sqrt{\varepsilon_b'}}. \tag{11.105}$$

For a given ***drop-size distribution*** $p(r)$, κ_{ai} and κ_s may be obtained by evaluating the integral in the expression

$$\kappa = \int_0^\infty p(r)\, Q(r,n)\, dr, \tag{11.106}$$

where κ is κ_{ai} or κ_{si} corresponding to Q_a or Q_s, respectively. The units of $p(r)$ are drops per m^3 per unit increment of drop radius r. If the drop-size distribution

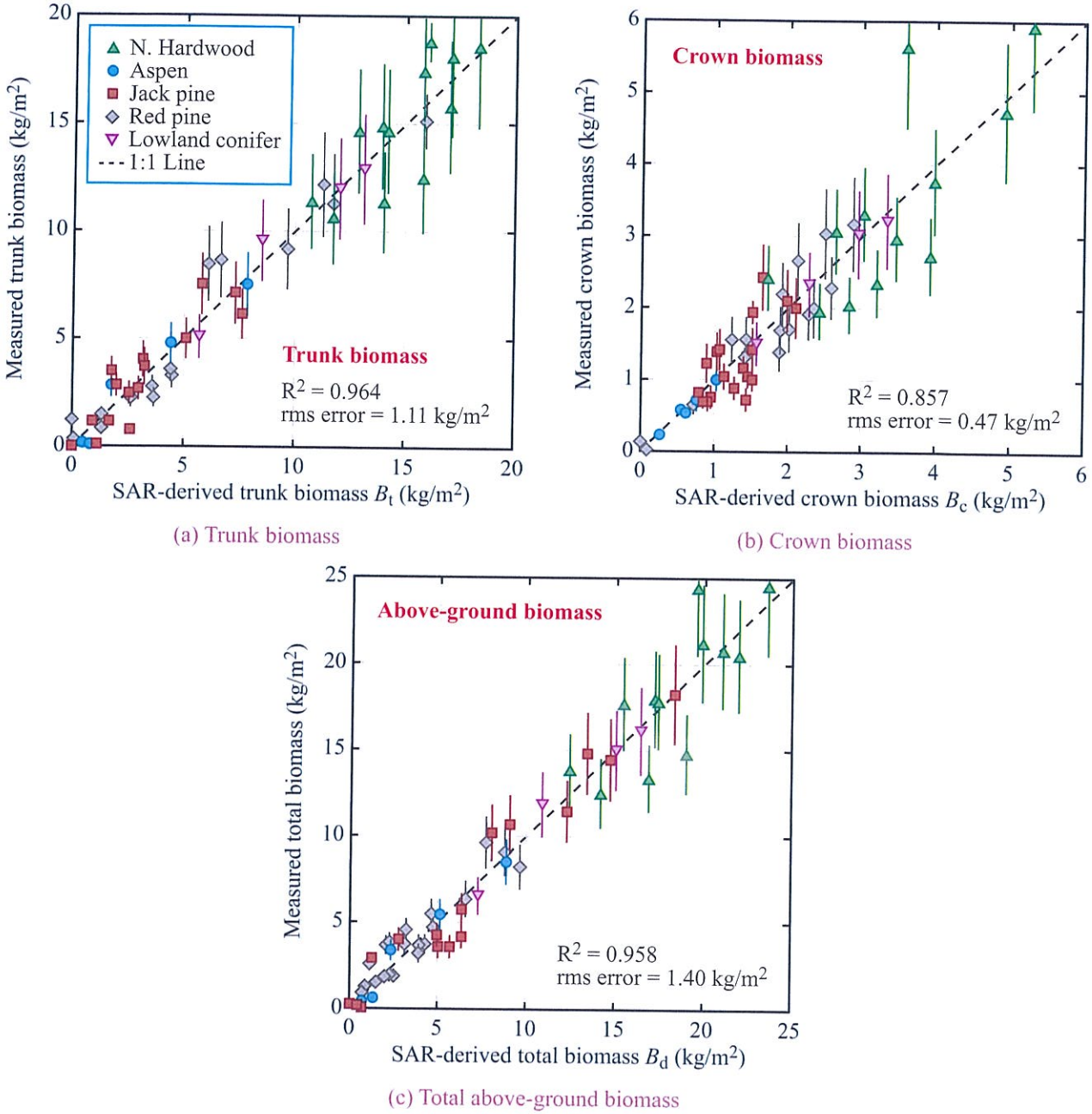

(a) Trunk biomass

(b) Crown biomass

(c) Total above-ground biomass

Figure 11-70: Measured *in-situ* versus SAR-derived values for (a) trunk biomass, (b) crown biomass, and (c) total above-ground biomass [Dobson et al., 1995b].

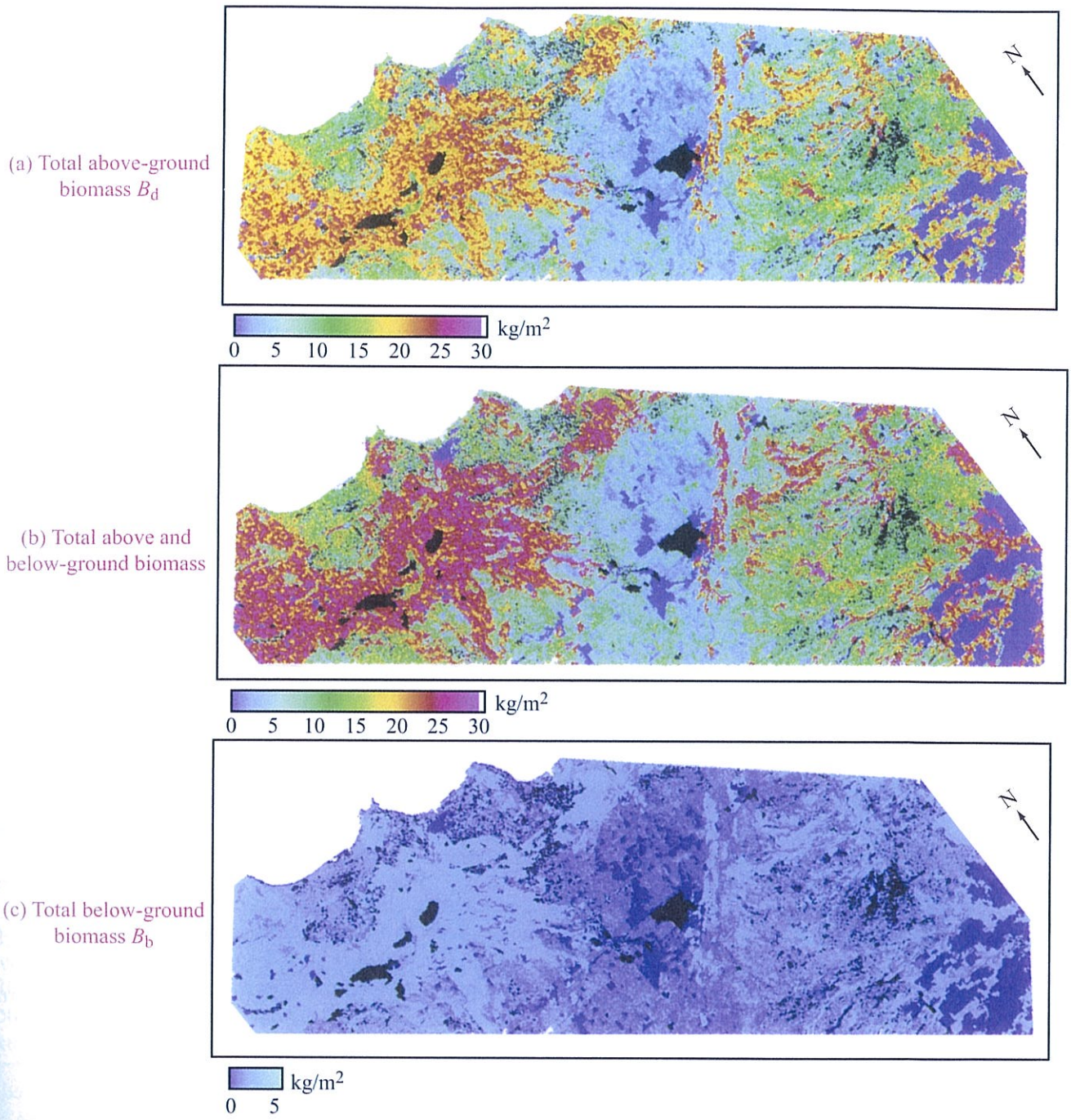

Figure 11-71: False-color images depicting the distribution of above-ground biomass, below-ground biomass, and total biomass for the Raco supersite [Dobson et al. (1995b) and Bergen et al. (1998)].

is equal to zero for r larger than some radius r_{max}, and if the wavelength λ_b ($= \lambda_0$ for dry snow) is such that $\chi_{max} = 2\pi r_{max}/\lambda_b \leq 0.3$, the Mie expressions for the cross sections Q_a and Q_s reduce to the Rayleigh expressions given in Section 8-5.3. This not only simplifies the computation of all quantities concerned, but also leads to an expression for κ_{ai} that is independent of $p(r)$. The ***Rayleigh*** expression for $Q_a(r_i,n)$ for an ice particle of radius r_i is

$$Q_a(r_i,n) = \frac{8\pi^2}{\lambda_b} r_i^3 \, \mathrm{Im}\{-K\}, \tag{11.107}$$

where K is a complex quantity defined by Eq. (8.43) in terms of the particle-to-background index of refraction n,

$$K = \frac{n^2-1}{n^2+2} = \frac{\varepsilon-1}{\varepsilon+2}. \tag{11.108}$$

Inserting Eq. (11.107) into the discrete form for κ_{ai} given by Eq. (11.103) leads to

$$\kappa_{ai} = \frac{8\pi^2}{\lambda_b} \mathrm{Im}\{-K\} \sum_{j=1}^{N} r_j^3. \tag{11.109}$$

The density of dry snow ρ_s (g/cm^3) is equal to the volume fraction occupied by the ice particles, v_i, multiplied by the ***density of ice*** ($\rho_i = 0.9167$ g/cm^3),

$$\rho_s = \rho_i \sum_{j=1}^{N_v} \frac{4\pi}{3} r_j^3. \tag{11.110}$$

Incorporating Eq. (11.110) into Eq. (11.109) leads to

$$\kappa_{ai} = \frac{6\pi}{\lambda_b} \frac{\rho_s}{\rho_i} \mathrm{Im}\{-K\}. \tag{11.111}$$

(Rayleigh approximation)

The absorption and scattering coefficients are model parameters used in the radiative transfer equation to compute the scattering and emission of a layer of snow. When such computations are performed, often $p(r)$ is not known for the snow layer under consideration; however, it may be possible to estimate the mean or typical particle radius instead. If this typical radius is r, and all the particles are assumed to be of this size,

$$\kappa(r) = N_v(r)\, Q(r,n) \tag{11.112}$$

for κ_{ai} and κ_{si} (corresponding to Q_a and Q_s), and the number density $N(r)$ is determined from the density ρ_s by

$$N_v(r) = \frac{\rho_s}{\rho_i} \cdot \left(\frac{4}{3}\pi r^3\right)^{-1} = \frac{v_i}{V_i(r)}, \tag{11.113}$$

where $v_i = \rho_s/\rho_i$ is the ***volume fraction*** of ice in dry snow, and $V_i(r)$ is the volume of a single ice particle of radius r.

▶ If the Rayleigh approximation is appropriate, we use Eq. (11.107) for $Q(r,n)$, but if the particle radius r is too large to satisfy the condition $|n\chi| < 0.5$ [where n and χ are as defined by Eq. (8.31)], then the Mie solution is called for, in which case $Q = (\pi r^2)\xi$, and ξ is as given in Section 8-5.2. ◀

11-14.1 Dry Snow

The dielectric properties of ice are presented in Section 4-3. The real part ε_i' is independent of temperature and frequency (in the microwave region) and is equal to $\varepsilon_i' \approx 3.18$. The dielectric loss factor ε_i'' is a function of both temperature and frequency, and its variation is given in Fig. 4-3. With $n_b = 1.0$, the only additional parameters to be specified for calculating κ_{ai} and κ_s [using Eqs. (11.103) and (11.101)] are the snow density ρ_s, the frequency f, and the particle radius r.

Figure 11-72 shows spectral plots of κ_s, κ_a, and κ_e for a dry snow medium containing spherical ice crystals with $r = 0.5$ mm. All computations were performed using Mie expressions.

▶ Below about 5 GHz $\kappa_s \ll \kappa_a$, and the albedo $a = \kappa_s/(\kappa_s + \kappa_a)$ is very small. On the other hand, at frequencies above 20 GHz, scattering becomes the dominant component of the total extinction loss of the dry snow medium. ◀

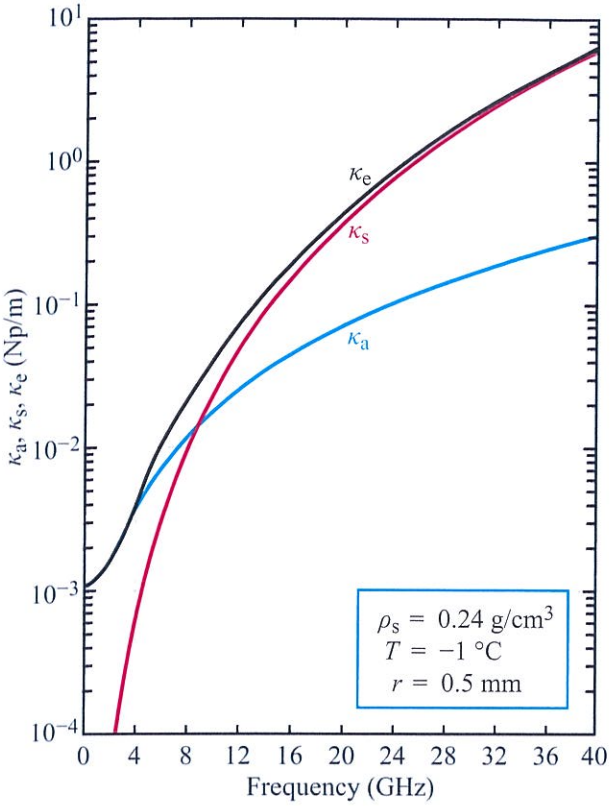

Figure 11-72: Mie-computed absorption, scattering and extinction coefficients for dry snow containing 1 mm diameter ice spheres, plotted as a function of frequency.†

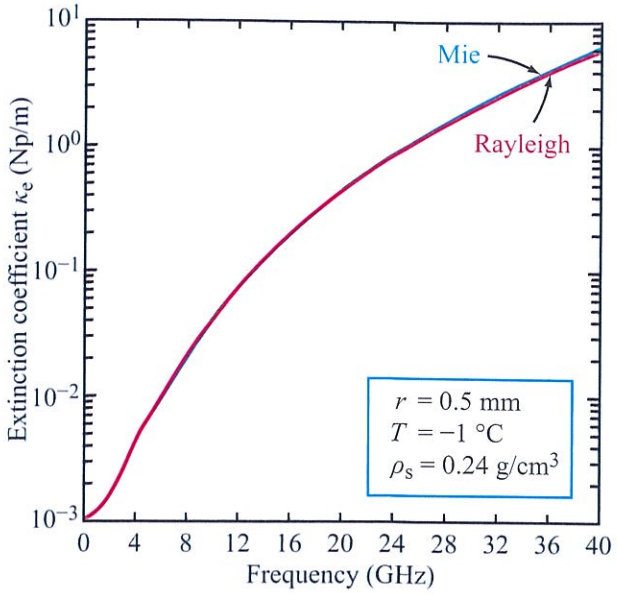

Figure 11-73: Comparison of the Rayleigh approximation with the Mie computation for κ_e of dry snow.

The variation of the extinction coefficient κ_e with the microwave frequency f is illustrated in Fig. 11-73 for snow containing ice particles with $r = 0.5$ mm. The Mie and Rayleigh plots are almost identical across the complete frequency range shown in the figure, which extends to 40 GHz.

▶ Based on this and similar comparisons performed for larger particles, the Rayleigh approximation for κ_e is valid up to 40 GHz for particles as large as 2 mm in radius. For much larger particles with $r = 5$ mm, the Rayleigh approximation provides reasonably accurate results up to 15 GHz. ◀

Plots of the penetration depth δ_p are displayed in Fig. 11-74 for ice particles with $r = 0.5$ mm, 2 mm, and 5 mm. All computations were performed using Mie expressions. We note that δ_p may vary from a few centimeters to tens of meters depending on the particle size and the microwave frequency.

Of course, the snow density ρ_s is important also, since it defines the numerical density of the particles in the snow medium. The plots in Fig. 11-75 indicate that at 37 GHz, κ_s, κ_a, and κ_e vary linearly with ρ_s for $r = 0.5$ mm.

The scattering albedo a of the medium is one of the key parameters determining snow scattering and emission. It is governed by the ice-particle size relative

†Computer Code 11.3.

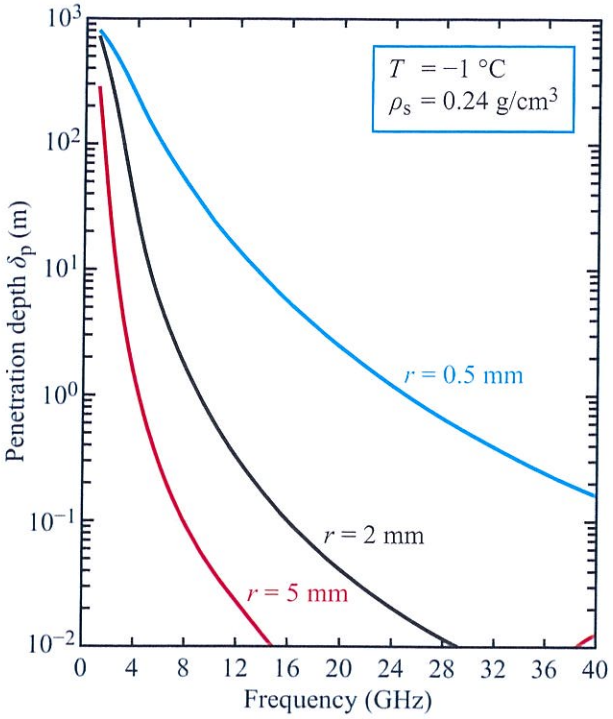

Figure 11-74: Mie calculated microwave spectra of the penetration depth of dry snow.

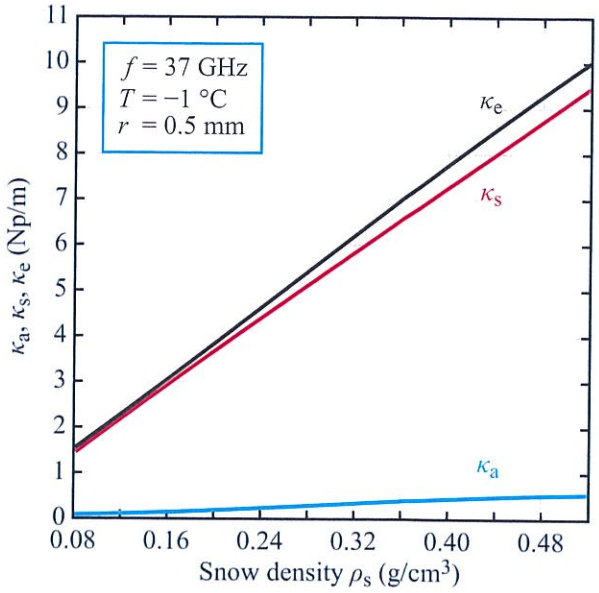

Figure 11-75: Mie-computed dependence of κ_a, κ_s, and κ_e on ρ_s for dry snow at 37 GHz.†

to λ. Plots of a as a function of the frequency f are shown in Fig. 11-76 for three sizes of particle radius. The albedo increases rapidly with increasing frequency f for frequencies corresponding to the size parameter $\chi < 0.5$, and at a slower rate for larger values of χ.

11-14.2 Wet Snow

When water in liquid form is present in snow, the snow medium becomes a mixture of ice particles, water droplets, and air. The volumetric water content of snow, m_v, which also is called ***snow wetness***, usually does not exceed a few percent, and the water droplets usually are much smaller than the ice particles.

▶ Hence, we assume that scattering in the medium is caused mainly by the ice particles, and that the background medium may be regarded as a mixture of water droplets and air. ◀

Assuming that the water droplets are randomly oriented ellipsoids of dielectric constant ε_w and that the host material is air, the dielectric constant of the background mixture (air-water) is, from Eq. (4.27), given by

$$\varepsilon_b = 1 + \frac{m_v}{3}(\varepsilon_w - 1) \sum_{u=a,b,c} \left[\frac{1}{1 + A_u \left(\frac{\varepsilon_w}{\varepsilon_b} - 1 \right)} \right], \tag{11.114}$$

where A_a, A_b, and A_c are the three ***depolarization factors*** of the ellipsoidal water droplet. Complete expressions for ε_w are given in Section 4-1, and according to the study reported by Ambach and Denoth

†**Computer Code 11.3.**

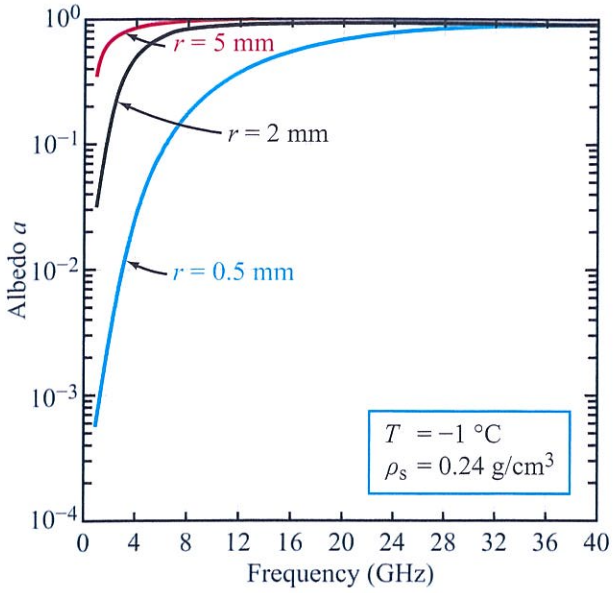

Figure 11-76: Calculated spectral variation of the albedo a of dry snow for three sizes of Mie spheres.

(1980), appropriate values one might assign to the depolarization factors are $A_c = 0.88$ and $A_a = A_b = 0.06$. With these parameters specified, it should be easy to solve Eq. (11.114) to determine the background dielectric constant ε_b for any value of the snow wetness m_v (note that ε_b appears on both sides of Eq. (11.114)).

Calculating κ_{ai} and κ_{si} for wet snow involves using the same expressions as for dry snow, except that ε_b in Eq. (11.100) is no longer equal to 1.0. In addition, we must use Eq. (11.104) to calculate the absorption coefficient of the background medium, which was equal to zero for dry snow.

The solid curves in Fig. 11-77 are plots of κ_e versus m_v at 4 GHz, 16 GHz, and 37 GHz. The data points are based on transmission measurements made for snow samples of varying wetness. Observations of the snow samples under a microscope indicate that a typical value for r is 0.5 mm; hence, this was the value used in calculating the curves in Fig. 11-77. Upon comparing the calculated curves with the measured data, we observe that the curves underpredict the measurements at 4 GHz, are comparable in level to the measurements at 16 GHz, and predict a level generally higher than the measured values at 37 GHz.

When snow melts, the absorption coefficient of the background medium, κ_{ab}, increases from zero for dry snow to a value larger than κ_s for $m_v \gtrsim 1\%$. Thus, the presence of a very small amount of liquid water in the snow mixture is sufficient to reduce the magnitude of the scattering albedo a to a very small value. This behavior is illustrated graphically in Fig. 11-78(a) for $r = 0.5$ mm. For $m_v \gtrsim 2\%$, the albedo is so small in magnitude that its dependence on r becomes inconsequential. Thus, when wet, snow becomes a nonscattering medium. The variation of the penetration depth δ_p as a function of m_v is shown in Fig. 11-78(b) for 4, 10, and 37 GHz.

11-15 Backscattering Behavior of Dry Snow

In the general case, the backscattering coefficient of snow-covered terrain may consist of (a) a direct contribution from the air-snow boundary, (b) a two-way attenuated contribution from the snow-ground boundary, (c) direct backscatter from the snow volume, and (d) indirect contributions resulting from the interaction between the snow volume and either or both boundaries of the snow layer. These various contributions are incorporated into the radiative-transfer formulations given in Sections 11-3 and 11-6.

Because the dielectric mismatch at the air-snow boundary is small for dry snow, the reflection coefficient is quite small, which, in turn, means that the snow-surface backscattering contribution may be neglected in comparison with the other contributions, except perhaps at normal incidence. This also means that multiple reflections involving the upper and lower boundaries of the snow layer may also be ignored. This contention is supported by the radar scatterometer observations reported in Fig. 11-79(a), which indicate that σ^0 is essentially insensitive to snow surface roughness when the snow layer is dry. The plots in Fig. 11-79(a)

[†] **Computer Code 11.4.**

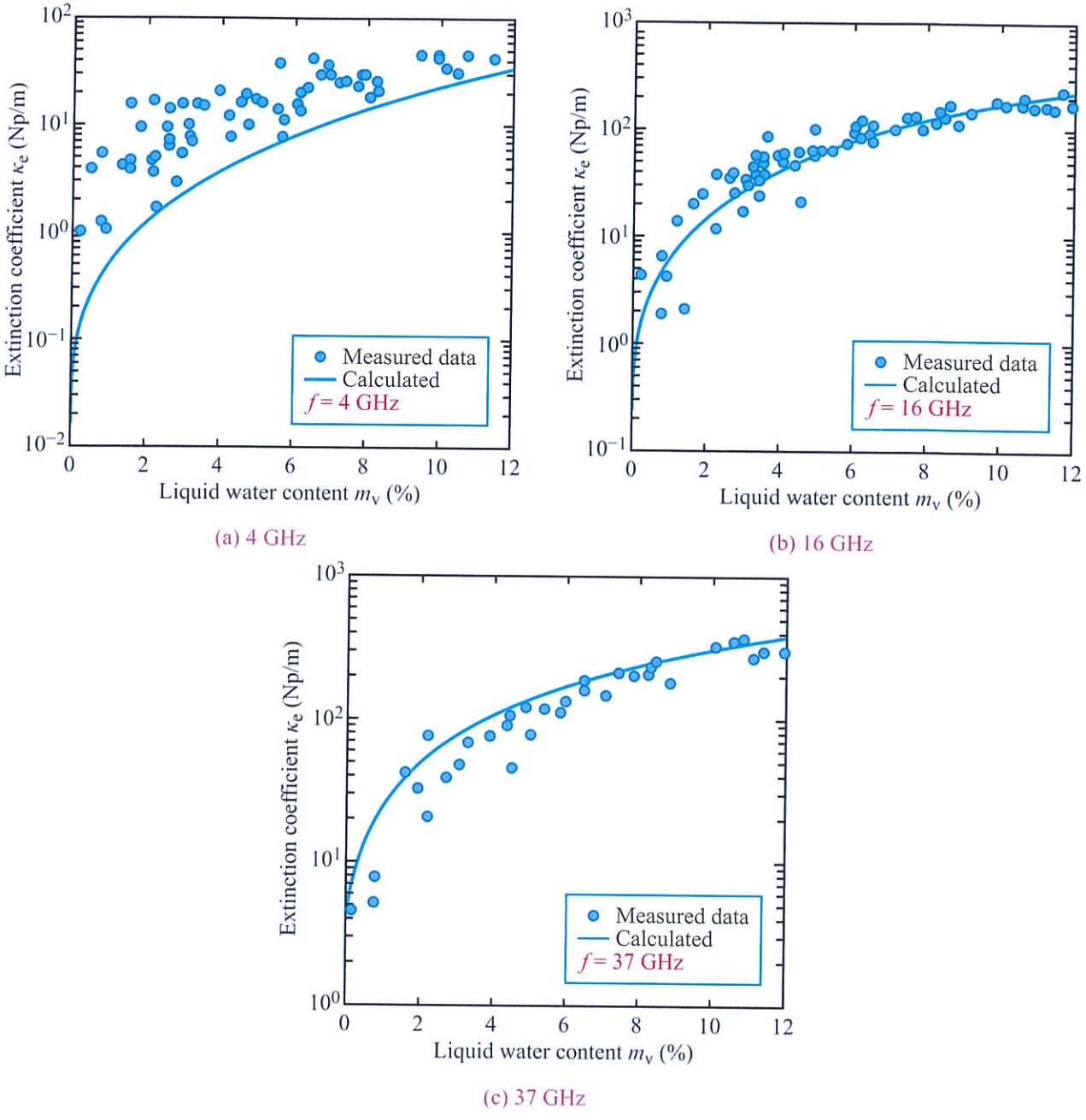

Figure 11-77: Comparison of the measured values of κ_e with the curves calculated for $\rho_s = 0.24$ g/cm^3, $r = 0.5$ mm, $A_a = A_b = 0.06$.

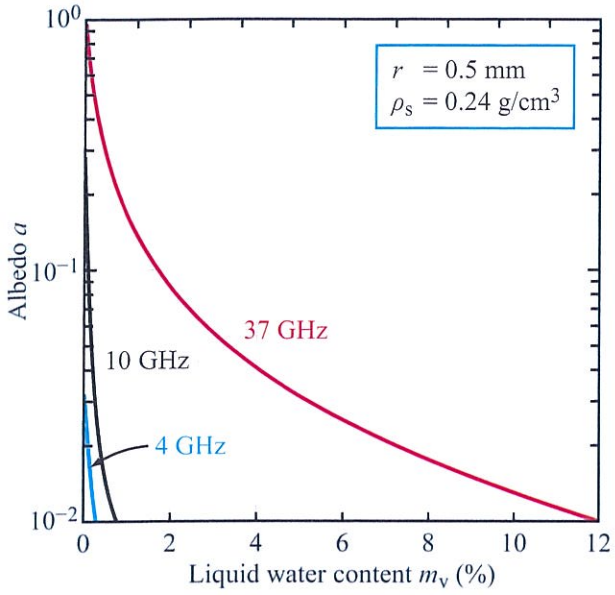

(a) Albedo

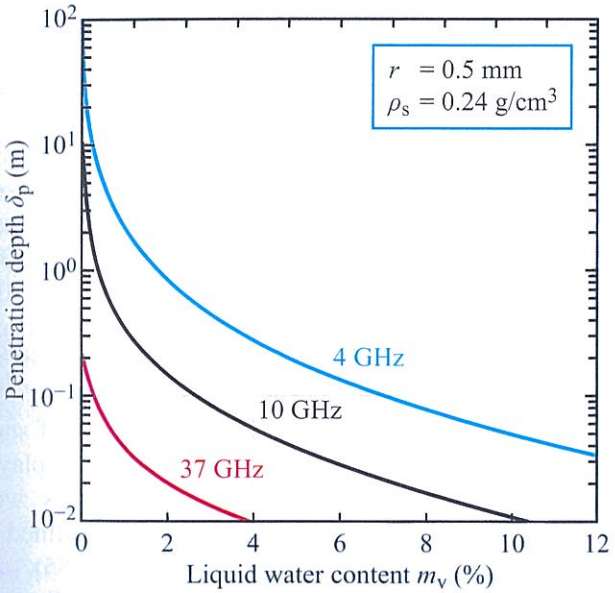

(b) Penetration depth

Figure 11-78: Mie-computed variation of snow (a) albedo and (b) penetration depth with liquid-water content.†

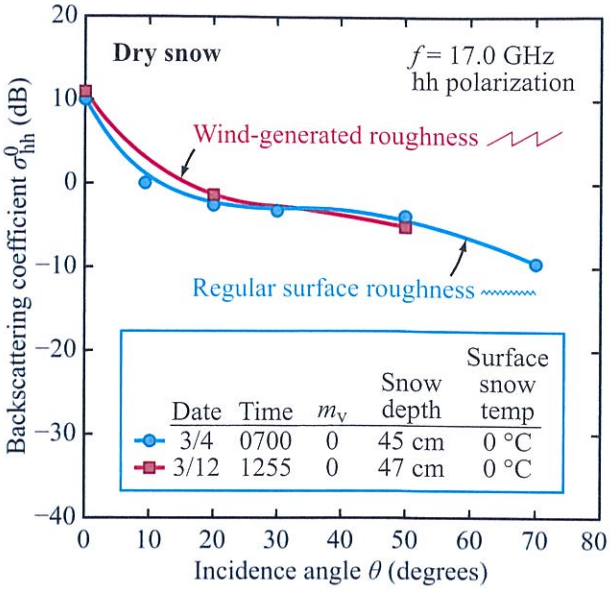

(a) Dry snow

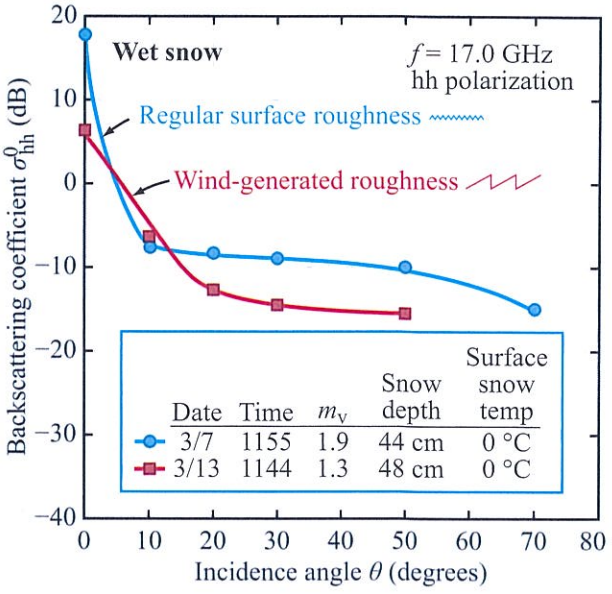

(b) Wet snow

Figure 11-79: Change in snow surface roughness has no effect on σ^0 when the snow is dry, but it does when the snow is wet [Stiles and Ulaby, 1980b].

compare σ^0 for dry snow with a "regular surface" characterized by high-frequency spatial variations with small amplitudes (on the order of 0.5 cm) with a "wind-generated surface" characterized by large smooth facets (about 30 cm long) connected by 2 cm high ridges, forming a sawtooth-like pattern. This latter surface condition was caused by strong southerly winds. The lack of any significant difference between the two curves in Fig. 11-72(a) indicates that σ^0 is insensitive to snow surface roughness when the snow is dry. This conclusion is based not only on the 17 GHz data shown in Fig. 11-79, but also on data measured at several other frequencies over the 1 to 35.6 GHz range.

In contrast to its lack of sensitivity to surface roughness for dry snow, σ^0 exhibits a significant response to surface roughness when the snow is wet. Figure 11-79(b) shows angular plots of σ^0 for essentially the same snowpack as before, except that now the top 5 cm of the snow layer contains some water in liquid form. Wet snow has a higher dielectric constant and lower albedo [Fig. 11-78(a)] than dry snow. Consequently, not only is the general angular pattern of $\sigma^0(\theta)$ different for wet snow, but so is the sensitivity of σ^0 to snow surface roughness.

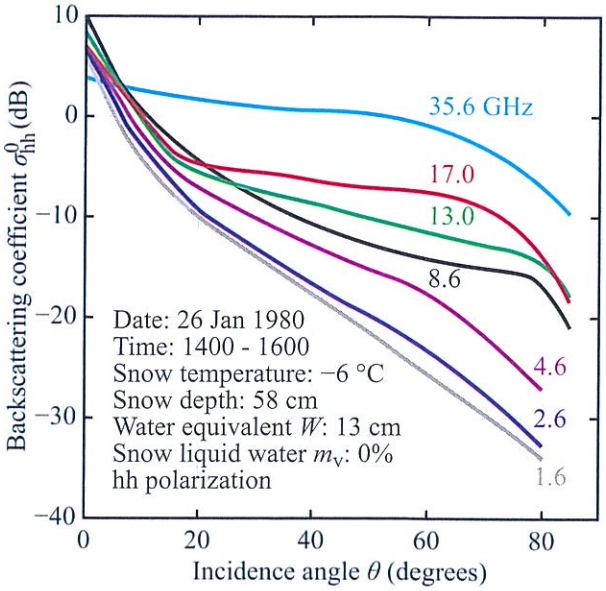

Figure 11-80: Angular patterns of measured backscattering coefficient of dry snow [Stiles et al., 1981].

11-15.1 Radiative Transfer Model

We open this subsection with Fig. 11-80, which displays angular plots of σ^0_{hh} for a 58 cm deep snowpack, measured at multiple frequencies between 1.6 GHz and 35.6 GHz. Based on the penetration depth and albedo plots shown in Figs. 11-74 and 11-76, we can surmise that at 1.6 GHz, the backscatter contribution of the snow layer is very small, so the measured plot of σ^0 is due primarily, if not entirely, to the underlying ground surface, as if the snow layer is totally absent. On the other end of the spectral range of the plots shown in Fig. 11-80, namely at 35.6 GHz, the 58 cm snow depth is equal to $\approx 5\delta_p$ (where δ_p is the penetration depth) and the albedo $a \gtrsim 0.9$. Hence, electromagnetically the snow layer is semi-infinite in depth; the backscatter is due to volume scattering in primarily the upper part of the snow layer.

The radiative transfer theory introduced in Section 11-6 is perfectly suitable for modeling the backscatter from a snow layer above a rough-surface snow-ground boundary. However, the iterative-solution method is capable of providing solutions of the radiative transfer equation (with reasonably accuracy) only if the albedo $a \lesssim 0.3$. Otherwise, a numerical solution is warranted. According to Fig. 11-76, for $r = 0.5$ mm, $a > 0.3$ if $f > 12$ GHz. Hence, a numerical solution is called for at frequencies above 12 GHz, and for snowpacks with larger ice particles the upper frequency limit of the iterative-solution method is lower still.

The theoretical behavior of σ^0 as a function of snow depth is illustrated by the families of plots displayed in Figs. 11-81 and 11-82. All computations were performed using the numerical technique outlined in the books by Fung (1994), Tsang et al. (1985), and Ulaby et al. (1986a). The plots in Fig. 11-81 illustrate the important role of the microwave frequency f. At 1.2 GHz, σ^0 is totally insensitive to snow depth d; the snow layer is essentially transparent to a 1.2 GHz EM wave, even for a layer as deep as 1.8 m. The sensitivity of σ^0 to d increases with increasing f. At 35 GHz, σ^0 exhibits a strong response to d between $d = 0$ and

	Ice loss factor	Soil surface parameters				Snow parameters	
f (GHz)	ε_i''	kl	kL	ks	m	Albedo a	κ_e (Np/m)
1.2	0.001	0.1	3	0.3	-	0.01	0.003
5.0	0.002	0.7	13	1.3	-	0.33	0.035
10.0	0.005	1.4	20	2.0	-	0.68	0.27
17.0	0.008	-	-	-	0.27	0.85	1.79
35.0	0.020	-	-	-	0.27	0.95	28.8

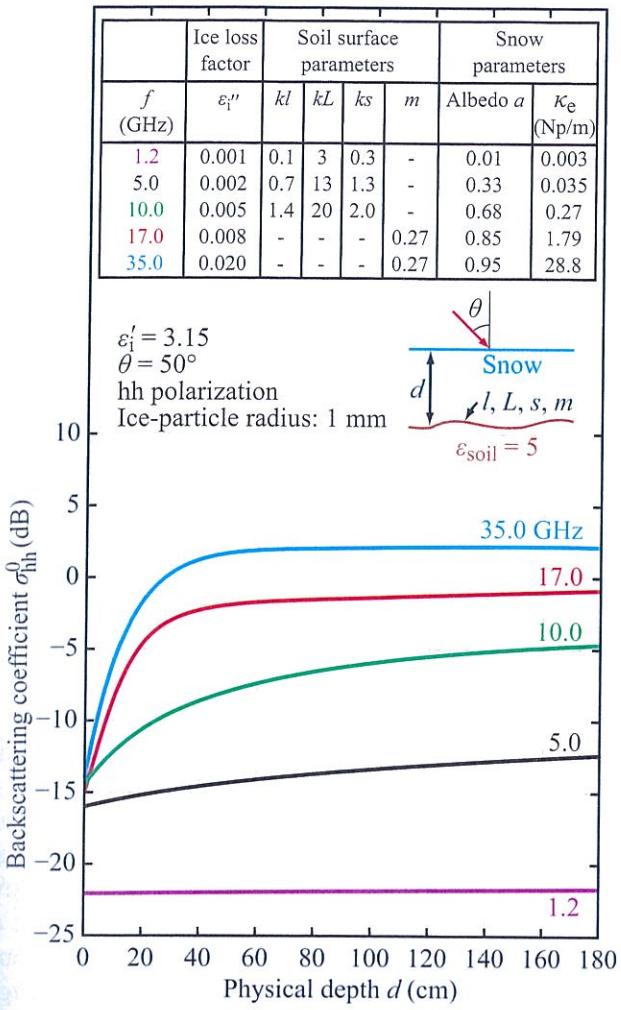

Figure 11-81: Calculated variation of σ^0_{hh} with d for a dry snow layer containing ice particles 1 mm in radius. Note the important role of frequency.

r (mm)	Albedo a	κ_e (Np/m)
0.25	0.03	0.09
0.50	0.21	0.11
0.75	0.47	0.16
1.00	0.68	0.27
1.50	0.88	0.70
2.00	0.94	1.55

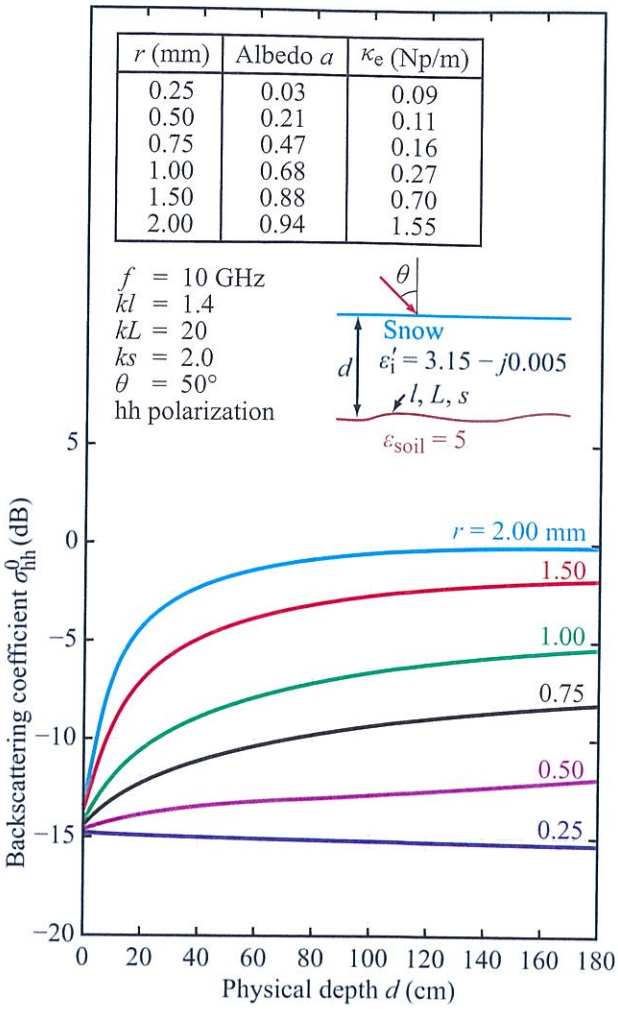

Figure 11-82: Calculated variation of σ^0_{hh} for a layer of dry snow over a dry soil surface as a function of the layer depth d, with the ice-crystal radius r as parameter. All calculations are for hh polarization at 10 GHz and $\theta = 50°$.

$d \approx 40$ cm, beyond which σ^0 approaches a saturation level.

The role of the ice-crystal radius is illustrated in Fig. 11-82. Here, $f = 10$ GHz and the variable parameter is r. Small crystals have small albedos and do not generate much scattering. Conversely, large crystals generate a great deal of scattering.

► The key parameter influencing volume scattering in snow is r/λ, where r is the crystal radius and λ is the wavelength. If $r/\lambda < 10^{-2}$, the snow layer appears electromagnetically invisible if its thickness $d \leq 2$ m. Conversely, the layer appears like a semi-infinite medium if $d \gtrsim 3000(r/\lambda)$. ◄

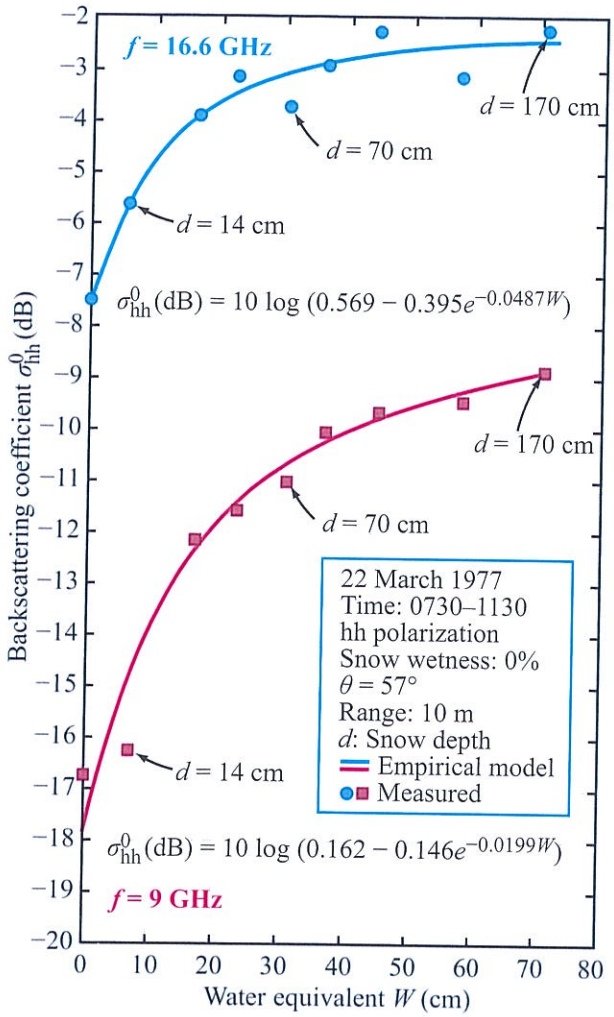

Figure 11-83: Response of backscattering coefficient σ^0 to snow water equivalent for dry snow at 9 and 16.6 GHz [Stiles and Ulaby, 1980a].

The general trends predicted by the theoretical plots of Fig. 11-81 are evident in the experimental measurements displayed in Fig. 11-83. The backscattering coefficient σ^0 was measured as a function of d by piling up dry snow in layers (Stiles and Ulaby, 1980a). The experiment was conducted at 9 and 16.6 GHz at an angle of incidence $\theta = 57°$. The measured data was empirically fitted with the following expressions:

$$\sigma^0 = c_1 - c_2 e^{-c_3 W} \qquad (m^2/m^2), \tag{11.115}$$

where c_1 to c_3 are constants and W is the ***snow water equivalent*** of the snow layer,

$$W = \int_0^d \rho_s \, dz. \tag{11.116a}$$

Here, ρ_s is the snow density in g/cm^3. For a layer with uniform density,

$$W = \rho_s d. \tag{11.116b}$$

The water equivalent is the height in cm of liquid water contained in a vertical column of the snow layer (after melting) with a horizontal cross section of 1 cm^2. The average density of the snow used in the experiment leading to Fig. 11-83 is $\rho_s = 0.42$ g/cm^3.

11-15.2 Role of Snow-Ground Interface

The dynamic range of σ^0 as a function of snow depth d extends between $\sigma^0_1 = \sigma^0_s$, representing the backscattering coefficient of the ground surface under snow-free conditions ($d \approx 0$), and the "saturation" level σ^0_2 representing the semi-infinite case. The lower bound, σ^0_1, is determined by the dielectric constant and roughness of the ground surface, and the upper bound, σ^0_2, is determined by the albedo of the snow layer. Figure 11-84 displays measurements made by a 13.9 GHz airborne system called POLSCAT. The measurements were made at three different sites. Whereas in all three cases the data appears to confirm the general pattern of σ^0 versus d, the starting levels of σ^0 at $d = 0$ among the three sites are different by as much as 8 dB. These differences are attributed to differences in ground surface conditions.

Figure 11-85 shows another example depicting the role of the snow-ground interface. Radiative-transfer calculations are compared with measurements made as a function of f from 1 to 18 GHz. The measurements shown are for $\theta = 20°$ and 50°. Excellent agreement is observed between theory and measurements when the ground surface is treated as a rough surface with $\sigma^0_s \neq 0$,

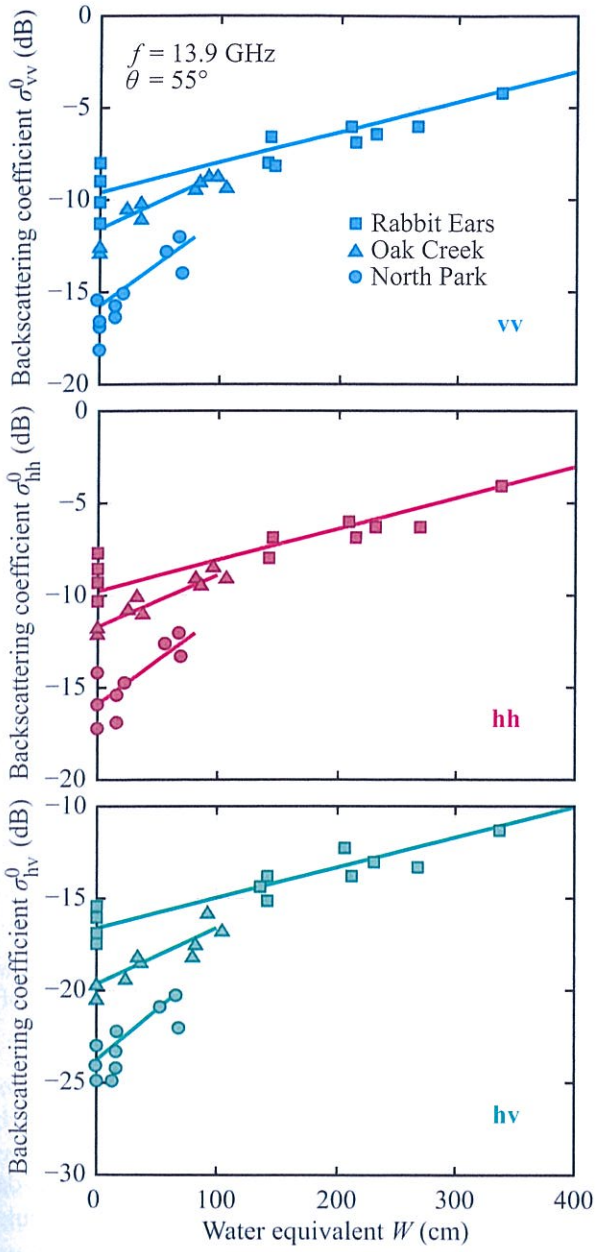

Figure 11-84: Comparison of 13.9 GHz POLSCAT radar data for three test sites [Yueh et al., 2009].

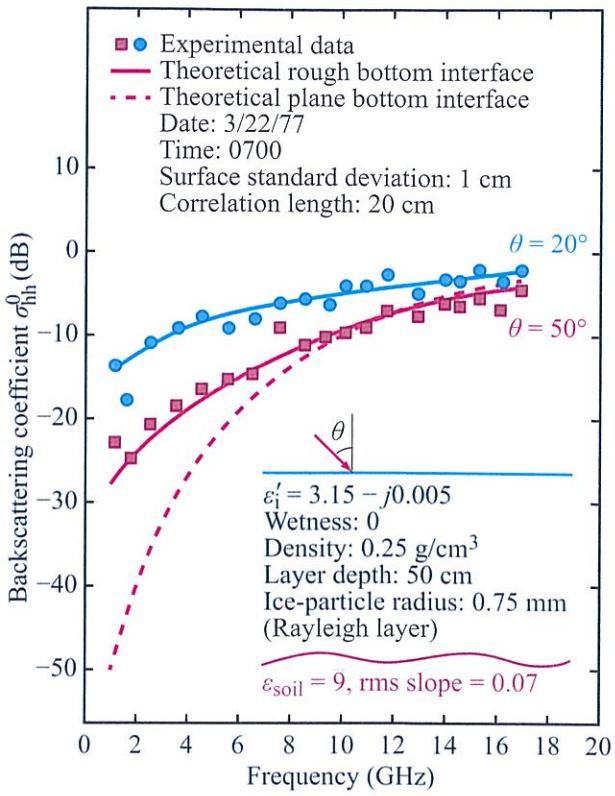

Figure 11-85: Comparison of theory and measurement for a layer of dry snow over the 1 to 18 GHz frequency band at 20° and 50° incidence angles.

but the agreement is quite poor at the low frequency end if we treat the ground surface as perfectly flat. For the purpose of computing the bistatic ground-snow and snow-ground contributions, the specular-surface assumption remains a reasonable approximation, but we should not altogether ignore the direct backscatter from the ground surface.

For deep snow with ice crystals of comparable size, the backscattering coefficient should be independent of the underlying ground surface. The plots in Fig. 11-86 were measured at very different sites, one in Colorado and the other in the Swiss Alps. The radar frequencies were approximately the same, the snow layer was sufficiently deep in both cases as to mask the underlying

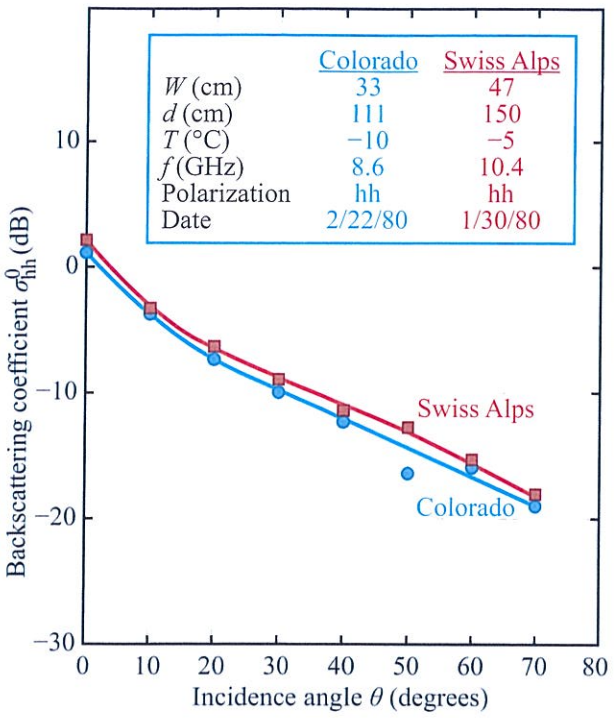

Figure 11-86: Comparison of deep-snow σ^0 measurements made at a site in the Swiss Alps (courtesy of C. Mätzler and E. Schanda, Univ. of Bern) with measurements made at a site in Colorado [from Ulaby et al., 1982d.].

(a) Photo of sled-mounted radar

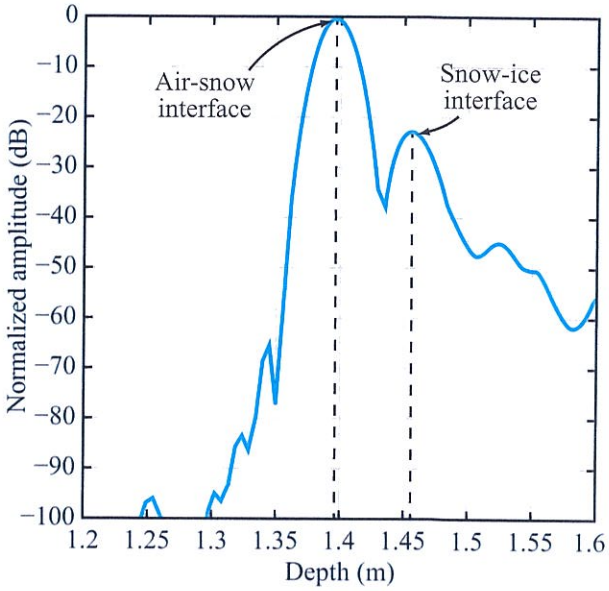

(b) Radar echo

Figure 11-87: (a) University of Kansas sled-mounted FMCW radar in Antarctica and (b) typical example of a radar echo [Kangaratnam et al., 2007].

surface, and so the measured angular responses of σ^0 of the two sites are almost identical.

11-15.3 Measuring Snow Thickness Over Sea Ice

Using an ultrawideband (2–8 GHz) FMCW radar mounted on a sled, a University of Kansas team evaluated the capability of the system for measuring the thickness of the snow layer over sea ice in Antarctica (Kanagaratnam et al., 2007). Figure 11-87(a) is a photograph of the FMCW radar system and Fig. 11-87(b) displays a typical example of the radar echo observed by the system. The first peak corresponds to the return from the air-snow boundary and the second peak corresponds to the snow-ice boundary. The snow layer thickness is computed from the time delay and the phase velocity u_p. The latter is calculated from $u_p = c/\sqrt{\varepsilon'_{snow}}$, and ε'_{snow} is determined using standard equations relating ε'_{snow} to the snow density ρ_s. The results of measurements conducted over a snow-thickness range from 4 cm to 85 cm are displayed in Fig. 11-88. By sweeping the signal frequency over a 6 GHz bandwidth (from 2 to 8 GHz), the theoretical

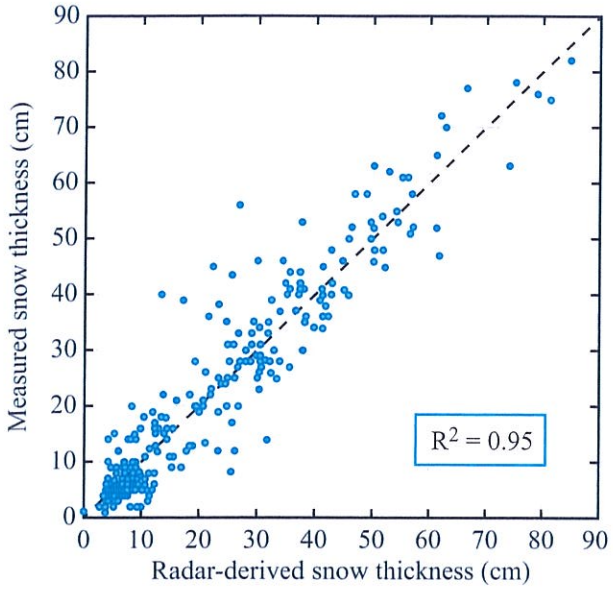

Figure 11-88: Comparison of radar-derived snow thickness with manually measured snow thickness [Kangaratnam et al., 2007].

range resolution of the FMCW system is

$$\Delta R = \frac{c}{2B} = \frac{3 \times 10^8}{2 \times 6 \times 10^9} = 0.025 \text{ m} = 2.5 \text{ cm} \qquad \text{(in air)},$$

and

$$\Delta R = \frac{2.5 \text{ cm}}{\sqrt{\varepsilon'_{\text{snow}}}} \qquad \text{(in snow)}.$$

The sled-mounted experiments were conducted in 2003 and reported in 2007. In 2008, a helicopter-mounted version of the FMCW radar [Fig. 11-89(a)] was used to demonstrate the snow-thickness measurement capability from an airborne platform. The experimental results, shown in Fig. 11-89(b), also exhibit good correlation between *in-situ* measurements of snow thickness and radar-derived values of snow thickness. The range of snow thickness that was encountered in Antarctica in 2008, however, was significantly narrower than that of 2003.

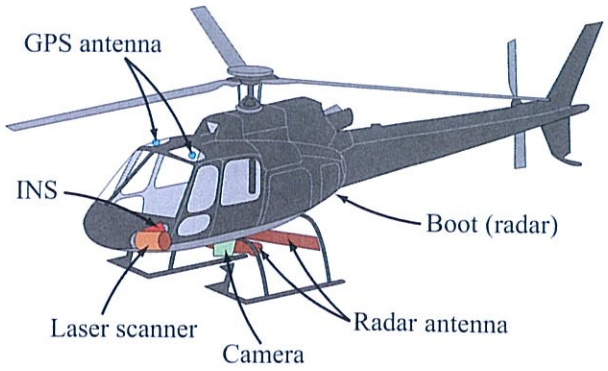

(a) Helicopter-mounted FMCW radar

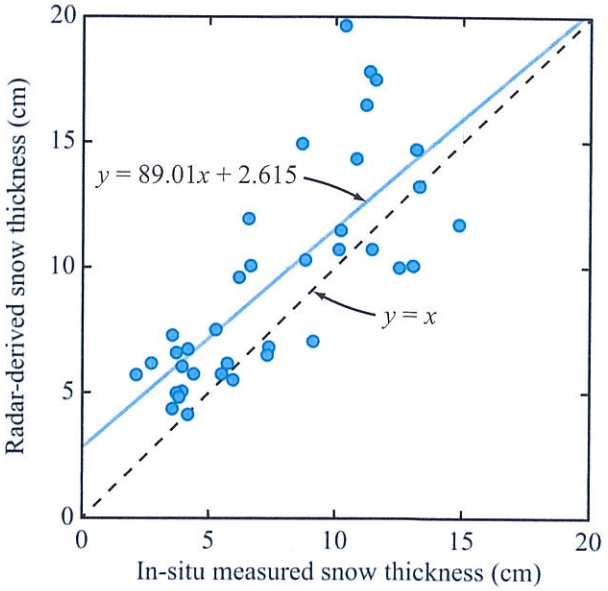

(b) Radar-derived vs in-situ measurements

Figure 11-89: (a) Helicopter-mounted FMCW radar and (b) results of measurement campaign [Galin et al., 2012].

11-16 Backscattering Behavior of Wet Snow

While the roughness of the snow surface exercises a negligible effect on the backscattering from snow when the snow layer is dry, it has a significant

impact on σ^0 when the snow is wet. This behavior, which is demonstrated by the curves introduced earlier in Fig. 11-79, is related to the average dielectric permittivity of snow. The relative permittivity for dry snow with a typical density of 0.25 g/cm^3 is about 1.5, compared with 2.6 at 6 GHz for snow containing 10 percent liquid water. The corresponding Fresnel reflectivities at normal incidence are 0.01 for dry snow and 0.06 for wet snow; i.e., the reflectivity of wet snow is larger than that of dry snow by a factor of 6. Consequently, when constructing a backscattering model for wet snow, the upper snow boundary is treated as a rough surface, in contrast to the dry-snow case in which it was regarded as a planar interface.

In addition to causing the permittivity of the snow layer to increase, the presence of liquid water in the snow volume causes a dramatic increase in the dielectric loss factor of the layer, ε''_{ws}, as detailed in Section 4-6.2. This, in turn, results in a large increase in the absorption coefficient, thereby reducing the relative importance of the ground contribution. Hence, to reduce the complexity of the single-scattering radiative transfer model of Section 11-6, the snow-ground interface usually is assumed to be a plane boundary.

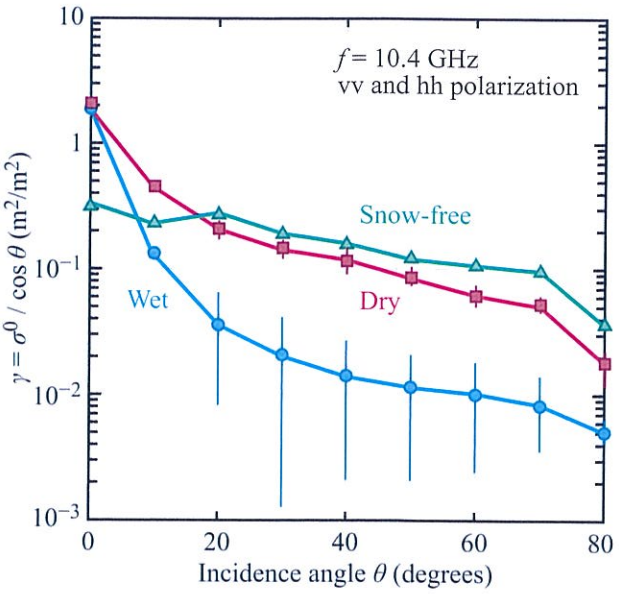

Figure 11-90: Mean values of vv- and hh-polarized backscattering coefficients averaged over all wet and dry snow, and over the snow-free situations, respectively. The standard deviations show the variability of the snow data [from Mätzler and Schanda, 1984].

11-16.1 Angular Dependence

To assess the potential of radar for mapping snow conditions, Mätzler and Schanda (1984) compared the measured angular response of $\gamma(\theta)$ for snow-free ground (Fig. 11-90) with responses for dry and wet snow, all measured at 10.4 GHz. The curves for dry and wet snow in Fig. 11-90 represent mean values measured over a wide range of snow conditions, and the vertical bars represent ± 1 standard deviation relative to the calculated means. The data in Fig. 11-90 indicate that for $\theta \geq 20°$ it should be easy to discriminate (using radar) between areas covered with dry snow and areas covered with wet snow, because of the large difference between σ^0 of dry snow and that of wet snow.

As an illustration of the role of the microwave frequency f with respect to both the shape of the angular response $\sigma^0(\theta)$ and sensitivity to snow wetness, we show in Fig. 11-91 data measured at 2.6 GHz and 35.6 GHz for a snow layer 27 cm deep. The 2.6 GHz curves show no sensitivity to the liquid-water content m_v. Furthermore, they exhibit an angular dynamic range of about 35 dB (between normal incidence and $\theta = 70°$). In contrast, at 35.6 GHz, $\sigma^0(\theta)$ of dry snow is about 8 dB higher than that of wet snow at all angles $\theta \geq 10°$. Also $\sigma^0(\theta)$ exhibits a much narrower angular dynamic range at 35.6 GHz, particularly when the snow is dry.

11-16.2 Frequency Dependence

The spectral curves in Fig. 11-92 illustrate the importance of the frequency f with regard to the sensitivity of σ^0 to snow wetness m_v. For a snowpack 48 cm deep, a change in wetness from zero to 1.26 percent results in a drop in level of only 1 dB at 1 GHz, but as f increases, the two curves diverge, and the difference between them increases to a maximum of 15 dB at 35.6 GHz.

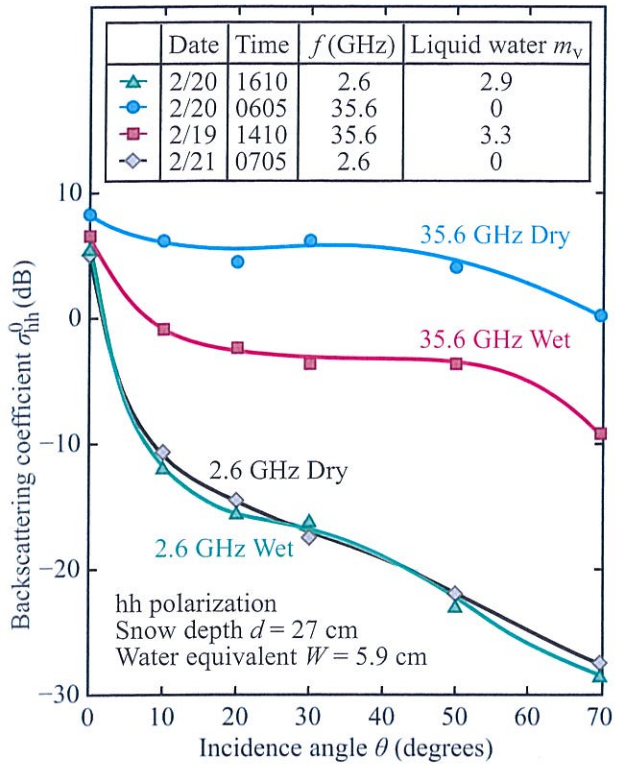

Figure 11-91: Angular dependence of σ^0 for wet and dry snow at 2.6 GHz and 35.6 GHz [from Stiles and Ulaby, 1980a].

11-16.3 Wetness Dependence

According to the data shown in Fig. 11-93, σ^0 exhibits an approximately linear response to m_v up to about 5 percent by volume. The measurements were made at 17 GHz for the depth and water equivalent values indicated alongside the curves. Similar measurements made at 8 GHz indicate that the response is linear over an even wider range of m_v (Ulaby and Stiles, 1981). In general, in the 1 to 35 GHz region, the magnitude of the sensitivity of σ^0 to m_v (i.e., $|d\sigma^0/dm_v|$ over the quasi-linear range of σ^0 versus m_v) increases with increasing frequency; however, concurrently, the detectable range of m_v (for which the σ^0 response is quasi-linear) decreases with increasing frequency. Thus, the choice of frequency should be dictated by whether

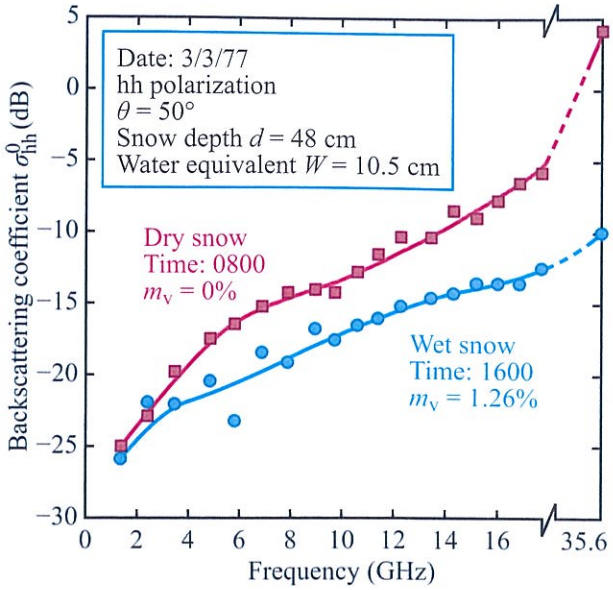

Figure 11-92: Spectral response of σ^0 for wet and dry snow [from Ulaby and Stiles, 1981].

it is more important to detect the presence of water in liquid form in the snowpack or to actually measure its percentage over as wide a range as possible.

11-16.4 Diurnal Variations

A convenient way to evaluate the response of σ^0 to snow wetness variations is to monitor σ^0 over a 24-hour diurnal cycle under clear-sky conditions. Figure 11-94 shows the results of such an experiment performed at $\theta = 50°$. During the daylight hours, the wetness m_v (of the top 5 cm layer) increased from zero at 0800 hours to a maximum of 1.26 percent by volume at 1500 hours and then decreased back to zero in the late afternoon. The observed σ^0 diurnal patterns are essentially mirror images of the m_v pattern, with some possible time-shifting between the σ^0 and m_v patterns. The magnitude of the dip in σ^0 increases from about 2 dB at 2.6 GHz to 15 dB at 35.6 GHz.

Under overcast conditions at below freezing temperatures, diurnal observations show no variation in σ^0. However, solar illumination under clear-sky conditions

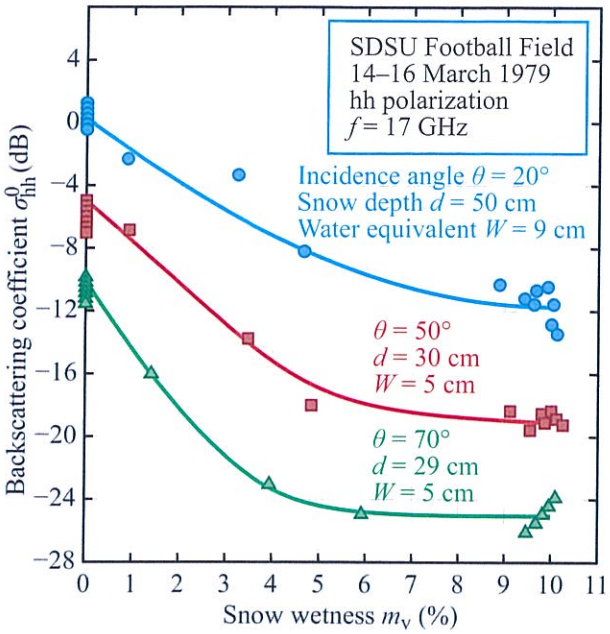

Figure 11-93: Measured response of σ^0 to snow liquid-water content at 17 GHz [from Ulaby and Stiles, 1981].

may cause partial melting of the snow's surface layer, even though the air temperature may be below freezing.

11-16.5 Seasonal Variations

Using a truck-mounted radar system, backscattering observations were made at a snow test site in Colorado for a period of six weeks (Ulaby and Stiles, 1981). The results for $f = 8.6$ GHz and $\theta = 50°$ are presented in Fig. 11-95 in the form of temporal plots of σ^0, the snow water equivalent W, and the liquid-water content m_v. In the figure, the boundaries of the temporal plot of σ^0 appear to form an envelope extending between two lines designated σ^0_{max} and σ^0_{min}. When the top layer of the snow is wet, it masks the contributions of the lower layers, and hence σ^0_{min} is essentially independent of the water equivalent W (so long as W is larger than some minimum value that equals 2 to 3 penetration depths in wet snow) and varies with m_v in a fashion similar to that indicated in Fig. 11-93. For dry snow, σ^0 increases with

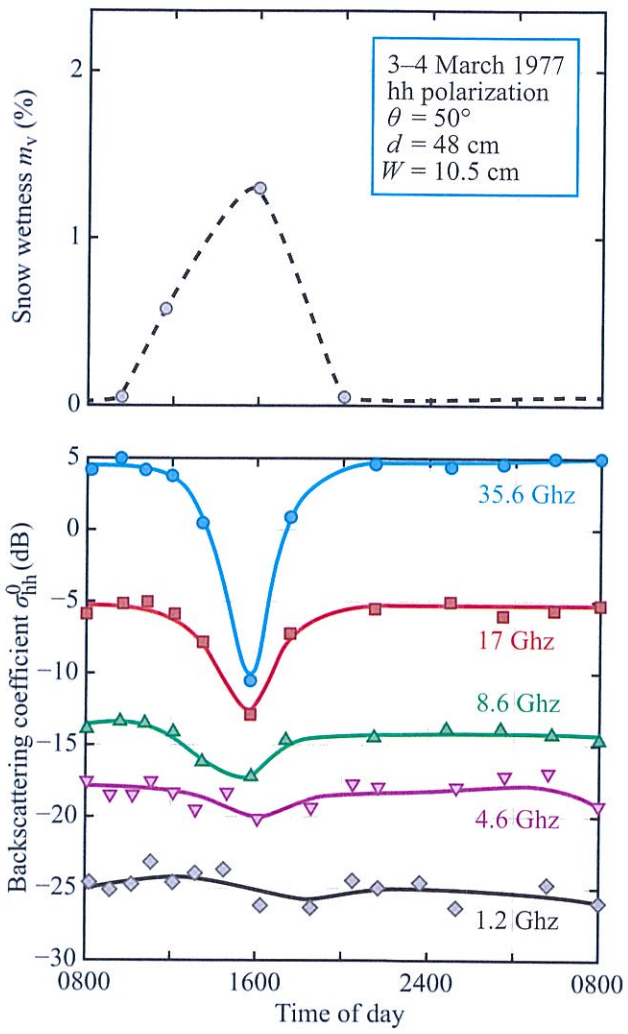

Figure 11-94: Diurnal patterns of liquid-water content m_v and backscattering coefficient σ^0 at several microwave frequencies [from Stiles and Ulaby, 1980a].

increasing W. This dependence is responsible for the observed positive slope of σ^0_{max}.

Although σ^0 varies with both m_v and W, it is possible to separate the causes of the changes in σ^0 by making observations both during the day and at night. At night, the snowpack is likely to be cold and dry; therefore, multidate nighttime observations may be used to update the status of W. The magnitude of the decrease in the

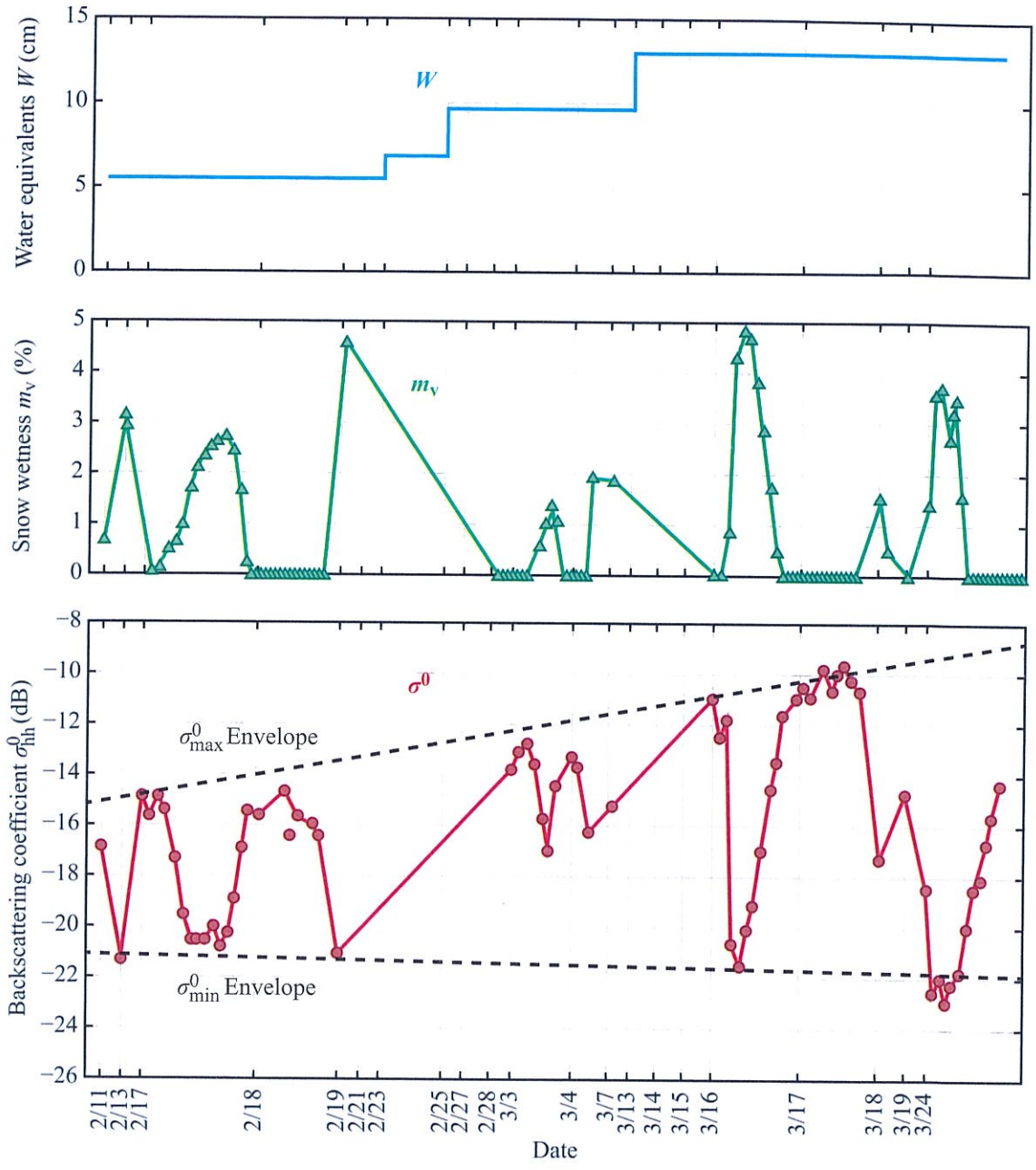

Figure 11-95: Temporal variation of σ^0 for Colorado snow test site [from Ulaby and Stiles, 1981].

level of σ^0 observed during daytime hours following a nighttime observation should then be indicative of the degree of wetness of the snowpack.

It is important to note that although the total increase in σ^0_{max} over the six-week period was only about 5 dB (in response to an increase in W of about 7 cm and a corresponding increase in depth of about 25 cm), such a change is quite significant when based on multidate observations of the same snowpack scene. During nighttime observations, the snow-layer and underlying ground parameters (other than W) influencing σ^0 are likely to exhibit much smaller temporal variations for a given ground cell than spatial variations on a given date. Thus, the use of change-detection techniques, in which a radar image of a given scene is "subtracted" from an image made earlier, may prove quite useful in estimating the water equivalent W of snowpacks over large areas.

11-16.6 Millimeter-Wave Observations

Our discussion thus far has dealt with the backscattering behavior of snow in the 1 to 35 GHz band. Far fewer studies have been reported involving measurements at higher frequencies. Examples illustrating the behavior of σ^0 for wet and dry snow at 35, 98, and 140 GHz are given in Fig. 11-96. As f increases from 35 GHz to 140 GHz, we observe the following patterns:

(a) The level of σ^0_{hv} approaches that of σ^0_{vv}, indicating the increased generation of cross-polarized energy as a result of the increase in the size of the ice crystals (in the snow volume) relative to λ.

(b) The sensitivity of σ^0 to wetness decreases. At 140 GHz, σ^0 is almost completely insensitive to m_v. This behavior is attributed to the albedo of the snow medium. At 35 GHz, the albedo of dry snow is on the order of 0.8, and when the snow is wet ($m_v \geq 1\%$) the albedo decreases to 0.3 or less (see Fig. 11-78(a)]. At 140 GHz, on the other hand, the albedo of dry snow is very close to 1.0 (because of the much larger sizes of the ice crystals relative to λ), and the presence of water in liquid form has little influence on the albedo because the permittivity of liquid water at 140 GHz is around 5,

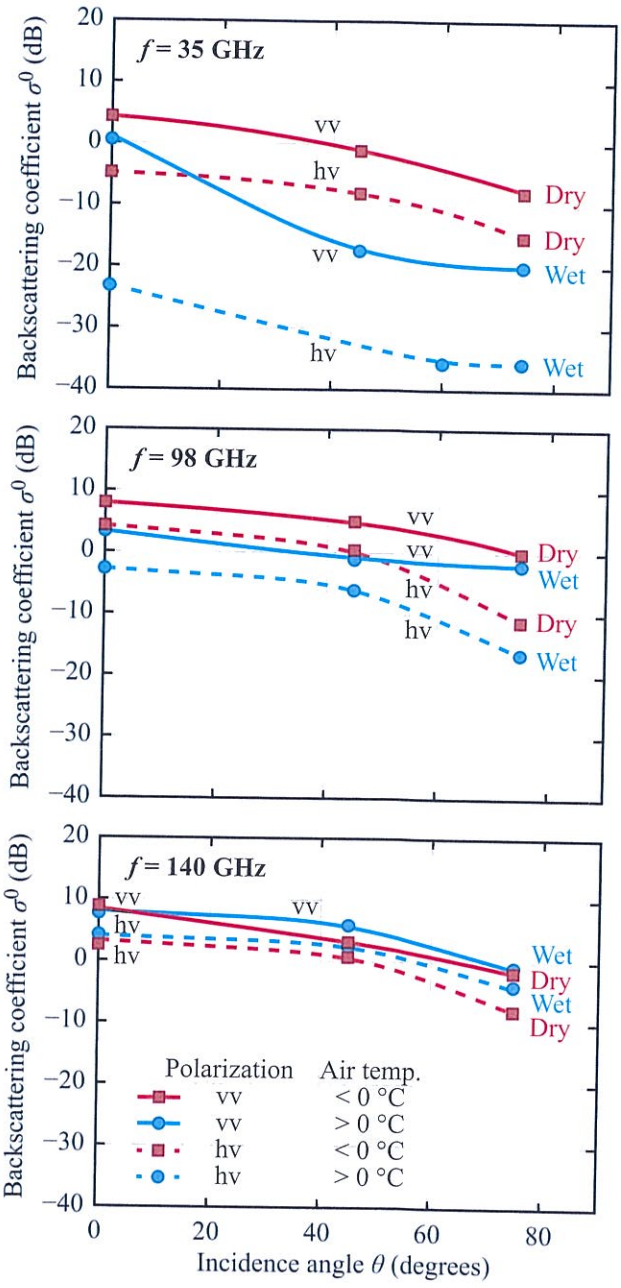

Figure 11-96: Measured angular variation of σ^0 for dry and wet snow at (a) 35 GHz, (b) 98 GHz, and 140 GHz [from Hayes et al., 1979].

which is not drastically different from that of the ice crystals, $\varepsilon_i' = 3.15$.

Applying a numerical solution to the radiative transfer equation, Kuga et al. (1991) evaluated the theoretical response of σ^0 to snow wetness at 35, 95, and 140 GHz. They modeled a 45 cm deep snowpack with an ice volume fraction of 0.4 (or an equivalent snow density $\rho_s = 0.37$ g/cm^3), containing ice particles characterized by a normal size distribution with a mean diameter of 1 mm and a standard deviation of 0.2 mm. The snow surface was assumed to have a rms slope $m = 0.5$. Their results for hh and hv polarizations are displayed in Fig. 11-97. We observe that:

(a) The cross-pol scattering coefficient σ^0_{hv} is more sensitive to snow wetness than the co-polarized component σ^0_{hh}.

(b) The sensitivity to snow wetness decreases with frequency; among the three millimeter-wave frequencies, the dynamic range of σ^0 due to m_v changing from 0 to 6% is highest at 35 GHz and lowest at 140 GHz.

The theoretical predictions of the radiative transfer model are confirmed by the experimental results and associated model calculations shown in Figs. 11-98 and 11-99 (Ulaby et al., 1991). The first figure displays plots of the recorded air temperature, snow surface temperature, and average snow wetness of the top 5 cm snow layer. Figure 11-99 contains plots of the measured diurnal variation of σ^0_{hh} at 35, 95, and 140 GHz, as well as model-calculated values. The calculated values are based on a hybrid first-order-numerical model applied to a snowpack with a snow-wetness depth profile that incorporates the thawing and refreezing processes that a snowpack undergoes over a diurnal cycle. Very good agreement is observed between the model-calculated and radar-measured diurnal patterns at all three millimeter-wave frequencies.

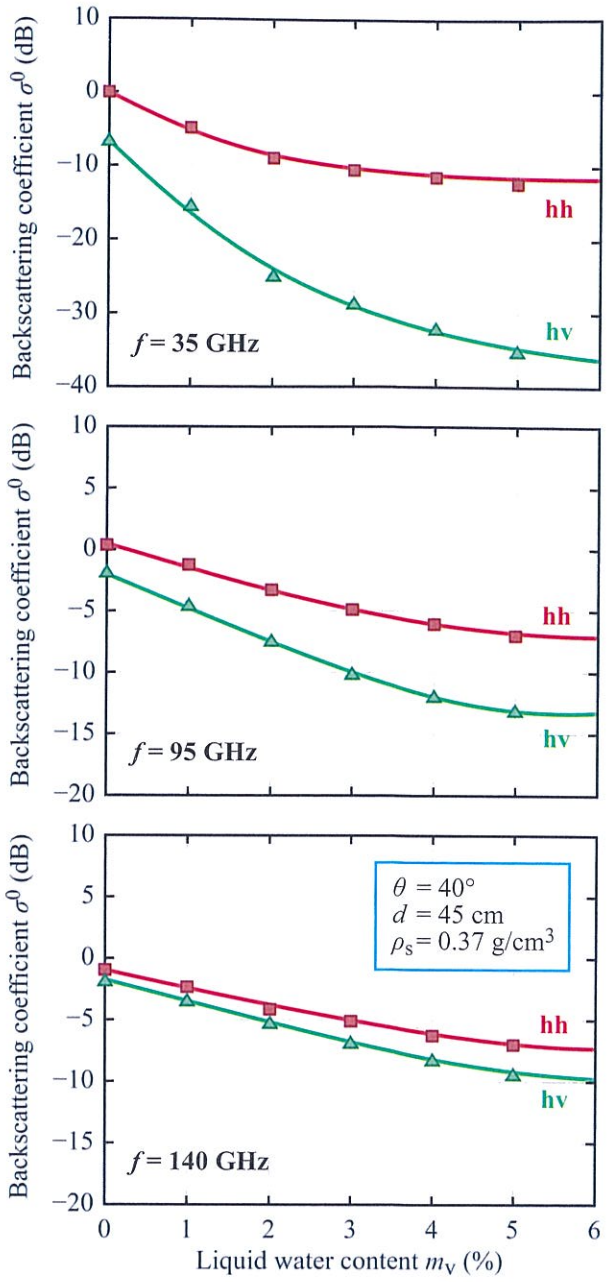

Figure 11-97: Backscattering coefficient σ^0 versus m_v at 35, 95, and 140 GHz [Kuga et al., 1991].

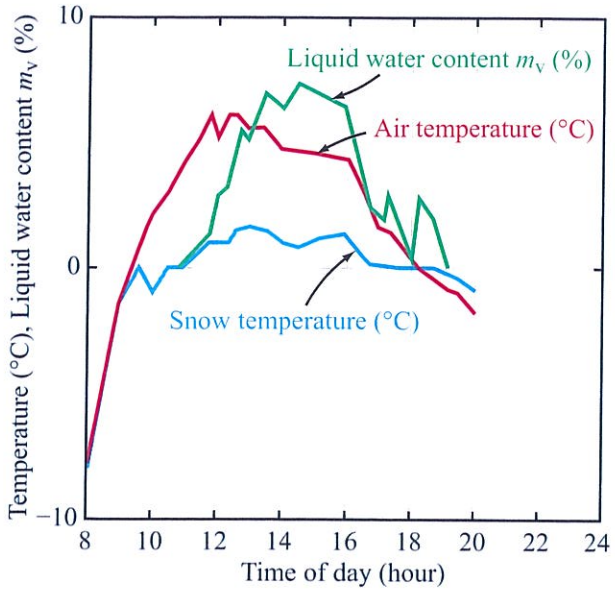

Figure 11-98: Temporal variations of air and snow temperatures and snow liquid-water content [Ulaby et al., 1991].

PROBLEMS

Canopy for Problems 11.1 to 11.3

A vegetation canopy is characterized by the following parameters:

albedo $a = 0.03f$, with f in GHz ($1 \leq f \leq 20$ GHz),

extinction coefficient $\kappa_e = 0.3f$ (Np/m), with f in GHz ($1 \leq f \leq 20$ GHz).

The underlying soil is loam and has a random surface with an rms height of 1 cm. Assume PRISM-1 is applicable.

11.1 Compute the backscattering coefficients for hh and vv polarizations at $\theta_i = 30°$ and $f = 3$ GHz as a function of the canopy thickness d (0 to 2 m) for:

(a) a dry soil surface with $m_v = 0.05$ g/cm^3.

(b) a wet soil surface with $m_v = 0.3$ g/cm^3.

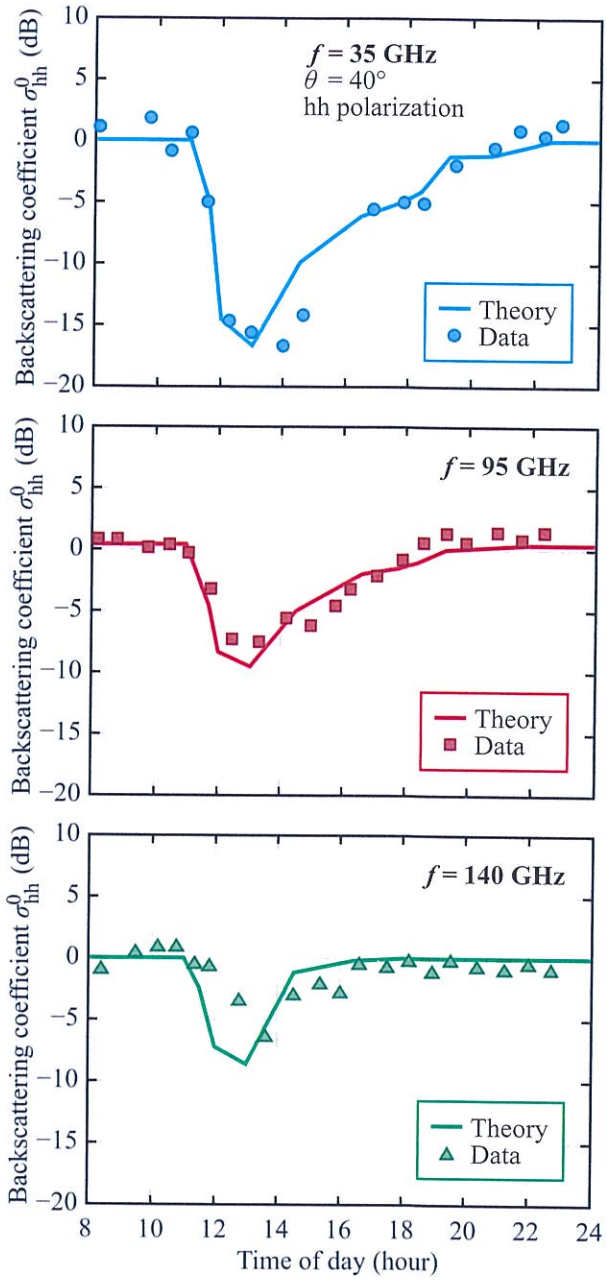

Figure 11-99: Comparison of the diurnal variation of the measured backscattering coefficient (relative to dry snow) with that using a hybrid first-order–numerical radiative transfer model [Ulaby et al., 1991].

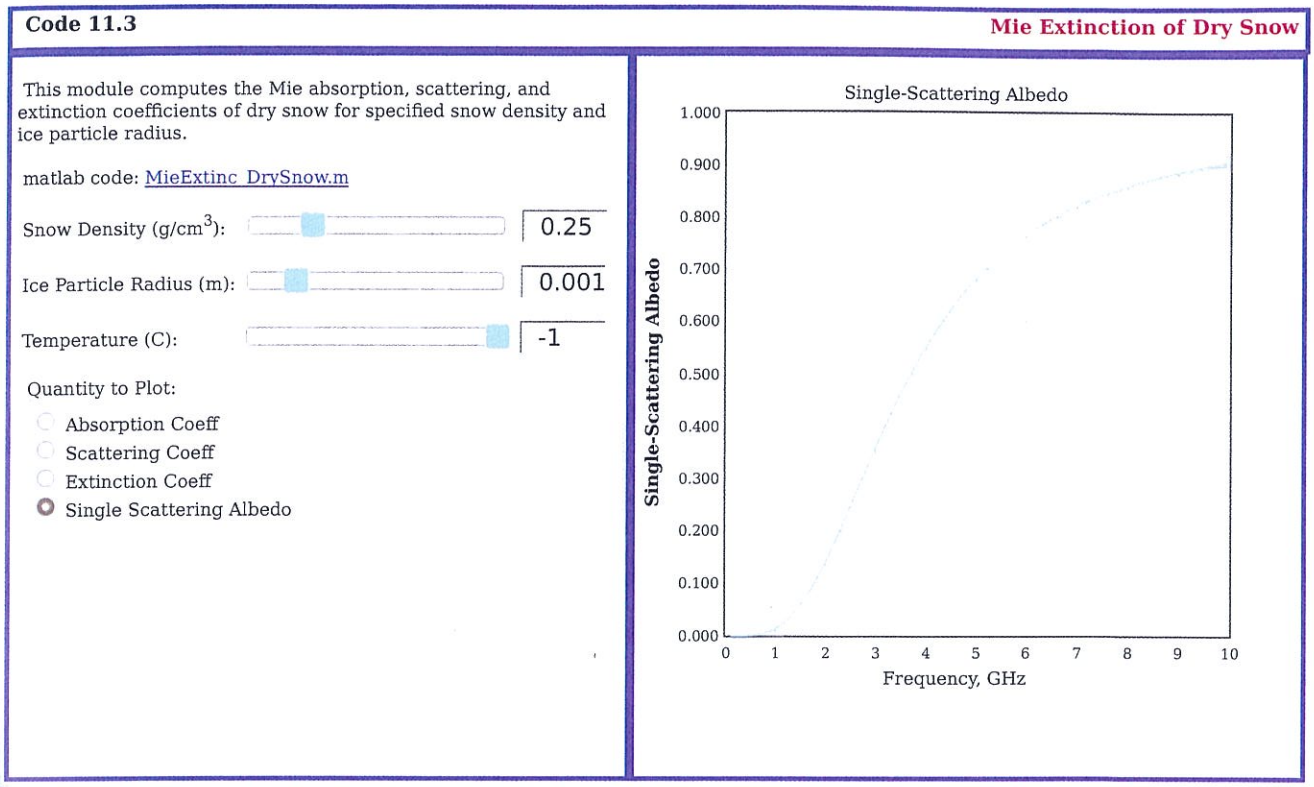

An example of one of the interactive modules available at the book website: mrs.eecs.umich.edu.

11.2 Compute the hh-polarized backscattering coefficient at $\theta_i = 30°$ as a function of volumetric soil moisture content (0 to 0.3 g/cm^3) for a 1 m tall canopy at:

(a) 1 GHz.

(b) 3 GHz.

(c) 10 GHz.

In each case, determine the radar sensitivity to soil moisture by computing the slope at $m_v = 0.2$ g/cm^3.

11.3 Compute the hh-polarized backscattering coefficient at $\theta_i = 30°$ as a function of frequency (1 to 10 GHz) for a 1 m tall canopy above a soil surface with:

(a) $m_v = 0.05$ g/cm^3.

(b) $m_v = 0.30$ g/cm^3.

11.4 A layer of dry snow of depth d overlays a soil surface. In the absence of snow, the hh-polarized backscattering coefficient of the soil surface at $\theta = 30°$ is given by

$$\sigma^0_{soil} = 0.01 + 0.001 f,$$

where f is in GHz ($1 \leq f \leq 30$ GHz).

The snow density is 0.5 g/cm^3 and at 10 GHz, the snow albedo is 0.2 and the extinction coefficient is 0.15 Np/m. Assuming that the snow layer has a flat top surface and that it can be treated as a Rayleigh layer, compute and plot the hh-polarized backscattering coefficient at 30° as a function of d from 0 to 2 m.

11.5 Repeat Problem 11.4 for wet snow, keeping all parameters the same except for changing the albedo to 0.01 and the extinction coefficient to 1.2 Np/m.